





This is to certify that the

dissertation entitled

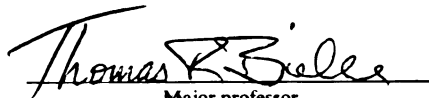
Mechanical Twin Nucleation, Propagation And
Mechanical Twinning During Creep Deformation In TiAl

presented by

Zhe Jin

has been accepted towards fulfillment
of the requirements for

Ph.D. degree in Materials Science


Major professor

Date 3-28-94

LIBRARY
Michigan State University

PLACE IN RETURN BOX to remove this checkout from your record.
TO AVOID FINES return on or before date due.

DATE DUE	DATE DUE	DATE DUE
SEP 25 1997	SEP 25 1997	
JUN 1 1 1998	SEP 25 2004	
JUN 1 1 1998		
SEP 23 1997		
FEB 2 1998		
JUN 09 1998		
JUN 2 1998		
MAR 03 1998		

MSU is An Affirmative Action/Equal Opportunity Institution

c:\circ\dlibdue.pm3-p.1

**MECHANICAL TWIN NUCLEATION, PROPAGATION
AND MECHANICAL TWINNING DURING
CREEP DEFORMATION IN TiAl**

**By
Zhe Jin**

A DISSERTATION

**Submitted to
Michigan State University
in partial fulfillment of the requirements
for the degree of**

DOCTOR OF PHILOSOPHY

Department of Materials Science and Mechanics

1994

ABSTRACT

MECHANICAL TWIN NUCLEATION, PROPAGATION

AND MECHANICAL TWINNING DURING CREEP DEFORMATION IN TiAl

By

Zhe Jin

Gamma titanium aluminide (TiAl) is a promising candidate material for high temperature and high performance applications because of its high strength, low density, good oxidation resistance, and excellent high temperature mechanical properties. In recent years, much work has been done in order to understand its deformation mechanisms at room temperature and high temperatures. The experimental results have shown that mechanical twinning is an important deformation mechanism in TiAl both at room temperature and at high temperature. Even under creep deformation conditions the mechanical twinning still has a significant contribution to the creep deformation. Therefore, in order to understand the mechanical twinning behavior during creep deformation of TiAl, mechanical twin nucleation and propagation mechanisms and the mechanical twinning contribution to the creep deformation in TiAl were studied.

Mechanical twin nucleation and propagation were *in situ* observed in creep deformed specimens using electron beam illumination in TEM. The mechanical twins nucleated either at grain boundaries or at twin interfaces due to the local stress concentration. The nucleus was either a superlattice intrinsic stacking fault that was a result of emission of one twinning dislocation from the grain boundary or the twin interface, or an extrinsic superlattice stacking fault resulting from the emission of two

twinning dislocations. The twinning dislocation was identified to be Shockley partial $\frac{1}{6}\langle 11\bar{2} \rangle$ and the twinning plane was identified as (111). The twinning propagation mechanism was a homogeneous glide of twinning dislocations on every adjacent twinning plane.

The stress state necessary for twin propagation is that the principal tensile stress axis must be orientated in the vicinity of $[55\bar{1}]$ crystal orientation. The stresses in the twin layers are classified into three categories: forward stress, back stress and external stress, (the definition of each stress is referred to section 4.4). A stress analysis on a thin twin layer shows that both the forward stress and back stress are very large at the twin tip, but they decrease as the distance from the twin tip increases. At very large distances from the twin tip, both stresses tend to be constant. The external stress is constant along the twin layer investigated.

Both true-twinning and pseudo-twinning configurations are observed in creep deformed specimens. The analyses of mechanical twin (true-twin and pseudo-twin) formation during creep of TiAl show that mechanical twinning in TiAl obeys the maximum resolved shear stress criterion.

Stress concentrations at grain triple points are found to be accommodated by formation of fine mechanical twins. These fine mechanical twins result in zigzagged grain boundaries at their intersections with the grain boundaries and hence inhibit the grain boundary sliding. The formation of fine mechanical twins are probably controlled more by the local stress concentration than by an externally applied stress.

Copyright by

ZHE JIN

1994

To My Parents

Zhong-Zhi Jin and Yu-Jin Cui

ACKNOWLEDGEMENTS

I sincerely appreciate the help of my major professor, Dr. Thomas R. Bieler. He has been a good friend and has provided me with an effective and encouraging environment to finish this research.

I am also very grateful to my graduate committee, Prof. Martin A. Crimp, Prof. David Grummon, Department of Materials Science and Mechanics, and Prof. Carl L. Foiles of Physics and Astronomy Department. They have provided many effective suggestions in selecting the research topic and the facilities necessary to pursue this research.

Particularly, I would like to express my sincere appreciation to Howmet Corporation, Whitehall, Michigan for the financial and material support to make this research possible. I would like to express my thanks to Dr. B. London, Dr. T. Thom, Dr. N.E. Paton, Dr. D.A. Weeler for their contributions in pursuing this research.

I would also like to express my gratitude to my wife, Jiyan An, for her patient support and encouragement during my entire graduate study.

TABLE OF CONTENTS

LIST OF TABLES	xiv
LIST OF FIGURES	xvi
CHAPTER ONE. INTRODUCTION	1
CHAPTER TWO. THEORY	7
2.1. Titanium Aluminide TiAl	7
2.1.1. Crystal Structure	7
2.1.2. Stacking Faults	9
(a) APB (Antiphase Boundary)	11
(b) SISF (Superlattice Intrinsic Stacking Fault)	13
(c) CSF (Complex Stacking Fault)	13
(d) SESF (Superlattice Extrinsic Stacking Fault)	14
2.1.3. Dislocations and Dislocation Core Structures	14
(a) $1/2 \langle 110 \rangle$ Type	15
(b) $\langle 101 \rangle$ Type	16

(c) $1/2 <112]$ Type	16
(d) $<100>$ Type	17
2.1.4. Dislocation Blocking Mechanisms	17
(a) Roof-Type Blocking	18
(b) Kear-Wilsdorf Blocking	20
(c) Deep Peierls Valley Blocking	21
(d) SSF-Tube Type Blocking	22
(e) Dislocation Interaction Blocking	26
2.1.5. Lamellar Structure and Its Formation	28
(a) Type-I Lamellar Structure	28
(b) Type-II Lamellar Structure	29
2.1.6. Phase Transformation Mechanisms	31
2.2. Mechanical Twinning Theory	33
2.2.1. Definition	33
2.2.2. Seven Twinning Classes	35
2.2.3. Classic Twinning Modes	37
2.2.4. Crystallography of Mechanical Twinning	38
2.2.5. Atomic Movement in Twinning Shear	45
2.2.6. Strain in Twinning	48
2.2.7. Prediction of Twinning Elements (Twinning Criterion)	52
2.2.8. Twinning in Superlattice	53

2.2.9. Mechanical Twin Nucleation and Propagation	61
(a) Dislocation Pole Mechanism in bcc Metals	62
(b) Dislocation Pole Mechanism in hcp Metals	63
(c) Dislocation Pole Mechanism in fcc Metals	66
2.2.10. Twin Shape	68
(a) A Model Concerning Energy Associated With Twinning	68
(b) A Model Based on Twinning Dislocation Interaction Forces	72
2.3. Creep Theory	75
2.3.1. Microstructural Correspondences to Creep	76
2.3.2. Mechanical Model	77
2.3.3. Microstructural Model	80
 CHAPTER THREE. MECHANICAL TWIN NUCLEATION AND PROPAGATION IN TiAl.....	
3.1. Materials and Experimental Procedure	83
3.2. Results and Analyses	85

3.2.1. <i>In Situ</i> Observations of Mechanical Twin	
Nucleation and Propagation	85
(a) Twin Nucleation at Grain Boundaries	85
(b) Twin Nucleation at Twin Interfaces	100
(c) Twin Layer Morphology Near The Twin Tip	107
3.2.2. Post-Mortem Observation of Mechanical Twinning	
During Creep Deformation	107
3.3. Discussion	113
3.3.1. Mechanical Twin Nucleation in TiAl	113
3.3.2. Mechanical Twinning Mechanisms in TiAl	116
3.3.3. On The DO ₁₉ phase in Fine Mechanical Twins	121
3.3.4. Twin Morphology	122
3.4. Summary	123

CHAPTER FOUR. FORCE AND STRESS ANALYSES

IN A THIN TWIN LAYER.....	126
4.1. Theory	127
4.1.1. Forces on Each Twinning Dislocation	127
4.1.2. Dislocation Interaction Forces	131

4.1.3. Internal Friction Force	134
4.1.4. The Force Due to The Stacking Faults	136
4.1.5. Applied Force	137
4.1.6. Definitions of External Force, Forward Force and Backward Force	138
4.2. Twinning Dislocation Distribution Within A Thin Twin Layer	139
4.3. Force Calculation	144
4.3.1. Calculation of Forward Force F_f	144
4.3.2. Calculation of Backward Force F_b	148
4.3.3. Calculation of External Force F_{ex}	155
4.4. Stresses in The Thin Twin Layer	157
4.5. Simplified Equations for F_f , F_b and F_{ex}	162
4.6. Discussion	168
4.6.1. Stress and Force Distributions Within The Twin Layer.....	168
(a) External Stress τ_{ex}	168
(b) Forward Stress τ_f	169
(c) Back Stress τ_b	170

4.6.2. Dislocation Distribution in The Case of Equal	
Backward Force on Each Twinning Dislocation.....	175
4.6.3. Effect of Dislocation Location on The Stress Distribution.....	176
4.7. Summary	178
 CHAPTER FIVE. MECHANICAL TWINNING DURING	
CREEP DEFORMATION IN TiAl	183
5.1. Introduction	183
5.2. Material and Experimental Procedure	184
5.3. Results	186
5.3.1. Optical Microstructure	186
5.3.2. Cross Twinning and Parallel Twinning in Lamellar Grains	187
5.3.3. Fine Mechanical Twins at Grain Triple Points	190
5.4. Analysis and Discussion	194
5.4.1. Cross Twinning in Lamellar Grains	194
5.4.2. Cross Twinning in Equiaxed γ Grains	202
5.4.3. Fine Mechanical Twins at Equiaxed γ Grain Triple Points	203

(a) Fine Mechanical Twins Formed by Accommodation of Stress Concentration at Equiaxed γ Grain Triple Points	203
(b) Formation of Fine Mechanical Twins Prevents Grain Boundary Sliding	204
(c) On DO ₁₉ Crystal Structure in Fine Mechanical Twins	207
5.5. Conclusions	209
 CHAPTER SIX. CONCLUDING REMARKS AND	
RECOMMENDED FUTURE WORK	211
 LIST OF REFERENCES	 214

LIST OF TABLES

Table 2.1. Dislocation behavior in TiAl at different temperature ranges	18
Table 2.2. Twinning modes in cubic lattices	36
Table 2.3. Twinning modes in cubic lattices	58
Table 2.4. Possible true twinning modes in cubic superlattices	60
Table 2.5. Twinning modes in non-cubic superlattices	61
Table 2.6. Twinning modes in hcp metals	66
Table 2.7. Creep Deformation Mechanisms At Temperature $T/T_m \geq 0.4$	79
Table 3.1. Composition of the γ TiAl specimen	83
Table 3.2. The mechanical twinning elements in Fig. 3.1	93
Table 3.3 Schmid factors on all possible twinning systems within the (111) plane	93
Table 4.1. The distance of twinning dislocations from the twin tip	143
Table 4.2 The forces on each twinning dislocation	149
Table 4.3 The stresses at each twinning dislocation	160
Table 4.4 The forces calculated using simplified equations	166
Table 4.5 The modified stresses and forces for the first three twinning dislocations	171
Table 5.1. Schmid Factors for Mechanical Twinning Systems in γ/γ Lamellae	199
Table 5.2 Misorientation and Grain Boundary Structure of Grains at the Grain Triple Point	205

LIST OF FIGURES

Figure 2.1 - Unit cell of superlattice $L1_0$	7
Figure 2.2 - Phase diagram of TiAl	8
Figure 2.3 - Stacking fault configurations as viewed along $[\bar{1}10]$. (a) APB, (b) SISF, (c) CSF, (d) SESF(I), and (e) SESF(II)	9
Figure 2.4 - Crystal projection as viewed along $[111]$. b_A is a crystal vector which results in an APB, b_C results in a CSF, and b_S results in a SISF	12
Figure 2.5 - Thompson tetrahedron. The primed letters indicate the antisites with respect to the unprimed letters	12
Figure 2.6 - Dislocations in superlattice $L1_0$	15
Figure 2.7 - Glissile configurations of superdislocations. The single line is a SSF, the jagged line is an APB, and the double line is a CSF	19
Figure 2.8 - Roof-type blocking configurations. The single line is a SSF, the jagged line is an APB, and the double line is a CSF	19
Figure 2.9 - Kear-Wilsdorf blocking configurations. The dashed line is the APB in the $\{001\}$ plane, and the single line is the SSF in the $\{111\}$ plane	20
Figure 2.10 - The Peierls relief along different crystallographic directions in TiAl	22
Figure 2.11 - Schematic diagram of the row of broken Ti-Ti bonds	23
Figure 2.12 - Formation of SSF-tube blocking. (a) Formation of nonaligned jogs on a superdislocation; (b,c) formation of a dipole; (d) a SSF-tube along $[101]$ direction	24

Figure 2.13 - Definition of orientation variants in $(\gamma + \alpha_2)$ lamellae	30
Figure 2.14 - Relations between c_i and p_i	39
Figure 2.15 - The sign of four twinning elements	41
Figure 2.16 - The rationality of K_1 in type-I twinning	42
Figure 2.17 - Schematic illustration of lattice shuffling during type-I twinning for the of $q = 4$	46
Figure 2.18 - Lattice point displacement during twinning shear	49
Figure 2.19 - The extension and contraction of sample length for twinning in zinc	51
Figure 2.20 - The structure and interchange shuffles during $(\bar{1}20)$ twinning in DO_3	56
Figure 2.21 - Dislocation pole mechanism for twinning in bcc lattice	64
Figure 2.22 - $(\bar{1}02)$ twinning in zirconium. Projection of the lattice on the $(12\bar{1}0)$ plane. Circles are in plane of the paper. Squares are $a/2$ above and below the paper. Solid symbols indicate atom positions in the twin	65
Figure 2.23 - Dislocation pole mechanism in fcc lattice	67
Figure 3.1 - Mechanical twinning propagation configuration which was observed <i>in situ</i> in TiAl: (a) the tilted image of fine mechanical twins within a grain interior; (b) the image of fine mechanical twins viewed parallel to the twinning plane; (c) the diffraction pattern across several fine twin layers; and (d) indexes of the diffraction pattern which shows a twin relationship across the twin-matrix interfaces	86
Figure 3.2 - Schematic diagram of mechanical twinning nucleation and propagation procedure in TiAl, which shows that the mechanical twinning nucleates at a grain boundary and propagates into the grain interior. (a) and (b) are the configuration of mechanical twinning nucleation at the grain boundary with the emission of one twinning dislocation from the grain boundary; (c) and (d) are the same configuration as (a) and (b) except that two twinning dislocations are emitted from the grain boundary simultaneously;	

(e) is an intermediate state of twinning propagation; and (f) is the final state in which the twinning propagation ceases in the grain interior as twin layers "A" and "B" in Fig. 4.1 (a)	89
Figure 3.3 - Schematic diagram of the incoherent twin boundary structure in terms of individual twinning dislocations, which is viewed in [110] direction. The boundary between the first dislocation and the second dislocation at the twin tip is an intrinsic stacking fault, the boundary between the second and the third dislocations is an extrinsic stacking fault, and the boundary between any two adjacent dislocations after the third dislocation is a twin plane. The twinning dislocations are denoted by numbers: the leading dislocation at the twin tip is counted as the first dislocation, the one just behind it is the second one, and so on	92
Figure 3.4 - Crystal orientation relationships of the twinning elements and the possible twinning directions in (111) plane. The cross mark indicates the direction of creep tensile axis	94
Figure 3.5 - Schmid factor contours with respect to the twinning system of (111)[112], which indicates that a tensile principal stress should be in the vicinity of [551] crystal direction in order to operate the (111)[112] twinning system	96
Figure 3.6 - Mechanical twinning propagation mechanism in TiAl, which shows the twin layers resulting from the glide of (a) one, (b) two, (c) three, and (d) four twinning dislocations in the (111) twinning plane during the twinning propagation. The left side column is the glide sequence of $1/6[112]$ twinning dislocations. The middle column is the atomic arrangements of resultant twins viewed in [110] direction, in which the open circles indicate the atoms located in the plane of the paper and the shaded squares indicate the atoms in the plane just beneath the paper. The right side column is the atomic stacking sequences along [111] direction before and after twinning, in which the primed letters indicate the sheared planes	97
Figure 3.7 - The sequences of mechanical twinning nucleation and propagation in TiAl	101
Figure 3.8 - (a) The side view of twin layers A, B, C, and D in Figure 4.7, and (b) the diffraction pattern taken across these twin layers	104
Figure 3.9 - The thin twin morphology near the twin tip	108

Figure 3.10 -	The configuration of fine mechanical twins resulting from the accommodation of local stress concentration at a grain triple point (a). Diffraction pattern across the interfaces (b) shows that these fine laths are twin-related with matrix and the existence of fine DO₁₉ phase between them (c). Diffraction pattern taken in untwinned area within the same grain without tilting the sample (d) shows that the untwinned region has the same crystal orientation as the matrix of fine mechanical twins as shown in (b). (e) is the indexes of (d). It also shows that the growth of fine mechanical twins as pointed out with an arrow between the completely developed fine twins and the matrix stopped in the grain interior	110
Figure 3.11 -	(a) shows three thin twin layers indicated by letters "A", "B" and "C" within a γ grain interior, which indicates that the nuclei of these twin layers were formed inside the γ grain; (b) is a diffraction pattern taken across the twin layer	119
Figure 4.1 -	Forces on individual twinning dislocation in the thin twin layer. (a) On the first twinning dislocation, (b) on the second one, (c) on the third, and (d) on the fourth	129
Figure 4.2 -	(a) Variation of Peierls energy as a function of transverse displacement (u), (b) Variation of the lattice friction stress. ($W_o \approx Gb^2$)	135
Figure 4.3 -	(a) is the amplified image of a thin twin layer and (b) is a schematic drawing of the twinning dislocation distribution in the thin twin layer	141
Figure 4.4 -	The distance of twinning dislocations from the twin tip	145
Figure 4.5 -	The forces distribution along the twin layer	150
Figure 4.6 -	Shear stresses distribution in the thin twin layer	161
Figure 4.7 -	Comparisons of results obtained from the original equations with results obtained from the simplified equations	167
Figure 4.8 -	The modified stress distribution along the thin twin layer	172
Figure 4.9 -	The modified force distribution along the thin twin layer	173

Figure 4.10 - Dislocation distribution at equal backward force on every twinning dislocation. ($F_t/Gb = 1.18 \times 10^{-2}$)	177
Figure 4.11 - Effect of the twinning dislocation location on the backward stress. (a) For the second dislocation, (b) for the third dislocation, and (c) for the tenth dislocation	179
Figure 5.1 - Optical micrographs of (a) initial microstructure and (b) after creep deformation	186
Figure 5.2 - (a) Cross twinning configuration in a lamellar grain, (b) diffraction pattern of the original lamellae, and (c) orientations of the original lamellae	188
Figure 5.3 - Cross twinning configuration within a large equiaxed γ grain	191
Figure 5.4 - Fine mechanical twin configurations at equiaxed γ grain triple points	192
Figure 5.5 - Fine mechanical twins (a), diffraction pattern across several fine twin interfaces (b), and twin relation in the diffraction pattern (c)	193
Figure 5.6 - Atomic arrangement of true-twinning (a) and pseudo-twinning (b)	196
Figure 5.7 - Stereographic projection of possible twinning systems along [110] direction	198
Figure 5.8 - Schematic mode of cross twinning: (a) initial condition of two lamellae; (b) metastable condition of twinning in lamellae 1; (c) final configuration of cross twins as seen in Fig. 5.2 (a)	200
Figure 5.9 - Fine mechanical twins from accommodation of local stress concentration (a), twin end configuration at equiaxed γ grain boundary (b), and dislocation slip near zigzagged boundary (c)	206
Figure 5.10 - Boundary between an equiaxed γ grain and a lamellar grain	208
Figure 5.11 - Optical microstructure showing the roughness of lamellar grain boundaries	208

CHAPTER ONE

INTRODUCTION

Gamma titanium aluminide (TiAl) is a promising candidate material in high temperature and high performance applications for its high strength, low density, good oxidation resistance, and excellent high temperature mechanical properties. The main barrier for application in practice is its brittleness at room temperature ^[1-3]. In the last decade, most of the research effort in TiAl has been concerned with fundamental studies of dislocation structures in single phase materials ^[4-10]. More recent studies on Ti-rich alloys consisting of two phases ($\gamma + \alpha_2$) which present better room temperature ductility have also been focused mainly on the dislocation structures ^[11-16]. However, experimental results have shown that mechanical twinning is an important deformation mechanism in TiAl both at room and high temperatures ^[17-29]. Particularly, under creep deformation conditions, mechanical twinning contributes significantly to the creep deformation ^[1,28-31].

Titanium aluminide TiAl has a $L1_0$ ordered face centered tetragonal structure. The mechanical twins observed are of the $\{111\} \langle \bar{1}1\bar{2} \rangle^*$ type which are the variants in

* The notations "<" and ">" in the indexes indicate that the two indexes nearest to "<" or ">" are permutable one to another without changing its properties.

which the $L1_0$ superlattices are mechanically twinned without disturbing the $L1_0$ crystal structure. It has been reported that when the $L1_0$ structure is homogeneously sheared by the variants other than $\{111\} \langle \bar{1}1\bar{2} \rangle$ type, the $L1_0$ structure will be changed into a $L1_1$ superlattice structure ^[1]. Based on this concept, the twinning operation by the variants other than $\{111\} \langle \bar{1}1\bar{2} \rangle$ is thought to be forbidden ^[2,3]. The details of mechanical twinning behavior and its contribution to the deformation in TiAl are not completely understood at present.

No fundamental investigations on mechanical twinning in TiAl have been carried out until the very recent work done by Farenc, Coujou and Couret ^[32] on twin propagation in TiAl, by Wardle, Phan and Hug ^[33] and by Sun, Hazzledine and Christian ^[34,35] on twin intersections. Farenc, Coujou and Couret first investigated *in situ* mechanical twin propagation at room temperature and at 400 °C. They found that "twins are formed by $a/6 \langle \bar{1}1\bar{2} \rangle$ partial dislocations gliding in octahedral planes" and the twin propagation is due to "a partial dislocation turning around a perfect dislocation". However, the material used in their study was an aluminum rich $Ti_{46}Al_{54}$ single γ phase alloy. The basic properties of Al-rich alloys (single γ phase) are inherent brittleness at room temperature ^[1-3,15], but the γ phase in the $\gamma + \alpha_2$ lamellar structure has been found to be intrinsically ductile ^[36]. Therefore, the mechanical twinning behavior and its role in the deformation in Al-rich single phase alloys may differ from those in Ti-rich two phase alloys. This is because the stacking fault energies of γ phase in Al-rich single γ phase and in Ti-rich $\gamma + \alpha_2$ lamellar grain are different ^[36]. The twin intersection has been comprehensively studied by Wardle, Phan and Hug ^[33] for both Al-rich and Ti-rich

alloys at room temperature and by Sun, Hazzledine and Christian ^[34,35] for an alloy of stoichiometric composition (50Ti - 50Al at. %) in the temperature range -196 °C to 900 °C, respectively. In Wardle, Phan and Hug's work ^[33], two different twin intersections were observed and it was found that the structures of twin intersections depended on "the orientation of the common direction of the twin habit planes". Similarly, in Sun, Hazzledine and Christian's work ^[34,35], two types of twin intersections have been found: type I intersection occurs along $\langle 110 \rangle$ directions while type II intersection occurs along $\langle 011 \rangle$ directions. In the type I intersection, two different configurations are observed depending on the deformation temperatures: (i) At room temperature, one twin band is deflected and the other remains rectilinear. The lattice in the intersection region remains in $L1_0$ structure and is congruent with the lattice of the deflected twin; (ii) at high temperature, both twin bands are deflected. In type II intersection, both twin bands are deflected at both room and high temperatures. Type II intersection has been found to be associated with $\frac{1}{2} \langle 110 \rangle$ dislocations in the twin-matrix interface.

However, all these fundamental studies on mechanical twinning have been carried out on the specimens deformed at common tensile testing strain rates, for example, the strain rate in [34] was $5 \times 10^{-5} \text{ s}^{-1}$, which is much faster than normal creep strain rates. Therefore, these observations may not be directly applicable to creep deformation.

For mechanical twinning in creep deformation, very limited research has been reported ^[22, 28-31, 37-39]. Also, there are two differing results concerning twinning in creep deformation of TiAl. Loiseau and Lasalmonie ^[22] investigated creep deformation of

equiaxed single phase γ $\text{Ti}_{46}\text{Al}_{54}$ and found that twinning was an important creep deformation mechanism at deformation temperatures up to 800 °C. Jin and Bieler ^[28-31] have found that mechanical twinning is significant in creep deformation at 765 °C for Ti-rich alloy (Ti-48Al-2Nb-2Cr). However, Huang and Kim ^[39] studied creep behavior of two phase $\gamma + \alpha_2$ alloy with composition of Ti-47.0Al-1.0Cr-1.0V-2.5Nb at 900 °C and observed no evidence of twinning in creep deformation. Pseudo-twinning, which was thought to be "forbidden" in the literature ^[25,40] and it will be discussed later, was found in a creep deformed TiAl specimen ^[28].

In addition, the creep deformation mechanisms are not clear at present. The activation energies for creep of TiAl are much larger than those for self-diffusion and interdiffusion in TiAl ^[39,41,42], which indicate that the creep rate may be controlled by some processes other than diffusion. The reported values of the stress exponents vary widely from about 2 to 8 ^[43-46]. This indicates that several deformation mechanisms may be involved in creep deformation of TiAl. Mechanical twinning has been found to be an important creep deformation mechanism ^[22, 28-31, 37,38], but mechanical twinning is influenced very little by diffusion processes, and dislocation configurations in creep specimens are similar to those observed in short term tensile specimens ^[6,9]. All these indicate that mechanical twinning may play an important role in the creep deformation of TiAl.

Based on the above circumstances, investigations of twin nucleation and propagation in creep deformed TiAl and the contributions of mechanical twinning to

creep deformation of TiAl have been carried out in this study. At first, the basic understanding of TiAl, the intensive twinning theory and a brief introduction of creep theory has been summarized in Chapter Two. In Chapter Three, *in situ* observations of mechanical twin nucleation and propagation in a creep deformed specimen are presented. The mechanical twinning was observed to nucleate either at grain boundaries or at twin interfaces due to the local stress concentration. The nucleus was either a superlattice intrinsic stacking fault which resulted from the emission of one twinning dislocation from the grain boundaries or the twin interfaces, or a superlattice extrinsic stacking fault resulting from the emission of two twinning dislocations. The twinning dislocation was identified to be Shockley partial $1/6 \langle 11\bar{2} \rangle$ and twinning plane was identified as (111). The twinning propagation mechanism was a homogeneous glide of twinning dislocation on every adjacent twinning plane. The stress state necessary for twinning propagation is that the principal stress axis must be orientated in the vicinity of $[55\bar{1}]$ crystal orientation in the case of tensile stress state.

The force and stress analysis on a thin twin layer is presented in Chapter Four. The result shows that both the forward stress and the back stress are very large at the twin tip and decrease quickly as the distance from the twin tip increases. At very large distances from the twin tip, both stresses tend to be constant. The external stress on the investigated twin layer was found to be a residual stress in the matrix. In the case of no external load and small residual stress, the twin propagation is controlled by the emission of twinning dislocations.

In Chapter Five, some characterizations of mechanical twins in creep deformed specimens are presented. The results show that mechanical twins are formed by either true-twinning or pseudo-twinning. The mechanical twinning in creep deformation of TiAl obeys the maximum resolved shear stress criterion. Stress concentrations at grain triple points can be accommodated by forming fine mechanical twins. The zigzagged grain boundary formed by mechanical twinning can inhibit grain boundary sliding. The formation of fine mechanical twins are probably controlled more by the local stress concentration than by an externally applied stress.

In the last chapter, Chapter Six, some general concluding remarks and some recommended future work are stated.

CHAPTER TWO

THEORY

Some basic understanding of titanium aluminide TiAl, mechanical twinning theory and creep theory will be summarized in this chapter.

2.1. Titanium Aluminide TiAl

2.1.1. Crystal Structure

Titanium aluminide TiAl has a $L1_0$ ordered face centered tetragonal structure with a composition range of 49-66 atomic percent of aluminum, which varies depending on temperature ^[47-49]. The Titanium and aluminum atoms alternately stack in (002) plane,

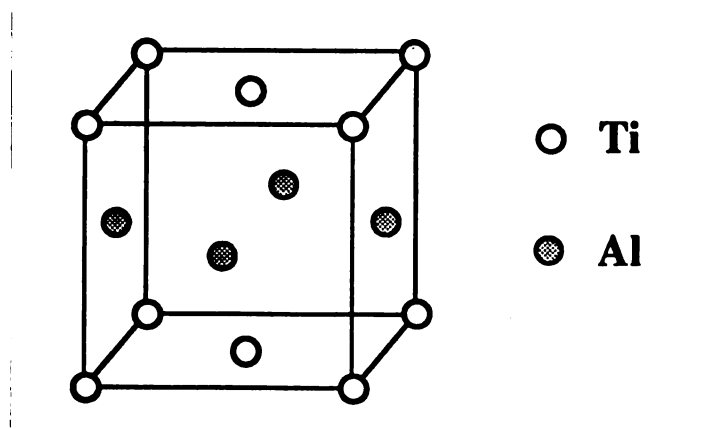


Figure 2.1 - Unit cell of superlattice $L1_0$.

as shown in Fig. 2.1. At the stoichiometric composition, the c/a ratio is 1.02 and the tetragonality increases up to $c/a=1.03$ with increasing aluminum concentration and decreases to 1.01 with decreasing aluminum concentration ^[50-52]. At off stoichiometric composition, excess titanium or aluminum atoms occupy antisites without creating vacancies ^[53]. The TiAl phase remains ordered up to its melting temperature of about 1450 °C as shown in Fig. 2.2 ^[49], which shows a central portion of the equilibrium Ti-Al phase diagram.

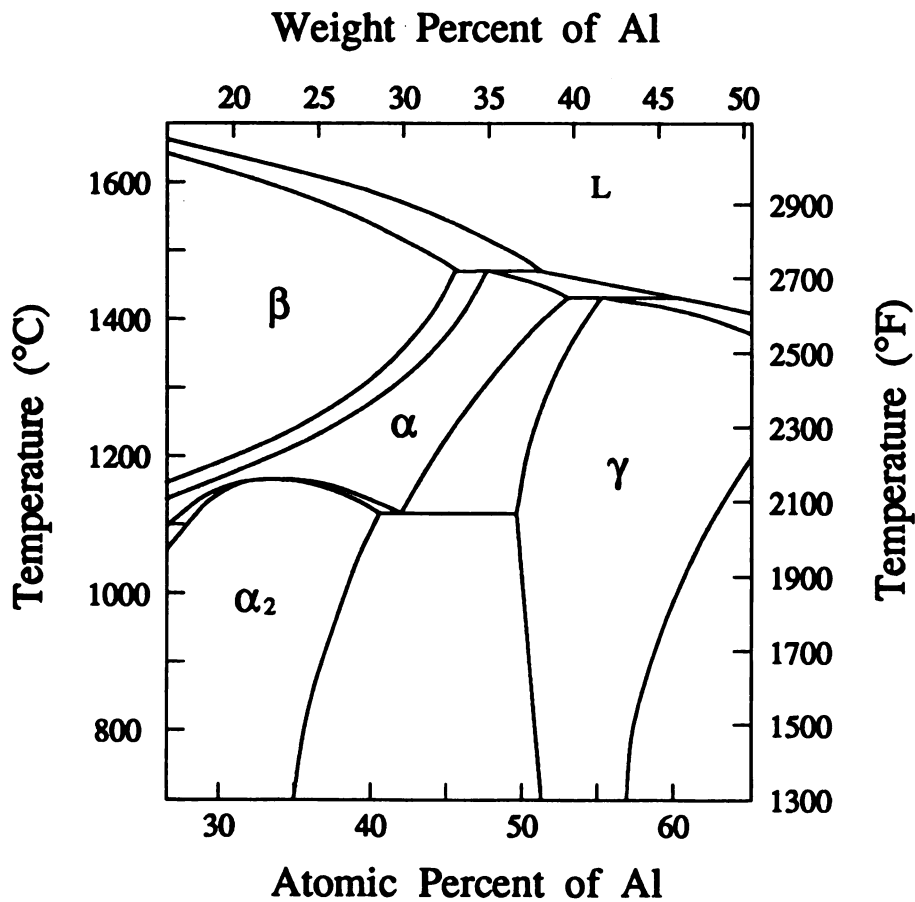


Figure 2.2 - Phase diagram of TiAl.

2.1.2. Stacking Faults

Since TiAl has $L1_0$ structure with ratio $c/a=1.02$, it is very close to the fcc structure. Like the fcc crystal, the geometric stacking sequence along $\langle 111 \rangle$ direction is

A B C A B C A B C A B C

There exist four types of stacking faults in the TiAl crystal structure, i.e., they are antiphase boundary (APB), superlattice intrinsic stacking fault (SISF), complex stacking fault (CSF) and superlattice extrinsic stacking fault (SESF). The atomic configurations of these stacking faults are shown in Fig. 2.3, which are viewed along $[\bar{1}\bar{1}0]$ direction.

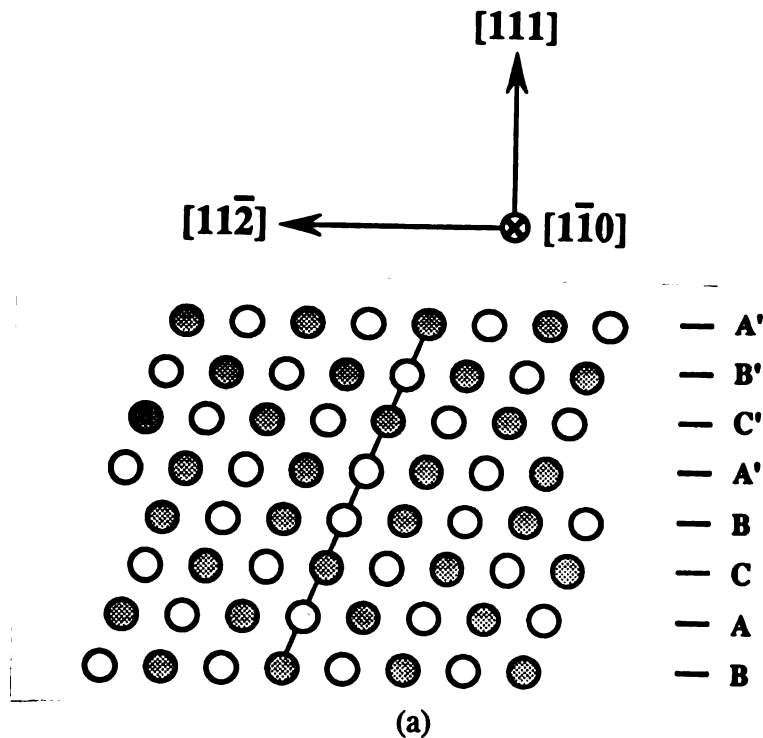
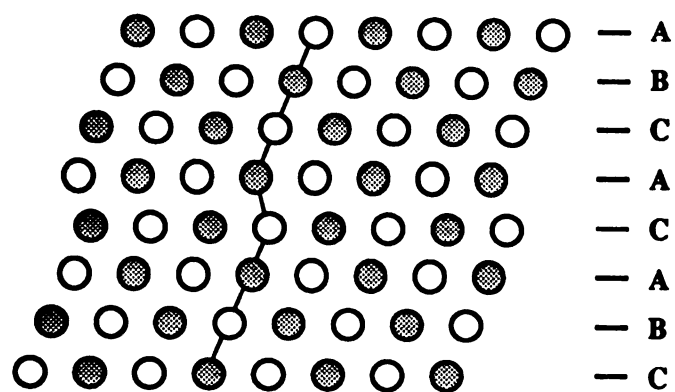
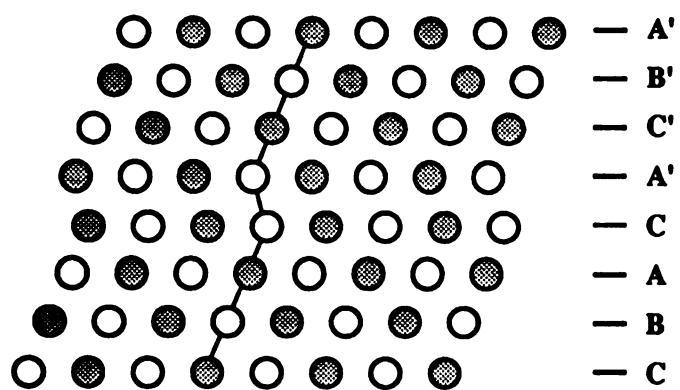


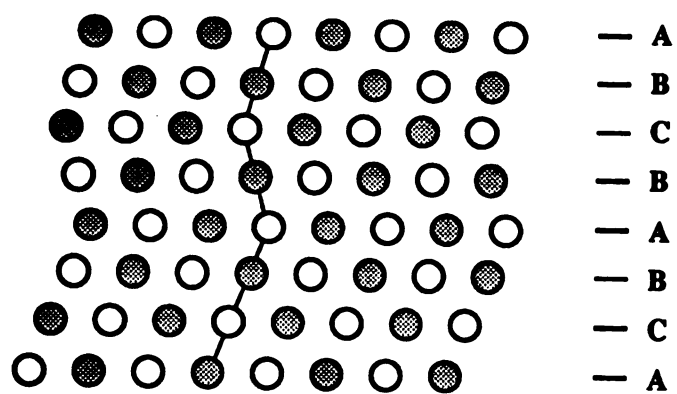
Figure 2.3 - Stacking fault configurations as viewed along $[\bar{1}\bar{1}0]$. (a) APB, (b) SISF, (c) CSF, (d) SESF(I), and (e) SESF(II).



(b)

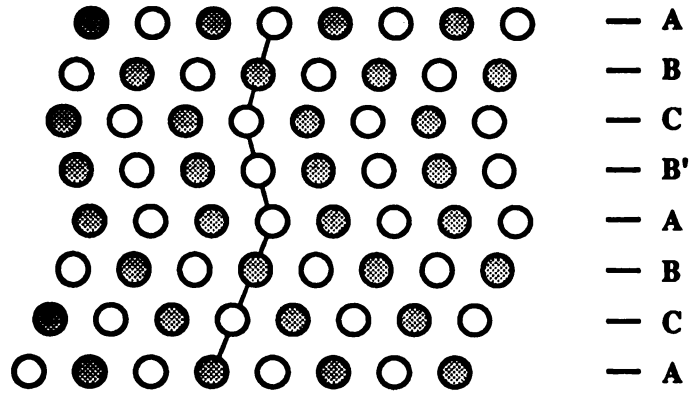


(c)



(d)

(Figure 2.3 continued)



(e)

(Figure 2.3 continued)

(a) APB (Antiphase Boundary)

The APB is created by the glide of a slip vector $D'A$ (or $C'A$), which is shown in Fig. 2.4 by a crystal vector b_A . Fig. 2.4 shows an atomic arrangement in a (111) crystal plane where the stacking sequence is labeled with a, b, c. The slip vector $D'A$ (or $C'A$) is shown in Thompson tetrahedron in Fig. 2.5. In this case the stacking sequence across the APB changes into the following one:

$$A B C A B C | A' B' C' A' B' C'$$

where the primed letters indicate the displaced planes with respect to the unsheared crystal that is indicated by letters without primes (it will be the same in the following).

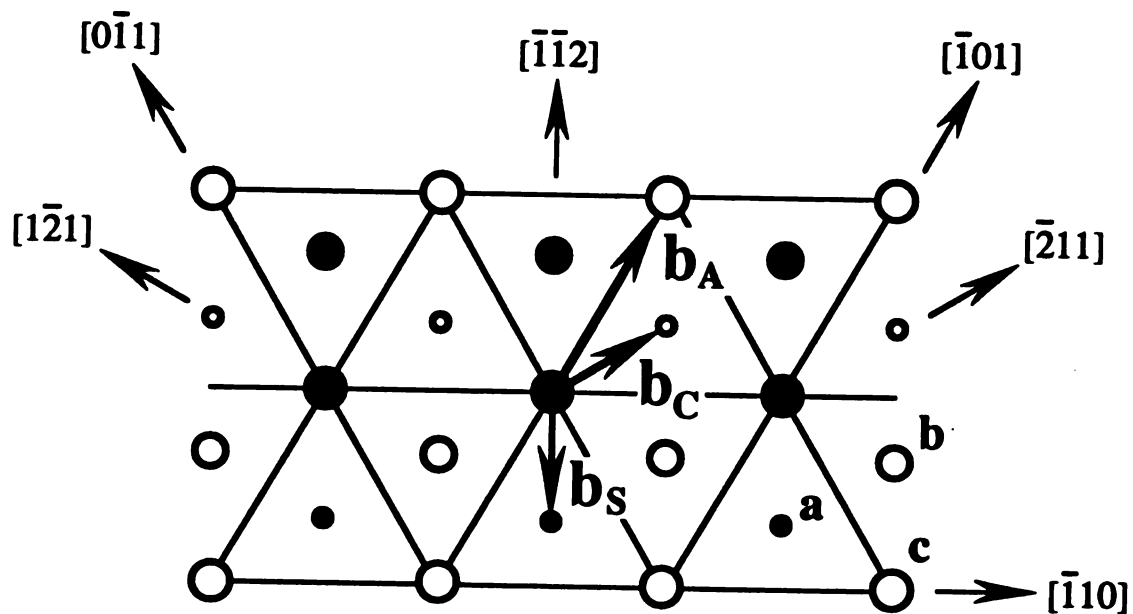


Figure 2.4 - Crystal projection as viewed along $[111]$. b_A is a crystal vector which results in an APB, b_C results in a CSF, and b_S results in a SISF.

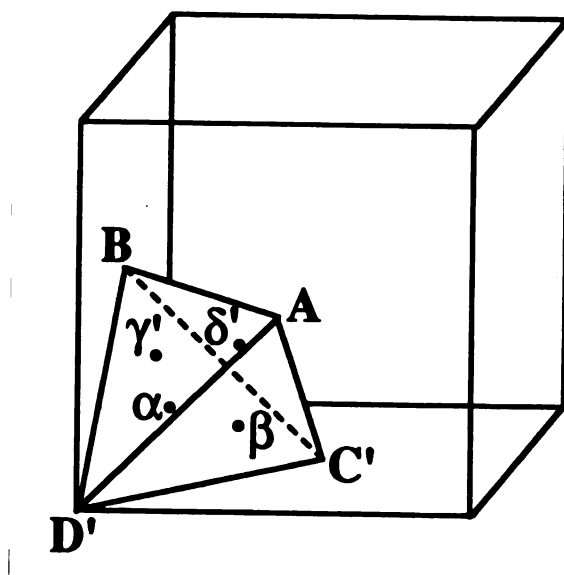


Figure 2.5 - Thompson tetrahedron. The primed letters indicate the antisites with respect to the unprimed letters.

It is more visible if one looks at the shear displacement in the $[1\bar{1}0]$ direction, which is shown in Fig. 2.3. In Fig. 2.3 (a), one can easily find the antiphase boundary configuration which lies in the (111) plane.

(b) SISF (Superlattice Intrinsic Stacking Fault)

The SISF is very common in TiAl. The SISF is formed by the glide of a slip vector βA in Fig. 2.5 or by a crystal vector b_s in Fig. 2.4. If one looks at the stacking sequence order, the SISF is formed by taking off one plane from the original stacking sequence as the following:



In Fig. 2.3 (b), it can be seen that the atoms in the upper half of the crystal shift to the left with respect to the lower half in an amount of βA .

(c) CSF (Complex Stacking Fault)

The CSF is created by the glide of $\beta D'$ (or $\beta C'$) in Fig. 2.5, which is shown in Fig. 2.4 with a crystal vector b_c . The stacking sequence after shearing is



From Fig. 2.3 (c), it is found that it has an antiphase boundary feature in addition to Fig. 2.3 (b) like configuration. Therefore, the CSF energy may be equal to APB energy plus

SISF energy.

(d) SESF (Superlattice Extrinsic Stacking Fault)

There are two possibilities to form the SESF. (i) The SESF is formed by the glide of two βA in successive close-packed planes (type I). This type SESF looks like the effect of inserting one extra plane between two original planes,



which is shown in Fig. 2.3 (d). (ii) The SESF is formed by the glide of slip vectors $\beta D'$ and $\beta C'$ (type II). The type II configuration is shown in Fig. 2.3 (e). Comparing type I and type II configurations in Fig. 2.3 (d) and (e), it is easily found that type I is more stable than type II because type II includes an APB feature.

2.1.3. Dislocations and Dislocation Core Structures

There are four types of dislocations in TiAl due to its ordered crystal structure, that is, $1/2 \langle 110 \rangle$ type, $\langle 101 \rangle$ type, $1/2 \langle 112 \rangle$ type and $\langle 100 \rangle$ type, as shown in Fig. 2.6. Here $1/2 \langle 110 \rangle$ dislocations are normal dislocations but both $\langle 101 \rangle$ and $1/2 \langle 112 \rangle$ dislocations are superdislocations and $\langle 100 \rangle$ dislocations are cube dislocations. Notations " \langle " and " \rangle " in the indexes indicate that the two indexes nearest to " \langle " or " \rangle " are permutable one to another without changing its properties. The dislocation core structures are very complicated and they depend on which plane they dissociate into

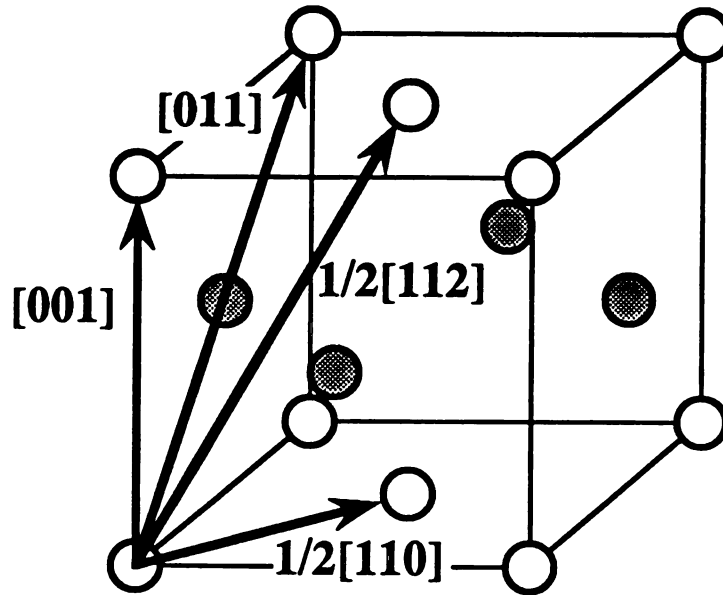
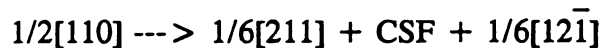
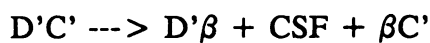


Figure 2.6 - Dislocations in superlattice $L1_0$.

[5,54,55]. The core structure dependence upon temperature is closely associated with the temperature-dependent deformation behavior in TiAl [2]. The typical dislocation dissociation reactions of these four dislocations are listed in the following:

(a) $1/2 \langle 110 \rangle$ Type



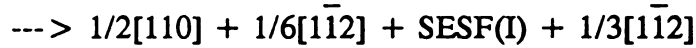
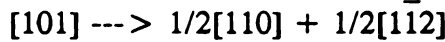
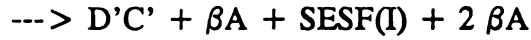
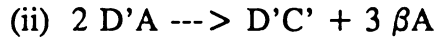
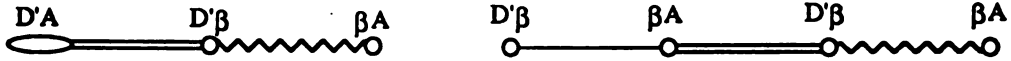
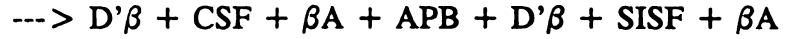
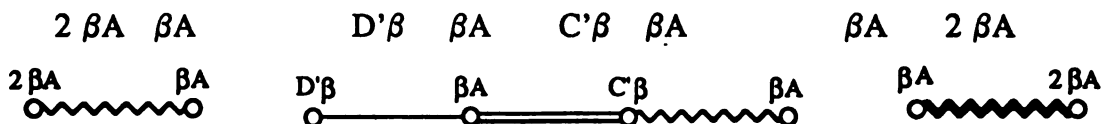
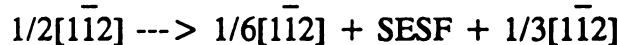
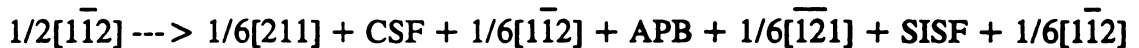
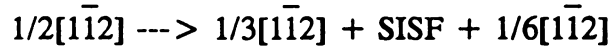
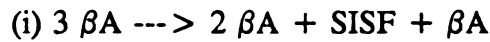
Note that the marks " ————— " is CSF,

" ~~~~~ " is SISF,

" = = = " is APB,

" ~~~~~ " is SESF,

" " is no fault.

(b) $\langle 101 \rangle$ Type(c) $1/2 \langle 112 \rangle$ Type

(d) $\langle 100 \rangle$ Type

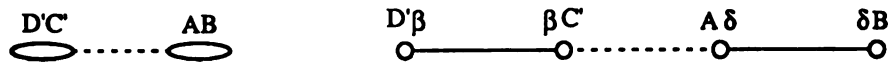
$$D'a^* \rightarrow D'C' + AB$$

$$\rightarrow D'\beta + \text{CSF} + \beta C' + A\delta + \text{CSF} + \delta B$$

where "*" is not a Thompson notation.

$$[100] \rightarrow 1/2[110] + 1/2[1\bar{1}0]$$

or $\rightarrow 1/6[211] + \text{CSF} + 1/6[12\bar{1}] + 1/6[\bar{1}2\bar{1}] + \text{CSF} + 1/6[\bar{2}11]$



The dislocation slip planes in TiAl are close packed $\{111\}$ planes. According to the crystallography of TiAl, dislocations with $1/2\langle 110 \rangle$ or $\langle 101 \rangle$ Burgers vectors can slip in two different $\{111\}$ planes while dislocations with $1/2\langle 112 \rangle$ Burgers vectors can only slip in one $\{111\}$ plane ^[5]. $\langle 100 \rangle$ dislocations may slip on the cube planes at very high temperatures (about 1000 °C) ^[56].

It has been found that dislocation behavior is different at different temperatures.

Dislocations observed in different temperature ranges are summarized in table 2.1.

2.1.4. Dislocation Blocking Mechanisms

TiAl, like many intermetallic compounds, shows an anomalous yield stress-temperature dependence, that is, unlike disordered metals and alloys, the yield stress of TiAl increases as the temperature increases up to about 700 °C. The anomaly of yield stress to temperature results from the glissile-sessile transformations of dislocations in different temperature ranges. The glissile dislocations have coplanar splitting

Table 2.1. Dislocation behavior in TiAl at different temperature ranges ^[5,6,61]

Dislocation	Unblocked	Blocked	Unblocked
$1/2 < 110]$	-196 to 100°C	200 to 540°C	> 600°C
$1/2 < 112]$	-196 to 100°C	200 to 600°C (Not observed)	> 700°C
$< 011]$	-196 to 300°C	400 to 600°C	> 700°C
$< 100 >$	Not observed	Not observed	> 700°C

configurations as shown in Fig. 2.7. The sessile dislocations have various configurations depending on their formation. Some dislocation blocking modes will be summarized in the following.

(a) Roof-Type Blocking

The roof type blocking results from a resplitting of superdislocations from their planar glissile configurations into two $\{111\}$ noncoplanar sessile configurations (like a peaked roof), as shown in Fig. 2.8 ^[54,57]. Of these configurations, the one containing SISF bands on both octahedral planes possesses the lowest energy compared to glissile and other roof-type configurations ^[2,58-60].

In addition, a planar sessile configuration was found for $1/2 < 112]$ dislocations

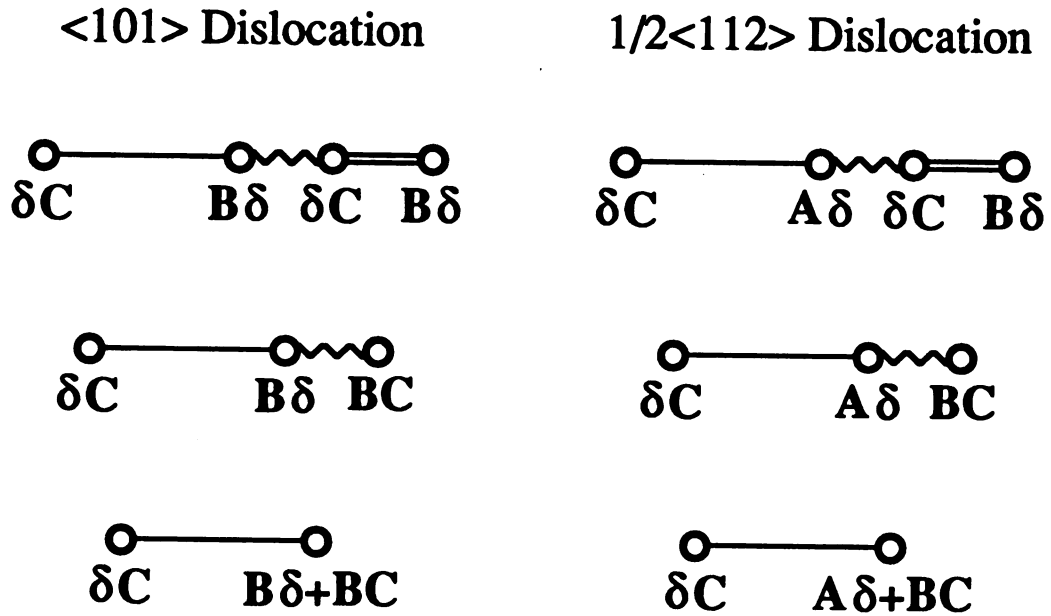


Figure 2.7 - Glissile configurations of superdislocations. The single line is a SISF, the jagged line is an APB, and the double line is a CSF.

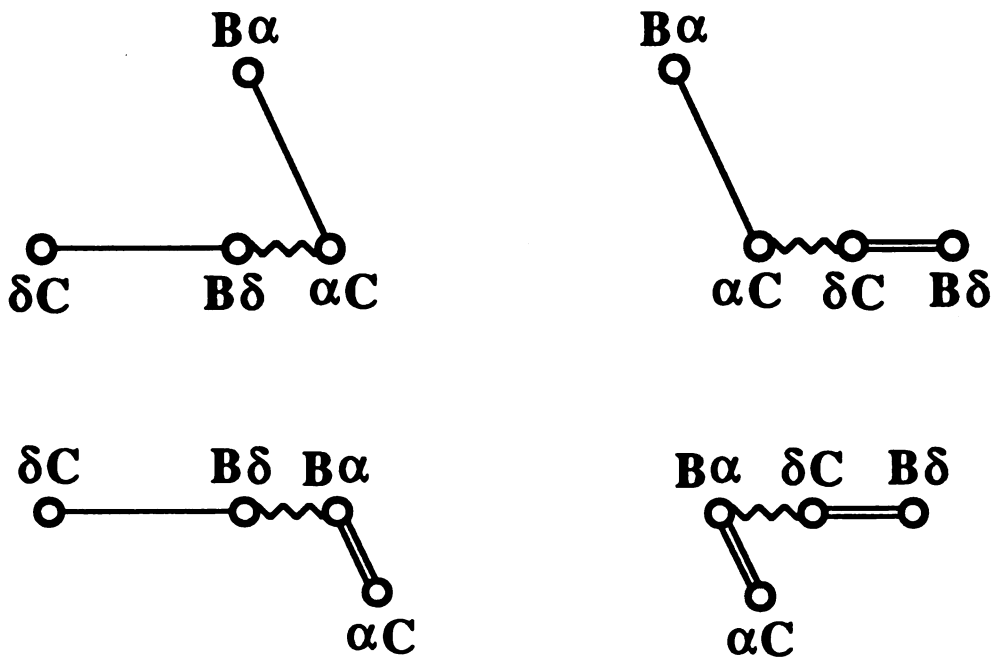


Figure 2.8 - Roof-type blocking configurations. The single line is a SISF, the jagged line is an APB, and the double line is a CSF.

[5,61]. It contains a SESF band bounded by partial dislocations with parallel Burgers vectors $1/6 \langle 112 \rangle$ and $1/3 \langle 112 \rangle$. This configuration forms double layer twin in its core and is strongly blocked.

(b) Kear-Wilksdorf Blocking

The Kear-Wilksdorf blocking occurs as a result of cross slip of superdislocations into the cubic plane, as shown in Fig. 2.9 [59,60]. Since the activation energy for the destruction of Kear-Wilksdorf blocking is very high, the transformation of Kear-Wilksdorf blocking to a glissile configuration is difficult. Taking $1/2 \langle 112 \rangle$ dislocation as an example, this dislocation may dissociate according to the reaction $(C'A + C'B)^{[C'A]} = C'A^{[C'A]} + C'B^{[C'A]}$, where the superscripts indicate the dislocation line directions. Therefore, the screw type $C'A^{[C'A]}$ can glide in (010) cube plane, and the other remains blocked. The $C'A^{[C'A]}$ partial gliding produces APB in (010) plane. Thus, Kear-Wilksdorf blockings of $\langle 011 \rangle$ or $1/2 \langle 112 \rangle$ dislocations can not be destroyed by cubic slip [6,61].

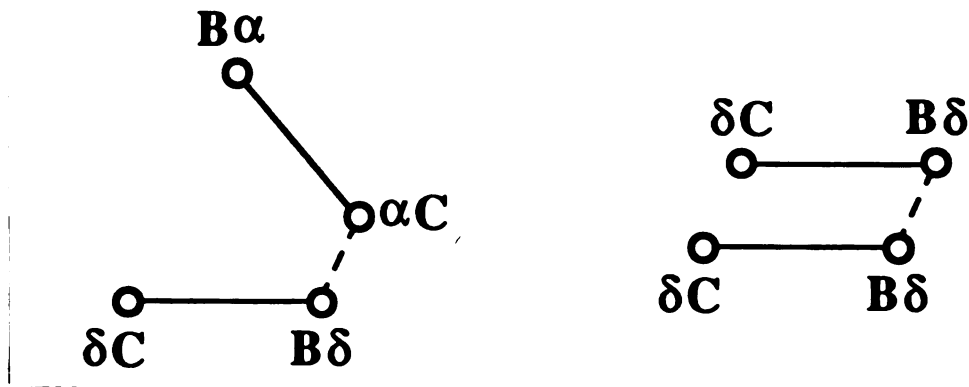


Figure 2.9 - Kear-Wilksdorf blocking configurations. The dashed line is the APB in the $\{001\}$ plane, and the single line is the SISF in the $\{111\}$ plane.

(c) Deep Peierls Valley Blocking

The covalent nature of interatomic bonds in TiAl is the cause of deep (compared to metals) Peierls potential valleys. The deep Peierls valley blocking is based on the formation of directional Ti-Ti bonds along $\langle 110 \rangle$ directions in $[001]$ plane that contains Ti atoms. The slip planes $\{111\}$ in gamma TiAl are equivalent, but the $\langle \bar{1}\bar{1}0 \rangle$ directions on this plane are not equivalent. As a result, two types of directions exist: like atom direction and unlike atom direction as shown in Fig. 2.10 (a). Accordingly, two types of dislocation families exist: one-color-set dislocations (the dislocation lines lie along the rows of like atoms), and two-color-set dislocations (the dislocation lines are parallel to the rows of unlike atoms). The presence of a dislocation of any set gives rise to a row of broken bonds in the (111) slip plane as schematically drawn in Fig. 2.11. However, the other row of covalent bonds lying in the slip plane is parallel to the dislocation line for only the one-color-set. Fig. 2.10 (b) shows the relative Peierls valleys of these two directions. The one-color-set dislocations are in deep energy valleys, and hence are more stable than two-color-set ones which are in shallow valleys.

The dislocations of different sets differ also in the structure of double kinks. For a one-color-set dislocation, the double kink consists of two equivalent kinks that are oriented in two-color-set directions; for a two-color-set dislocation, the double kink contains two nonequivalent kinks: one is in one-color-set direction and the other is in two-color-set direction. Therefore, a transformation from the shallow valleys into the deep valleys is thermodynamically preferred. At low temperatures, dislocations in deep valleys are blocked. As temperature rises until the stress peak, the above transformation

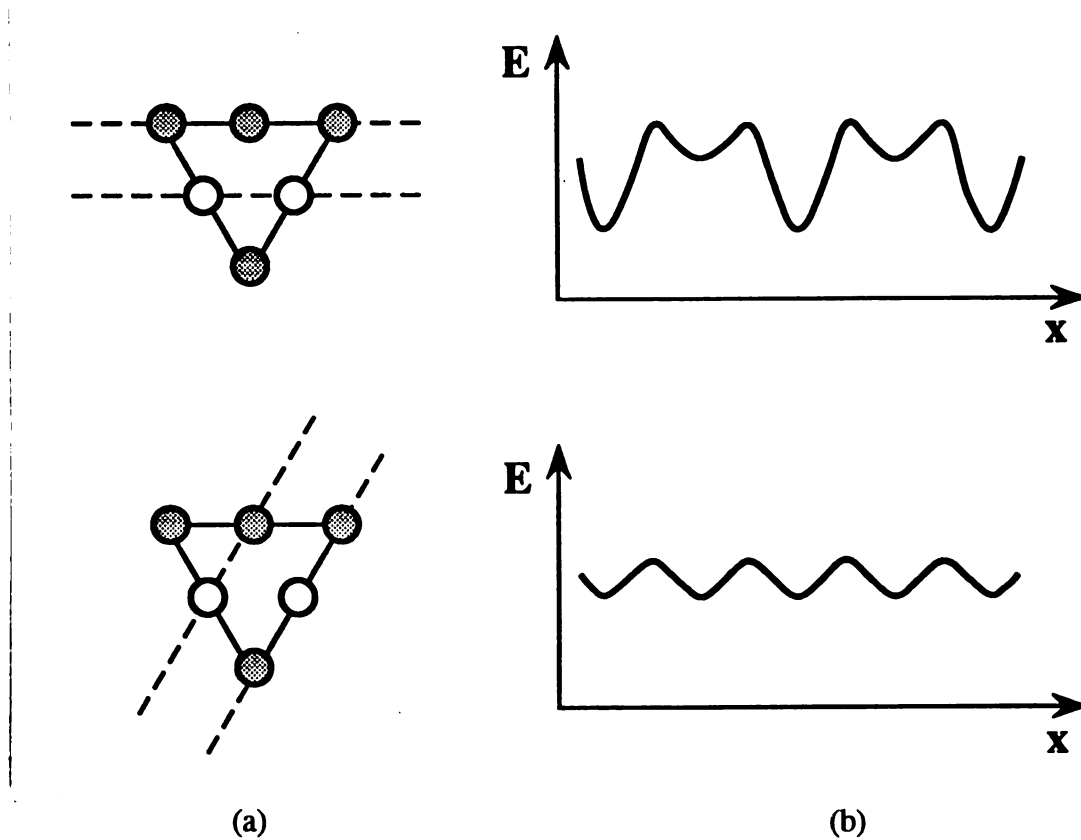


Figure 2.10 - The Peierls relief along different crystallographic directions in TiAl.

is thermally activated and more dislocations are blocked in the deep valleys so as to increase the yield stress. Above the peak temperature, however, the deep valley blocking is thermally destroyed so that the flow stress drops rapidly.

(d) SSF-Tube Type Blocking

The SSF-tube (Superlattice Stacking Fault tube) blocking is also an effective blocking mode. The formation of such a configuration is schematically shown in Fig. 2.12 ^[9]. A slipping superdislocation intersects with the other dislocations to form a jog in the second plane. As a result of splitting, the jog transforms into two nonaligned jogs

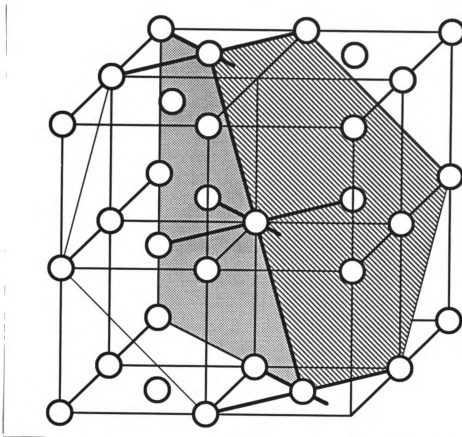


Figure 2.11 - Schematic diagram of the row of broken Ti-Ti bonds. Al atoms are removed for clarity. The gray shaded plane is a terminated half plane of the dislocation and the cross-hatched plane is (111) plane.

on the trailing and leading dislocations. Between them, a SISF band is formed. On the intersection edge of primary and secondary slip planes, stair-rod dislocations with Burgers vector $(A\beta + C\delta)$ are necessary, Fig. 2.12 (a). (Here we did not use the primed letters as used in Fig. 2.5. This will not affect the analysis of SSF-tube type blocking.) As the leading dislocation with Burgers vector δC moves, a dipole arises. However, a similar dipole cannot be formed on the trailing dislocation $2\delta C$, Fig. 2.12 (b). As some part of the trailing dislocation comes into contact with the leading and the stair-rod

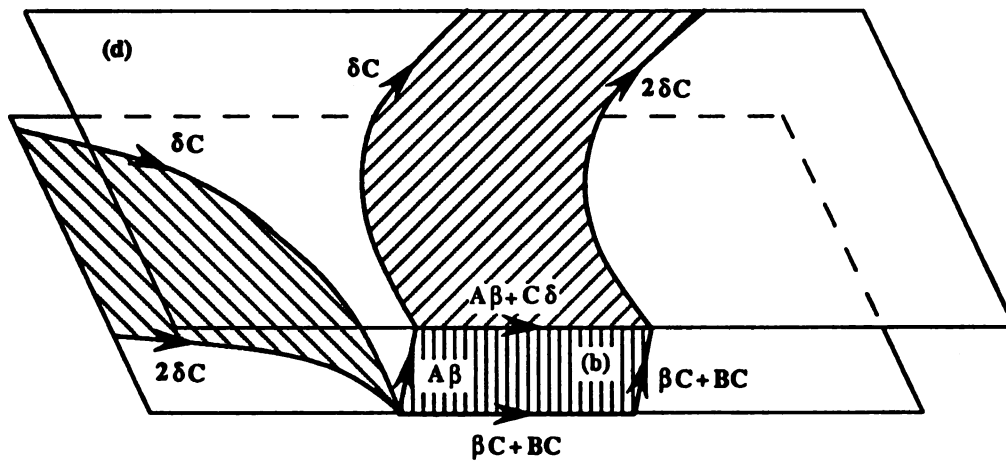
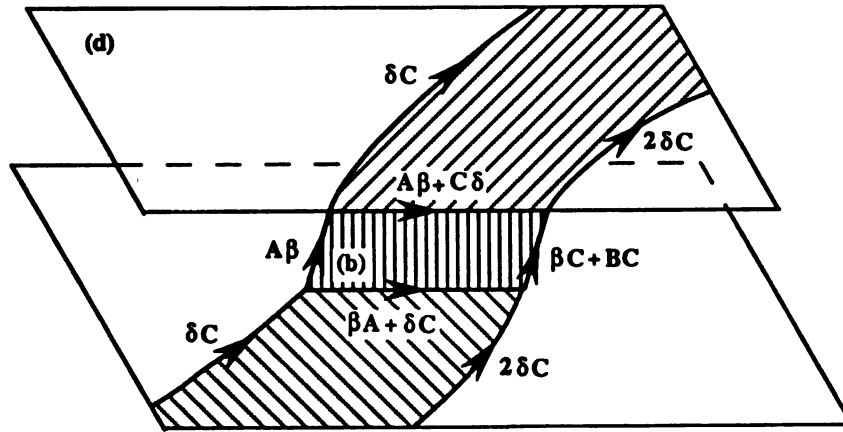
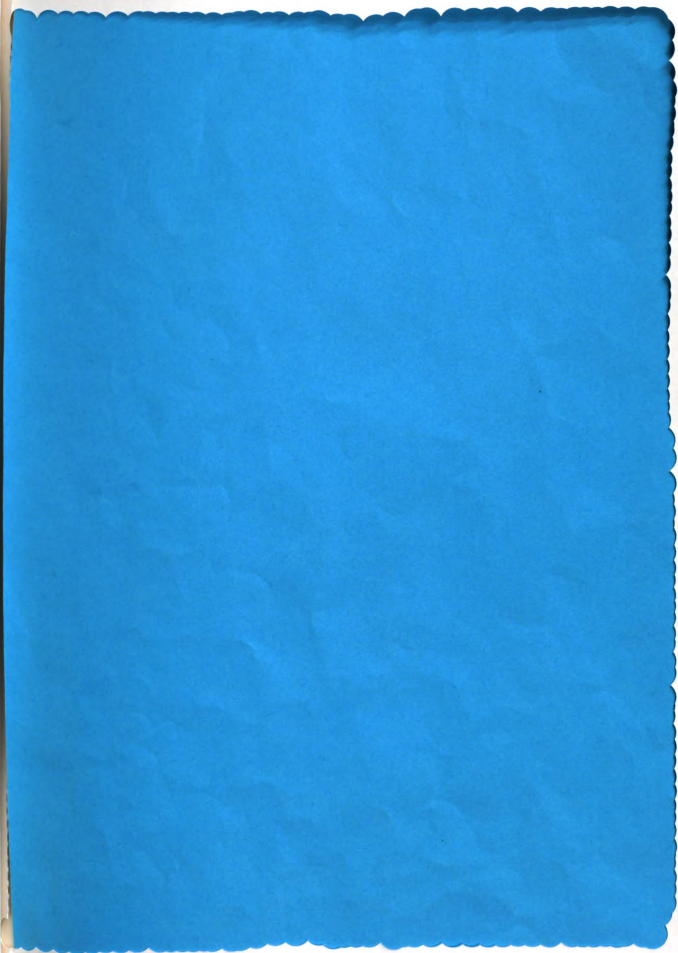
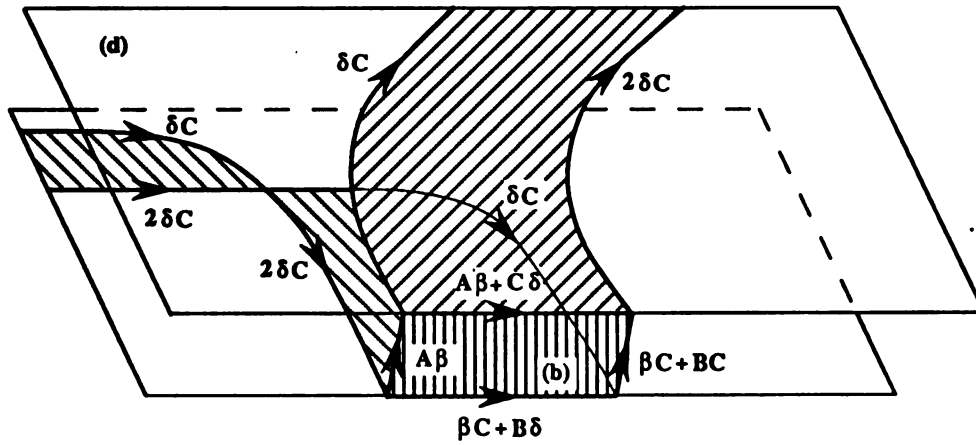


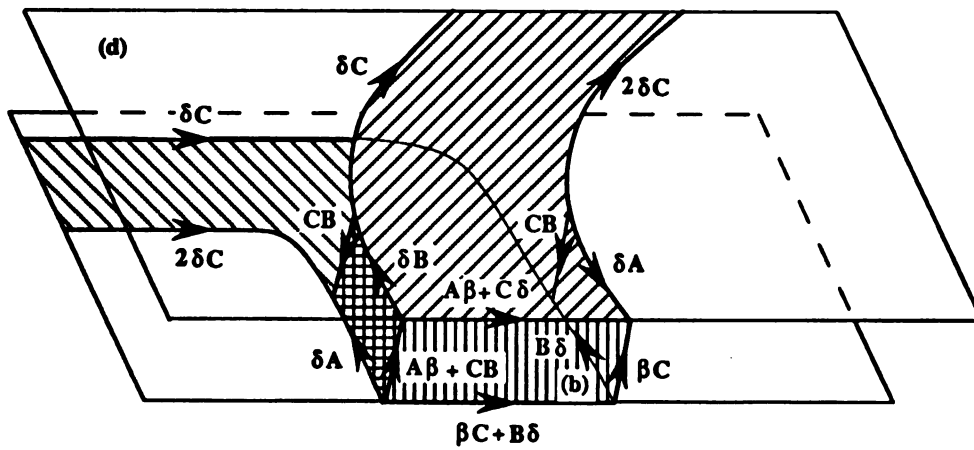
Figure 2.12 - Formation of SSF-tube blocking. (a) Formation of nonaligned jogs on a superdislocation; (b,c) formation of a dipole; (d) a SSF-tube along [101] direction.







(c)



(d)

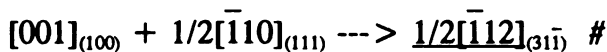
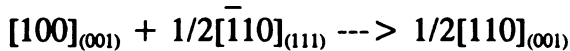
(Figure 2.12 continued)

dislocations, a reconstruction of the whole configuration takes place which results in a dipole forming on the superdislocations. The dipole contains two SISF bands on the parallel primary slip planes and one SISF band on the second plane, Fig. 2.12 (c). The tube formation ends by the formation of APB bands which takes place during emission of $1/2 < 101 \rangle$ screw dislocations (vector CB in Fig. 2.12 (d)) in parallel cross-slip planes. In practice, depending on the jog height, the tube may be observed either as two isolated SISF's or as a SESF (if the jog is not large).

(e) Dislocation Interaction Blocking

When two mobile dislocations are moving toward each other, these two dislocations can react at their intersection and produce a third dislocation. This resultant dislocation is either glissile on one of primary slip planes that the two unreacted dislocations belong to, or glissile on the third slip plane, or completely sessile, i.e., to form a stair rod dislocation. Either of the last two resultant dislocations can not move in the primary slip planes of two reacting dislocations, and hence, blocks the two glissile dislocations. Kawabata and Izumi ^[55] made a good summary on some possible dislocation reactions in TiAl. In addition to the dislocation reactions of Kawabata and Izumi's, some additional dislocation reactions in terms of $< 100 >$ type dislocations are summarized by the author. The added dislocation reactions are listed in the following.

Reactions between $< 100 >$ and $1/2 < 110 \rangle$ dislocations



$$[001]_{(100)} + 1/2[\bar{1}10]_{(1\bar{1}\bar{1})} \rightarrow \underline{1/2[\bar{1}12]}_{(1\bar{1}\bar{1})} \#$$

$$[001]_{(100)} + 1/2[110]_{(1\bar{1}\bar{1})} \rightarrow \underline{1/2[112]}_{(1\bar{1}\bar{1})} \#$$

Reactions between $\langle 100 \rangle$ and $\langle 011 \rangle$ dislocations

$$[100]_{(001)} + [\bar{1}01]_{(111)} \rightarrow \underline{1/2[101]}_{(1\bar{1}\bar{1})} + \text{APB} + 1/2[\bar{1}01]_{(111)}$$

$$[100]_{(001)} + [011]_{(11\bar{1})} \rightarrow \underline{1/2[211]}_{(1\bar{1}\bar{3})} + \text{APB} + 1/2[011]_{(11\bar{1})} \#$$

$$[001]_{(100)} + [10\bar{1}]_{(111)} \rightarrow \underline{1/2[101]}_{(\bar{1}11)} + \text{APB} + 1/2[10\bar{1}]_{(111)}$$

$$[001]_{(100)} + [01\bar{1}]_{(111)} \rightarrow 1/2[011]_{(100)} + \text{APB} + 1/2[01\bar{1}]_{(111)}$$

Reactions between $\langle 100 \rangle$ and $1/2\langle 112 \rangle$, $1/3\langle 112 \rangle$, $1/6\langle 112 \rangle$ dislocations

$$[100]_{(001)} + 1/2[\bar{1}12]_{(1\bar{1}\bar{1})} \rightarrow \underline{1/2[112]}_{(\bar{1}10)}$$

$$[100]_{(001)} + 1/3[\bar{1}12]_{(1\bar{1}\bar{1})} \rightarrow \underline{1/3[212]}_{(\bar{2}21)}$$

$$[100]_{(001)} + 1/6[\bar{1}12]_{(1\bar{1}\bar{1})} \rightarrow \underline{1/6[512]}_{(\bar{1}12)}$$

$$[001]_{(100)} + 1/2[11\bar{2}]_{(111)} \rightarrow \underline{1/2[110]}_{(\bar{1}12)}$$

$$[001]_{(100)} + 1/3[11\bar{2}]_{(111)} \rightarrow \underline{1/3[111]}_{(\bar{2}11)}$$

$$[001]_{(100)} + 1/6[11\bar{2}]_{(111)} \rightarrow \underline{1/6[114]}_{(5\bar{1}\bar{1})}$$

Reactions between $\langle 100 \rangle$ dislocations

$$[100]_{(001)} + [010]_{(100)} \rightarrow [110]_{(001)} \#$$

$$[100]_{(001)} + [001]_{(100)} \rightarrow \underline{[101]}_{(\bar{1}01)} \#$$

$$[100]_{(001)} + [001]_{(010)} \rightarrow [101]_{(010)} \#$$

Here the underlines indicate resultant stair rod dislocations and the marks "#" at the end

of equations indicate that the reactions are energetically equivalent in the forward and backward directions.

2.1.5. Lamellar Structure and Its Formation

The lamellar structure in TiAl is formed by a phase transformation and it can be classified into two types, type-I and type-II, according to γ lath crystal orientation relationships within lamellae. Both types of lamellar structures have alternating $\alpha_2(\text{Ti}_3\text{Al})/\gamma(\text{TiAl})$ plates at room temperature and the same crystallographic orientation relationships between α_2 and γ . The difference between these two types of lamellar structures is that γ plates in type-II have the same crystal orientations within a grain, but γ plate crystal orientations in type-I vary from plate to plate.

(a) Type-I Lamellar Structure

The type-I lamellar structure is typically formed by the growth of γ plates into α phase or α_2 phase in two phase regions: $\alpha + \gamma$ and $\alpha_2 + \gamma$ (see phase diagram shown in Fig. 2.2). The TiAl (γ) lamellar phase is formed on the basal plane of the Ti_3Al (α_2) at the expense of the Ti_3Al phase and finally a lamellar structure consisting of lamellae of TiAl and Ti_3Al phases is formed in the two phase region ^[62]. The orientation relationship between the TiAl and Ti_3Al is the following ^[63],

$$\begin{aligned} \{111\}_{\text{TiAl}} // (0001)_{\text{Ti}_3\text{Al}} \\ \langle 110 \rangle_{\text{TiAl}} // \langle \bar{1}1\bar{2}0 \rangle_{\text{Ti}_3\text{Al}} \end{aligned}$$

The $\langle 110 \rangle$ and $\langle 101 \rangle$ in TiAl are not equivalent to each other, but the $\langle 11\bar{2}0 \rangle$ directions in Ti_3Al are all equivalent. Therefore, there exist six possible crystal orientations, as shown in Fig. 2.13 [64]. In Fig. 2.13, orientations E and F are crystallographically identical to the orientations C and D, respectively. Therefore, four distinguishable orientations exist in TiAl laths. With different combinations of two of them, there exist four orientation relationships between two γ plates: (1) when orientation A in one γ plate is parallel to orientation A in neighboring γ plate, a translation order-fault interface or no interface is formed between them; (2) when A//C or A//E, a 120° rotational order-fault interface is formed where the c-axes of the two neighboring γ plates are perpendicular to each other; (3) when A//B, two γ plates have true-twin relationship; (4) when A//D or A//F, pseudo-twin relationship is formed. The pseudo-twin differs from the true-twin. In the pseudo-twin, the atomic sites are in twin positions but these sites are incorrectly occupied by anti-site atoms. Since the energy of lamellar interface with true-twin orientation relationship is lower than those with other orientation relations, the true-twin lamellar interface is more preferred. When the orientation relationships other than the true-twin are observed, a thin lamella of Ti_3Al is often found to be sandwiched between the corresponding two TiAl lamellae. However, for mechanical twinning, the energetic criterion is usually not suitable, particularly at high stress and low temperature deformation. In this case a maximum resolved shear stress criterion proposed by Jin is more suitable [28].

(b) Type-II Lamellar Structure

The type-II lamellar structure is formed by Ti_3Al (α_2) plate growing into TiAl (γ)

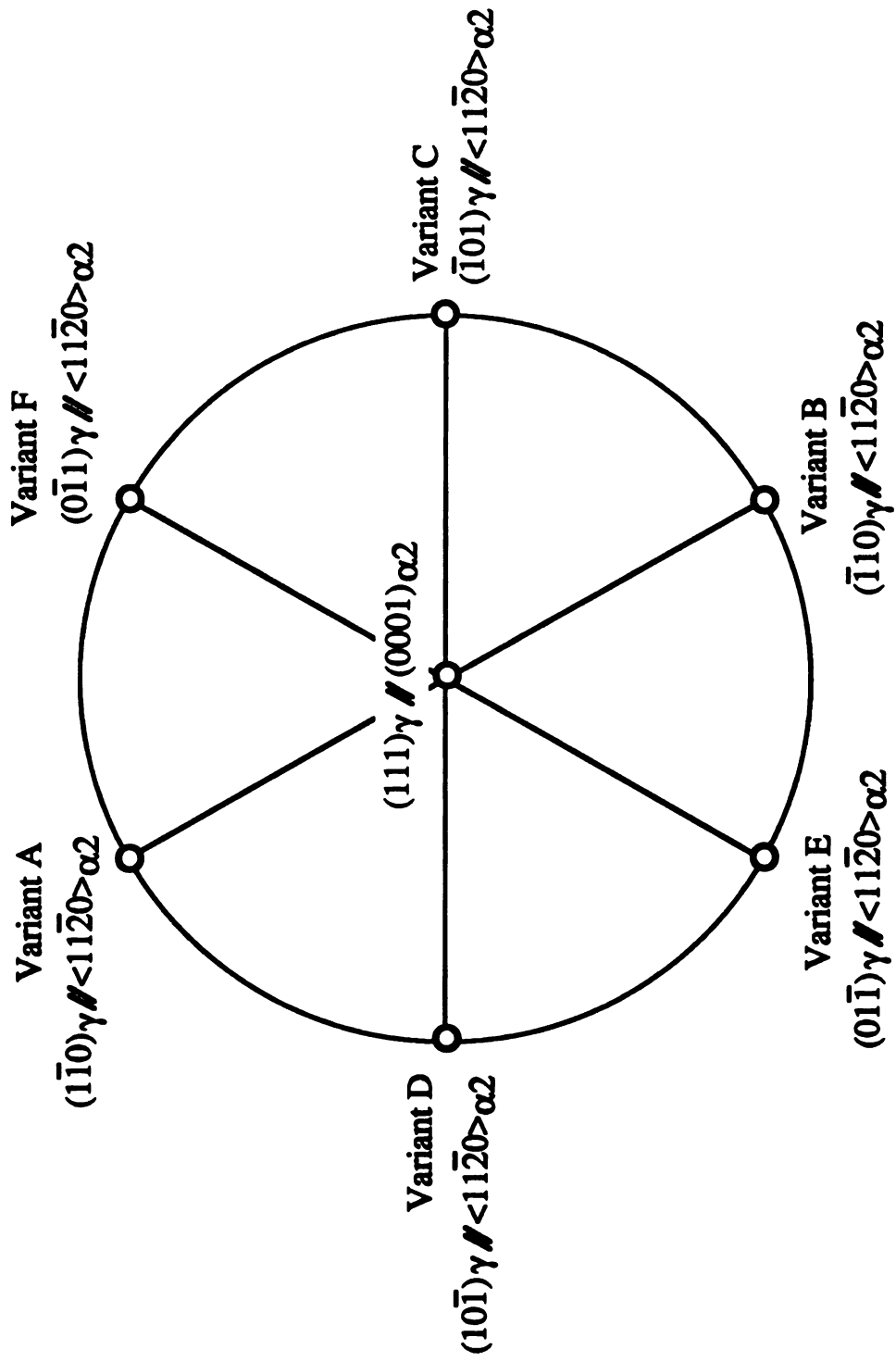


Figure 2.13 - Definition of orientation variants in $(\gamma + \alpha_2)$ lamellae.

phase. This lamellar structure has the orientation relationship between the TiAl and Ti₃Al as type-I does, that is, $\{111\}_{\text{TiAl}} // (0001)_{\text{Ti}_3\text{Al}}$ and $\langle 110 \rangle_{\text{TiAl}} // \langle 11\bar{2}0 \rangle_{\text{Ti}_3\text{Al}}$. However, since all $\langle 11\bar{2}0 \rangle$ directions in Ti₃Al are equivalent to one another, there are only one α_2 crystal orientation and only one γ crystal orientation within a grain, and the γ crystal orientation is the orientation of the original γ grain.

There are two ways to form either type-I or type-II lamellar structure, as shown in the following.

For type-I, (i) $\alpha \rightarrow \alpha + \gamma_p \rightarrow L(\alpha/\gamma) \rightarrow L(\alpha_2/\gamma)$
(ii) $\alpha \rightarrow \alpha_2 \rightarrow \alpha_2 + \gamma_{pt} \rightarrow \alpha_2 + \gamma_p \rightarrow L(\alpha_2/\gamma)$

where γ_p stands for γ plates, $L(\alpha/\gamma)$ stands for lamellar structure of γ phase and α phase, γ_{pt} is γ precipitates.

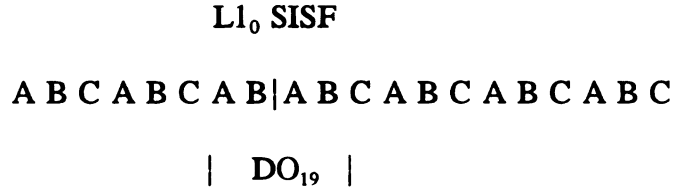
For type-II, (i) $\gamma_m + \alpha^p \rightarrow \gamma_m + \alpha_p \rightarrow L(\gamma/\alpha) \rightarrow L(\gamma/\alpha_2)$
(ii) $\gamma_m \rightarrow \gamma_m + \alpha_{pt} \rightarrow \gamma_m + \alpha_{pl} \rightarrow L(\gamma/\alpha) \rightarrow L(\gamma/\alpha_2)$

where superscript "p" dedicates particles, subscript "pl" dedicates plates, subscript "m" matrix and subscript "pt" precipitates.

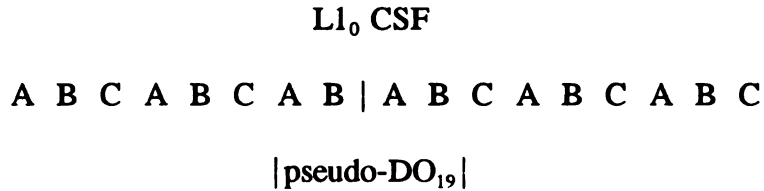
2.1.6. Phase Transformation Mechanisms

Concerning phase transformation mechanisms, there is a well-accepted stacking

fault mechanism proposed by Blackburn ^[65]. A TiAl ($L1_0$) stacking fault has the equivalent stacking sequence to the Ti_3Al structure (DO_{19}). For example, in a SISF (Superlattice Intrinsic Stacking Fault), the four atomic layers around $L1_0$ stacking fault turns out to be DO_{19} crystal structure,



However, this mechanism is not suitable for other stacking faults existing in TiAl. In the case of CSF (Complex Stacking Fault), even though the stacking sequence of four atomic layers in CSF is similar to DO_{19} structure,



it is a pseudo- DO_{19} structure since it includes an anti-phase component, as shown in Fig. 2.3 (c). For the SESF (Superlattice Extrinsic Stacking Fault) and the APB (Antiphase Boundary), the Blackburn mechanism is also not suitable, (see Fig. 2.3 (a), (d) and (e)). But, since the SISF is the lowest interface energy condition of all possible stacking faults, and therefore very common in TiAl, it can help explaining how the α_2 precipitates in the γ matrix. Once a Ti_3Al phase nucleates at the SISF of TiAl, Ti_3Al grows along the

octahedral plane of TiAl by increasing the separation of the bounding Shockley partial dislocations in the octahedral plane.

The γ precipitation in α_2 basal plane can also be explained by this mechanism in the same way. In this case, glide of Shockley partials $a/3 < 10\bar{1}0$] in alternate basal planes of Ti_3Al matrix results in $L1_0$ atomic stacking sequence (TiAl),

A B A B A B A B C A B C A B C A B A B A B

DO₁₉ | L1₀ | DO₁₉

or

A B A B A B A C B A C B A C B A B A B A B

DO₁₉ | L1₀ | DO₁₉

by operating opposite Shockley partials $a/3 < \bar{1}010$] ^[65,66].

2.2. Mechanical Twinning Theory

2.2.1. Definition

Mechanical twinning is generally defined as a homogeneous shape deformation in which the deformed crystal structure is identical with that of the parent, but oriented differently. If the product and parent are to remain in contact, the deformation must be an invariant-plane strain. Since the two structures are identical, there can be no volume change and the deformation must be a simple shear. In general, the twinning modes are

defined with four twinning elements: K_1 , K_2 , η_1 and η_2 ^[67]. K_1 is the first invariant or unrotated plane in the twinning operation; η_1 is the direction of shear that is in the K_1 plane. K_1 is called twinning plane and η_1 is called twinning direction. K_2 is the second undistorted (but rotated) plane and called conjugate twinning plane. The plane perpendicular to K_1 and K_2 and containing η_1 is called the plane of shear and denoted by S . η_2 is the intersection between K_2 and S , and it is called conjugate twinning direction. To any given twin mode, $K_1=(hkl)$, $K_2=(h'k'l')$, $\eta_1=[uvw]$ and $\eta_2=[u'v'w']$, there corresponds theoretically a conjugate or reciprocal mode $K_1'=K_2=(h'k'l')$, $K_2'=K_1=(hkl)$, $\eta_1'=\eta_2=[u'v'w']$ and $\eta_2'=\eta_1=[uvw]$, with the same magnitude of shear g .

When specifying a mechanical twinning mode, we also indicate the twinning shear magnitude (g) and the shuffle parameters q and \bar{q} in addition to the twinning elements. Here q is the number of K_1 lattice planes crossed by a primitive lattice vector parallel to η_2 , and \bar{q} is the number of K_2 lattice planes crossed by a primitive lattice vector parallel to η_1 .

When describing the twinning crystallography, we also need to define the sign of each twinning element. According to the Bilby-Crocker sign convention ^[68], the signs of twinning elements are defined as the following. The relative signs are chosen such that on twinning, the positive side of the K_1 plane shears in the positive η_1 direction and similarly for the conjugate shear. The angle between the positive directions of η_1 and η_2 is obtuse in the parent crystal, the angles between η_1 and the normal to K_2 plane and

between η_2 and the normal to K_1 plane are both acute, and the directions of η_1 , η_2 and the positive normal to S form a right handed set.

2.2.2. Seven Twinning Classes

Based on the above general twinning definition, mechanical twinning can be classified into seven classes, as shown in table 2.2 ^[69]. Table 2.2 was obtained by using the unimodular correspondence matrices given in table 2 of [70]. In table 2.2, m is the reciprocal of the fraction of lattice points sheared directly to correct twin positions in a primitive lattice, the remaining lattice points having to shuffle in order to get to the correct twin positions, and n is the position number of the correspondence matrix in table 2 of [70]. Therefore, $m.n$ indicates the twinning mode. The \bar{m} and \bar{n} in table 2.2 indicate that the correspondence matrix is the inverse of the preceding one. m_I and m_F are the m values for bcc and fcc crystal structures respectively. The twinning shear magnitude, g , is presented in m^2g^2 form in order to get integers. The a and b in the "class" column indicate two different relations between the twinning elements and the asterisks indicate the indistinguishable subdivisions of the correspondence matrix. Therefore, when the twinning modes with $m = 1$, $m_I = 1$ and $m_F = 1$ are operating, no lattice point shuffles are needed for the simple cubic lattice, for the bcc lattice and for the fcc lattice, respectively. For modes with m , m_I or $m_F = 2$, one half of the lattice points must shuffle in the corresponding lattice. Similarly, for m , m_I or $m_F = 4$, three quarters must shuffle.

Table 2.2. Twinning modes in cubic lattices

class	M.n	K_1	K_2	η_1	η_2	S	m^2g^2	m_I	m_F
1	2.7	$1 e^+ 1$	$1 e^- 1$	$2 e^- 2$	$\bar{2} e^+ e^-$	$1 0 \bar{1}$	6	2	4
1	$\bar{2}.7$	$1 1 f^+$	$\bar{1} \bar{1} f^-$	$\bar{4} \bar{4} f^-$	$4 4 f^+$	$1 \bar{1} 0$	6	2	4
1	4.14	$1 1 \bar{1}$	$1 1 \bar{1} 1$	$2 \bar{1} 1$	$2 1 1 \bar{1} \bar{1}$	$0 1 1$	18	8	2
1	$\bar{4}.14$	$1 1 \bar{1}$	$\bar{5} 7 7$	$\bar{2} 1 \bar{1}$	$14 5 \bar{5}$	$0 1 1$	18	8	2
2	1.3	$1 0 0$	$1 1 1$	$0 1 1$	$2 \bar{1} \bar{1}$	$0 1 \bar{1}$	2	2	1
2	1.6	$1 0 0$	$5 2 4$	$20 1 2$	$2 \bar{1} \bar{2}$	$0 2 \bar{1}$	5	2	2
2	2.2	$1 1 1$	$\bar{1} 1 1$	$\bar{2} 1 1$	$2 1 1$	$0 1 \bar{1}$	2	4	1
2	2.3	$1 0 0$	$1 \bar{2} \bar{2}$	$0 \bar{1} \bar{1}$	$4 1 1$	$0 1 \bar{1}$	2	4	2
2	2.6	$1 0 0$	$5 \bar{4} 8$	$0 1 \bar{2}$	$4 1 2$	$0 2 \bar{1}$	5	4	4
2	2.8	$1 1 0$	$\bar{1} 7 \bar{4}$	$\bar{1} 1 \bar{1}$	$3 1 1$	$\bar{1} 1 2$	6	1	4
3	4.23	$2 j^+ \bar{1}$	$\bar{2} j^- 1$	$8 j^- 4$	$8 j^+ \bar{4}$	$1 0 2$	34	8	4
4a	2.4	$0 1 c^+$	$0 1 c^-$	$0 c^+ \bar{1}$	$0 c^- 1$	$1 0 0$	2	4	4
4	$\bar{2}.4$	$0 1 d$	$0 \bar{1} d$	$0 d 1$	$0 d 1$	$1 0 0$	2	4	4
4a	$\underline{2.12}$	$0 g^+ \bar{1}$	$0 g^- 1$	$0 1 g^+$	$0 1 g^-$	$1 0 0$	10	4	4
4a	2.12	$0 3 h^+$	$0 3 h^-$	$0 h^+ 3$	$0 h^- 3$	$1 0 0$	10	4	4
5b	4.4	$2 i^- 2$	$2 i^+ 2$	$1 i^+ 1$	$1 i^- 1$	$1 0 \bar{1}$	4	4	4
5	4.28	$k^- 2 k^+$	$k^+ \bar{2} k^-$	$l^+ \bar{4} l^-$	$l^- 4 l^+$	$1 \bar{1} 1$	36	4	4

Table 2.2. Twinning modes in cubic lattices (continued)

class	M.n	K_1	K_2	η_1	η_2	S	m^2g^2	m_i	m_F
6a	1.4	$a^+ 1 1$	$a^- 1 1$	$a^- 1 1$	$a^+ \bar{1} \bar{1}$	$0 1 \bar{1}$	4	2	2
6a	1.7	$0 b^+ 1$	$0 b^- 1$	$0 \bar{1} b^+$	$0 1 b^-$	$1 0 0$	5	2	2
7a	1.2	$1 0 0$	$1 \bar{2} 0$	$0 \bar{1} 0$	$2 1 0$	$0 0 1$	1	2	2
7a	1.5	$1 0 0$	$1 \bar{1} 0$	$0 \bar{1} 0$	$1 1 0$	$0 0 1$	4	1	1
7a	2.1	$1 0 0$	$1 \bar{4} 0$	$0 \bar{1} 0$	$4 1 0$	$0 0 1$	1	4	4
7a	2.5	$1 1 0$	$\bar{1} 3 0$	$\bar{1} 1 0$	$3 1 0$	$0 0 1$	4	2	2
7	2.9	$1 2 0$	$\bar{1} 2 0$	$\bar{2} 1 0$	$2 1 0$	$0 0 1$	9	4	4
7a	2.10	$1 0 0$	$3 \bar{4} 0$	$0 \bar{1} 0$	$4 3 0$	$0 0 1$	9	4	4
7b	2.11	$2 1 0$	$2 5 \bar{4}$	$\bar{2} 4 \bar{5}$	$2 0 1$	$\bar{1} 2 2$	9	4	4

$$\begin{array}{llll}
 a^\pm = 2 \pm 2^{1/2}; & b^\pm = 3 \pm 5^{1/2}; & c^\pm = 3 \pm 8^{1/2}; & d = 2^{1/2}; \\
 e^\pm = 4 \pm 12^{1/2}; & f^\pm = 12^{1/2} \pm 2; & g^\pm = 10^{1/2} \pm 2; & h^\pm = 40^{1/2} \pm 1; \\
 i^\pm = 8^{1/2} \pm 2; & j^\pm = 24^{1/2} \pm 2; & k^\pm = 12^{1/2} \pm 1; & l^\pm = 2 \pm 3^{1/2}.
 \end{array}$$

2.2.3. Classic Twinning Modes

Based on the classic twinning theory, the orientation relationships between the parent and the twin are classified into four groups formed by ^[67]:

- (i) reflection in K_1 plane;
- (ii) rotation of 180° about η_1 ;
- (iii) reflection in the plane normal to η_1 ;
- (iv) rotation of 180° about the normal to K_1 .

In these four orientation relations, at least two twinning elements must be rational. It will be proved that modes (i) and (iv) or modes (ii) and (iii) are geometrically equivalent to one another in the following section.

Since the twinning elements indexed by letters a^\pm to l^\pm in Table 2.2 are all irrational, classes 3, 4, 5, 6 and some modes in class 1 are not classic twinning modes.

2.2.4. Crystallography of Mechanical Twinning

The earliest theory of mechanical twinning crystallography may be referred to work done by Schmid and Boas in 1950 ^[71]. A few years later, the review papers by Hall ^[72] and Cahn ^[67], the work done by Kiho ^[73,74], Jaswon and Dove ^[75-77] described several theories of mechanical twinning crystallography in their special cases. Several years later in 1960's, Billy and Crocker ^[68], Bevis and Crocker ^[69,70] proposed a more general and comprehensive theory. In this section, the crystallography of mechanical twinning will be summarized. The twinning mode considered will be the classic twinning mode.

Following the notation of tensor calculus, we define \mathbf{c}_i and \mathbf{p}_i ($i=1,2,3$) are direct primitive lattice bases to define the parent and the twin lattices, respectively, and therefore the corresponding reciprocal lattice bases are defined by \mathbf{c}^i and \mathbf{p}^i . The direct primitive lattice bases \mathbf{c}_i and \mathbf{p}_i have the relations as shown in Fig. 2.14 corresponding to the four orientation relationships of classic twinning modes. The \mathbf{p}_i is a reflection of \mathbf{c}_i about K_1 plane in Fig. 2.14 (a); the \mathbf{p}_i in Fig. 2.14 (b) is obtained by 180° rotation of

\mathbf{c}_i about η_1 ; in Fig. 2.14 (c) the \mathbf{p}_i is the reflection of \mathbf{c}_i in the plane normal to η_1 ; and in Fig. 2.14 (d) the \mathbf{p}_i is the 180° rotation of \mathbf{c}_i about the normal to K_1 .

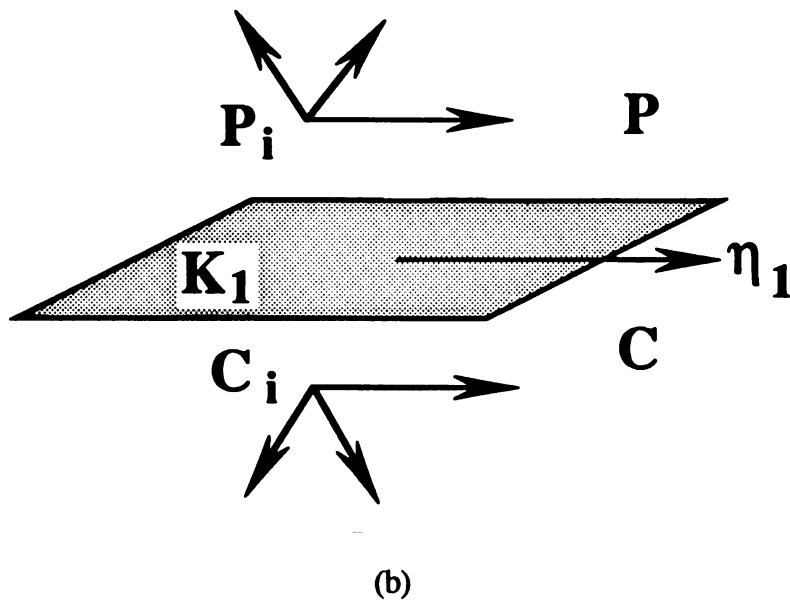
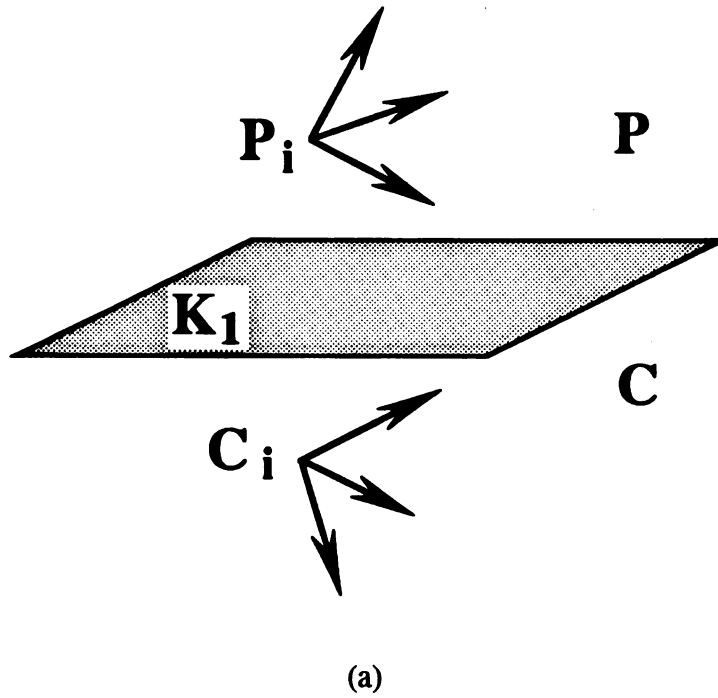
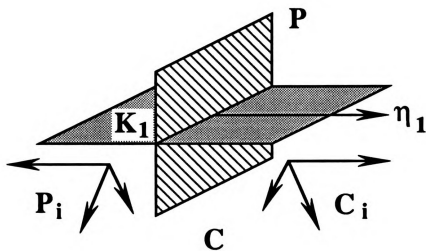
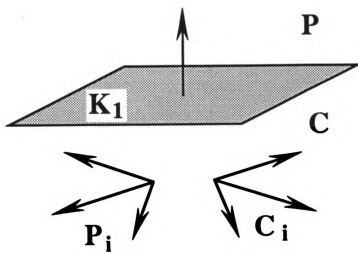


Figure 2.14 - Relations between \mathbf{c}_i and \mathbf{p}_i .



(c)



(d)

(Figure 2.14 continued)

In the notation of tensor calculus, we have the interplanar spacing of h_i planes, $d = (c^i h_i h_i)^{-1/2}$, the identity distance along the u^i direction, $a = (c_{ij} u^i u^j)^{1/2}$, the unit vector normal to K_1 plane, $n^i c_i = d c^i h_i c_i = d h_i c^i$, and the unit vector along η_1 direction, $b_i c^i = a^{-1} c_{ij} u^j c^i = d^{-1} u^i c_i$. The sign of these notations are shown in Fig. 2.15. According to Fig. 2.15, the twinning plane can be defined by K_1 , h_i or n^i ; the twinning direction is η_1 , u^i or b_i ; the reciprocal twinning plane K_2 , k_i or \underline{n}^i ; the reciprocal twinning direction η_2 or v^i ; the normal to the plane of shear S is s^i .

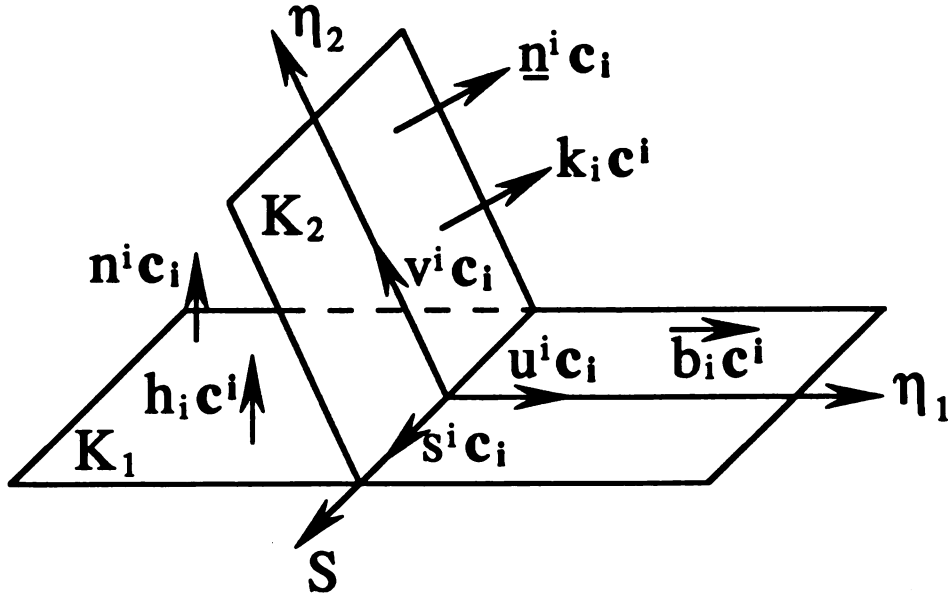


Figure 2.15 - The sign of four twinning elements.

Thus, the four orientation relationships of classic twinning modes can be expressed in tensor notations as follows,

$$p_i^{(1)} = c_i - 2dh_i n^i c_j, \quad (2.1)$$

$$\mathbf{p}_i^{(2)} = 2a^{-1}b_i u^i \mathbf{c}_j - \mathbf{c}_i, \quad (2.2)$$

$$\mathbf{p}_i^{(3)} = \mathbf{c}_i - 2a^{-1}b_i u^i \mathbf{c}_j, \quad (2.3)$$

$$\mathbf{p}_i^{(4)} = 2adh_i v^i \mathbf{c}_j - \mathbf{c}_i. \quad (2.4)$$

Here the superscripts ($s=1,2,3,4$) of \mathbf{p}_i in equations (2.1) to (2.4) indicate the four corresponding twin relations. Investigating these four equations, we find that $\mathbf{p}_i^{(1)} = -\mathbf{p}_i^{(4)}$ and $\mathbf{p}_i^{(2)} = -\mathbf{p}_i^{(3)}$. So actually only two twin orientation relationships exist. Thus the relations (i) and (iv) in the classic twinning modes shown in section 2.2.3 are classified as type-I, and the relations (ii) and (iii) are classified as type-II.

Now let us look at the properties of type-I twinning. Fig. 2.16 shows the geometry of twinning shear in K_1 plane. When the composition plane moves from a

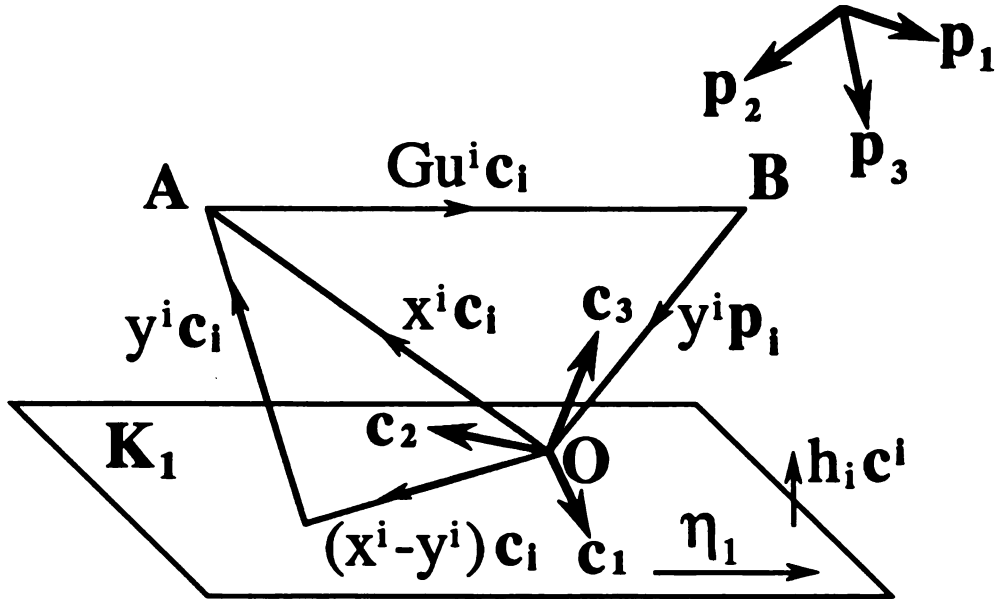


Figure 2.16 - The rationality of K_1 in type-I twinning.

position containing the lattice point A at $x^i \mathbf{c}_i$ to a position containing the origin O of the parent lattice base \mathbf{c}_i and the lattice point B at $-y^i \mathbf{p}_i$, the shear of amount $G u^i \mathbf{c}_i$ is required such that

$$x^i \mathbf{c}_i + G u^i \mathbf{c}_i = -y^i \mathbf{p}_i \quad (2.5)$$

Here $G = g a^{-1} d x^i h_i$, and g is the twinning shear. The projection of $x^i \mathbf{c}_i$ and $y^i \mathbf{p}_i$ on the normal to the twinning plane are clearly equal, so the vector $(x^i - y^i) \mathbf{c}_i$ in Fig. 2.16 must lie in the composition plane. Since the x^i and y^i are the lattice points, they should be integers, so $(x^i - y^i) \mathbf{c}_i$ is a rational vector. This vector can be one of an infinite number of directions in the K_1 plane depending on the selection of $x^i \mathbf{c}_i$, so K_1 must be rational.

Since $\mathbf{p}_i = \mathbf{c}_i - 2d h_i n^i \mathbf{c}_j$ for type-I twinning, the equation (2.5) becomes

$$G u^i \mathbf{c}_i = -(x^i + y^i) \mathbf{c}_i + 2d y^i h_i n^i \mathbf{c}_j \quad (2.6)$$

Assume $x^i + y^i = z^i$, then we have

$$x^i h_i + y^i h_i = 2x^i h_i = 2y^i h_i = z^i h_i \quad (2.7)$$

so we obtain

$$g a^{-1} d z^i h_i u^i \mathbf{c}_i = -z^i \mathbf{c}_i + 2d z^i h_i n^i \mathbf{c}_j \quad (2.8)$$

By using the orientation relationship of type-I, i.e., $\mathbf{p}_i = \mathbf{c}_i - 2d h_i n^i \mathbf{c}_j$, equation (2.8) becomes

$$z^i c_i + g a^{-1} d z^j h_j u^i c_i = -z^i p_i \quad (2.9)$$

or

$$z^i c_i + G u^i c_i = -z^i p_i \quad (2.10)$$

The equation (2.10) is identical to the equation (2.5). Thus, this equation indicates that the parent lattice vector $z^i c_i$ is sheared to become the twin lattice vector $-z^i p_i$ with the same indices. The vector $z^i c_i$ is thus undistorted and must lie in K_2 plane.

Since $s^i c_i$ is normal to the plane of shear, as shown in Fig. 2.15, we have by definition $s^i h_i = c_{ij} n^i s^j = c_{ij} u^i s^j = 0$. Taking the scalar product of each term in equation (2.8) with $s^i c_i$, we obtain $c_{ij} z^j s^i = 0$. So $z^i c_i$ lies in the plane of shear and the rational lattice vector $z^i c_i$ lies along the reciprocal twinning direction η_2 . The same result holds for the twin relationship (iv). Thus for type-I twinning, both K_1 plane and η_2 direction are rational. In the case that all four elements are rational, the twinning mode is compound.

In a similar way, it can be proved that the K_2 plane and the η_1 direction are rational for type-II twinning mode, the details of which are in reference [68]. If the K_1 plane and the η_2 direction are also rational in the case of type-II, the twinning mode becomes compound.

Therefore, the mechanical twinning modes can be classified as the following three types:

Type-I: K_1 plane and η_2 direction are rational;

Type-II: K_2 plane and η_1 direction are rational;

Compound: all twinning elements K_1 , K_2 , η_1 and η_2 are rational.

2.2.5. Atomic Movement in Twinning Shear

In this section, we also use type-I twinning mode as an example to analyze the atomic movement in twinning shear. We assume that $v^i c_i$ is the shortest lattice vector in the direction of $z^i c_i$, i.e., in the η_2 direction, then $z^i = mv^i$, where m is an integer. If D is any lattice point of the parent in the plane through the lattice point $v^i c_i$ and parallel to h_i plane, as shown in Fig. 2.17, OD may be written $(v^i + f^i) c_i$, where $f^i h_i = 0$. After the twinning shear, OD becomes the vector

$$(v^i + f^i) c_i + g a^{-1} d v^k h_k u^i c_i = -v^i p_i + f^i c_i \quad (2.11)$$

Based on equation (2.1), we have

$$(v^i + f^i) p_i = (v^i + f^i) c_i + 2 d v^j h_j n^i c_i \quad (2.12)$$

that is,

$$f^i p_i = f^i c_i \quad (2.13)$$

So (2.11) becomes

$$(v^i + f^i) c_i + G u^i c_i = -v^i p_i + f^i p_i = (f^i - v^i) p_i \quad (2.14)$$

Thus every point in this plane is also sheared to a twin lattice point.

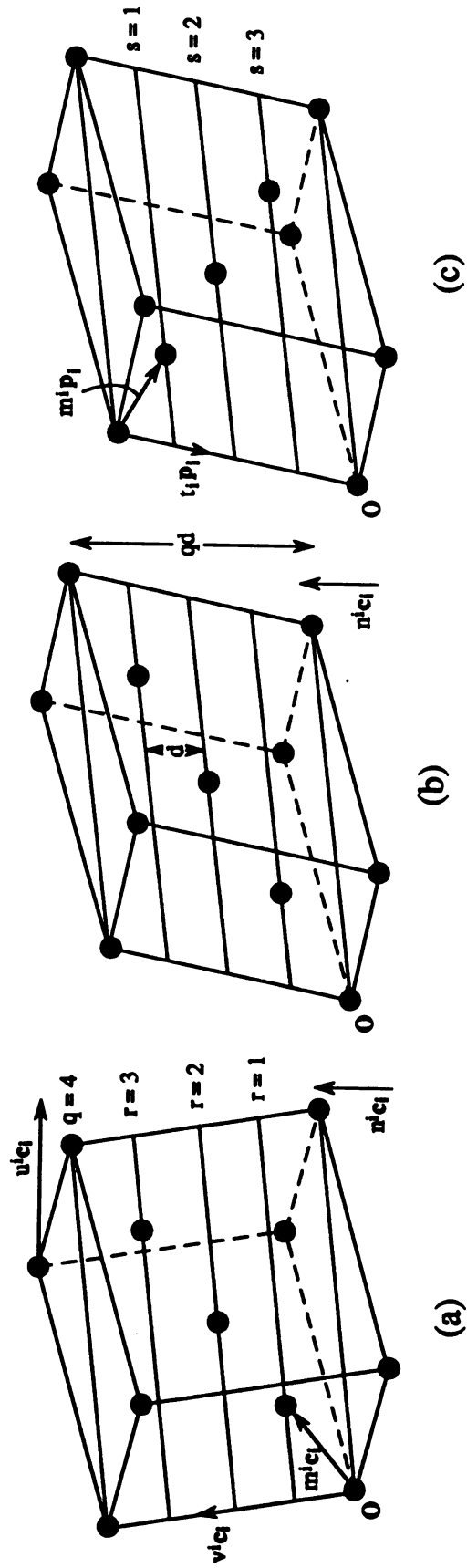


Figure 2.17 - Schematic illustration of lattice shuffling during type-I twinning for the case of $q = 4$.

However, if the points on those h_i planes lying between O and v^i , these points in general will not shear directly to twin lattice points. In order to get to the correct twin lattice points, these points must shuffle. If we assume that all lattice points on a given h_i plane shuffle in the same way, we need to consider only one lattice point on each plane.

Let $v^i h_i = q$, then $a_{ij} v^j n^i = qd$, where d is the interplanar spacing of plane h_i and q is the number of h_i planes cutting $v^i c_i$. If $m^i c_i$ is a lattice vector connecting the origin of primitive parent lattice base c_i to any point on the h_i plane that has a distance d from the origin O, as shown in Fig. 2.17 (a) where $q = 4$, $m^i h_i$ will be equal to one and any parent lattice point can be represented by $rm^i c_i$, where r is a positive integer and smaller than q . During the twinning shear, the lattice points $rm^i c_i$ will move to positions $r(m^i + g a^{-1} d u^i) c_i = r(m^i + 2d n^i - 2q^{-1}) c_i$, as shown in Fig. 2.17 (b). From Fig. 2.17 (b), we see that not all $r(m^i + 2d n^i - 2q^{-1}) c_i$ positions are at the correct twin lattice points. The correct twin lattice points relative to O in Fig. 2.17 are given by the lattice vectors $(s m^i - t^i) p_i$, where $-t^i p_i$ is a lattice vector connecting O to any twin lattice point on the h_i plane and s is a positive integer less than q in the p lattice base. Therefore, the difference

$$\begin{aligned} \Delta &= (s m^i - t^i) p_i - r(m^i + 2d n^i - 2q^{-1}) c_i \\ &= [(s - r)m^i + 2d(q - r - s)n^i + (2rq^{-1}v^i - t^i)] c_i \end{aligned} \quad (2.15)$$

defines the shuffles necessary to take the sheared lattice points to the correct twin lattice

points. By taking the scalar product of Δ with $h_i c^i$, we can see that the component of Δ normal to h_i is zero when $s = q - r$. Substituting $s = q - r$ for s in above equation, we obtain the shuffles in the h_i planes

$$\Delta = [(q - 2r)m^i - t^i + 2rq^{-1}v^i]c_i \quad (2.16)$$

Therefore, the necessary condition for $\Delta = 0$ is that

$$r = 1/2 q \quad (2.17)$$

if we choose $t^i = v^i$ and $s = r$. When q is even the lattice points on the h_i plane defined by $r = 1/2 q$ need not shuffle. So if $q = 2$, no shuffles are needed for any parent lattice point to move to the correct twin lattice point. But for $q > 2$, at least some lattice points must shuffle as illustrated in Fig. 2.17.

For the multiple lattice structure, the shuffling is much more complicated than the single lattice structure analyzed above. In the case of multiple lattice structure, the shuffles both in the h_i planes and in the directions perpendicular to h_i planes are necessary to move parent lattice points to the twin lattice positions.

2.2.6. Strain in Twinning

On the macroscopic scale, the twinning deformation consists of homogeneous simple shear displacement parallel to the plane K_1 and in the direction η_1 . The magnitude of shear can be obtained by the following equation

$$s = 2 \cot \angle \eta_1 \eta_2 = 2 \tan \angle \eta_1 K_2 = 2 \tan \angle \eta_2 K_1 \quad (2.18)$$

where $\angle \eta_1 \eta_2$ is the acute angle between the two directions concerned, $\angle \eta_1 K_2$ is the acute angle between η_1 and the normal to the plane K_2 , and $\angle \eta_2 K_1$ is the acute angle between the η_2 and the normal to K_1 .

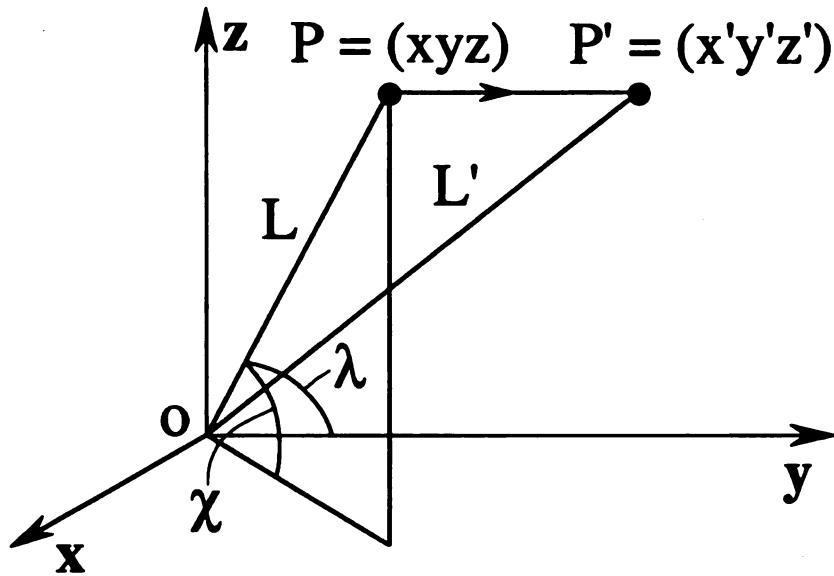


Figure 2.18 - Lattice point displacement during twinning shear.

Let us look how the specimen length changes corresponding to the twinning. We choose the orthogonormal cartesian coordinate system such that the axes x and y in twinning plane and y axis is in twinning direction, as shown in Fig. 2.18 [72]. The points $P(x, y, z)$ and $P'(x, y + sz, z)$ are lattice point coordinates before and after twinning, here s is the magnitude of shear. Thus, the ratio of the lengths of the position vectors of P' and

P is as follows

$$\frac{L'}{L} = \left(\frac{x^2 + y^2 + 2syZ + (s^2 + 1)z^2}{x^2 + y^2 + z^2} \right)^{\frac{1}{2}} = (1 + 2s \sin \chi \cos \lambda + s^2 \sin^2 \chi)^{\frac{1}{2}} \quad (2.19)$$

where $y = L \cos \lambda$, $z = L \sin \chi$. Since the maximum strain (extension or contraction in length) is obtained in the plane of shear, i.e., when $x = 0$ or $\lambda = \chi$, the maximum and minimum values of the extension or contraction can be obtained by differentiation of equation (2.19) and the result is expressed as

$$\left(\frac{L'}{L} \right)_{\max} = \sqrt{1 + s^2 \tan^2 \chi} \quad (2.20)$$

The maximal extension $(L'/L)_{\max}^e$ and the maximal contraction $(L'/L)_{\max}^c$ in terms of the magnitude of twinning shear (s) are expressed as follows

$$\left(\frac{L'}{L} \right)_{\max}^e = \frac{s}{2} + \sqrt{\frac{s^2}{4} + 1} \quad (2.21)$$

$$\left(\frac{L'}{L} \right)_{\max}^c = -\frac{s}{2} + \sqrt{\frac{s^2}{4} + 1} \quad (2.22)$$

The extension and contraction of sample lengths are, therefore, conveniently represented on the stereographic projection, as shown in Fig. 2.19 ^[72] which is for twinning in a zinc crystal. Poles I to VI indicate the six twinning planes $\{10\bar{1}2\}$. So if the sample axis falls into the triangle A, contraction in length occurs for all six twinning

planes; if the sample axis falls in the triangle D, extension always occurs. For the triangle B, the twinning planes II, III, V, VI result in contraction, but the planes I and IV extension. In the triangle C, however, the planes II and V cause contraction but the others extension.

The twinning deformation is relatively small compared to the deformation by slip. The twinning shear is only a fraction of the lattice parameter, but the shear can be unlimited in slip.

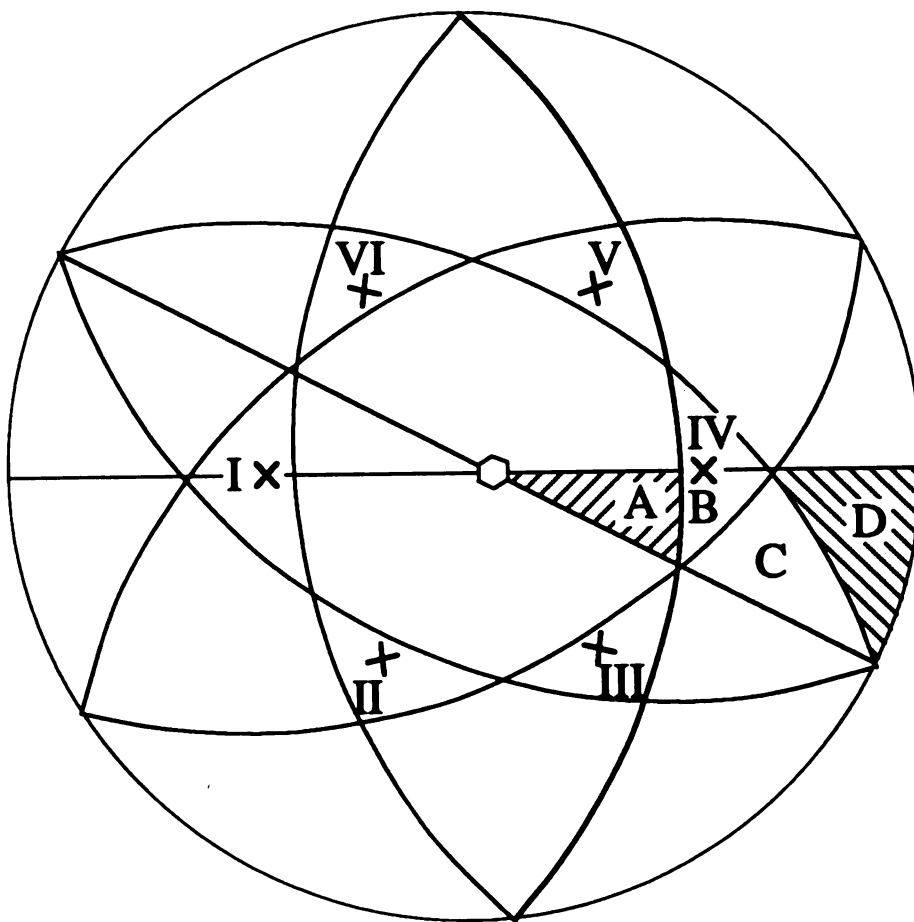


Figure 2.19 - The extension and contraction of sample length for twinning in zinc.

2.2.7. Prediction of Twinning Elements (Twinning Criterion)

According to the analysis in the previous sections, the twinning criterion should include the following points ^[68]:

- (i) the twinning shear should be small;
- (ii) the shuffle mechanism should be simple, that is, q or m should be small;
- (iii) the shuffle magnitudes should be small;
- (iv) shuffles should be parallel to the twinning direction rather than perpendicular to this direction.

The twinning criterion can be expressed in the matrix form as follows ^[70]

$$U_{ij}U_{ij} \leq g_{max}^2 + 3 \quad (2.23)$$

where g_{max}^2 is some maximum value of shear, and U_{ij} is correspondence matrix for cubic lattice that must satisfy

$$g^2 = U_{ij}U_{ij} - 3 \quad (2.24)$$

$$g_2 = U_{ij}^T U_{ij}^T - 3 \quad (2.25)$$

where g is the twinning shear, and U_{ij}^{-1} is the inverse of U_{ij} . So, for a given value of g_{max} , we can determine the correspondence matrix U_{ij} . This correspondence matrix is used to determine the twinning elements.

The twinning criterion can also be expressed in the notation of tensor calculus as^[68]

$$4(c^{ij}h_ih_j)(c_{pq}v^pv^q) < q^2(g_{max}^2 + 4) \quad (2.26)$$

where q is the shuffle parameter described in section 2.2.1, and g_{max}^2 is a given maximum value of shear. So, for given values of q and g_{max} , the values of h_i and v^i which satisfy above inequality can be determined for a lattice defined by c^{ij} or c_{ij} . Thus the twinning mode with the smallest possible g may be specified.

2.2.8 Twinning in Superlattice

Since the mechanical twinning in a superlattice was reported by Laves in 1952^[78], many experimental results on mechanical twinning in superlattices have been reported, such as the mechanical twinning in the superlattices $L1_2$ ^[79-82], B_2 ^[83-86], DO_3 ^[83,87], $L1_0$ ^[1,3,17-22,24,26-31], DO_{22} ^[88-91], DO_{19} ^[91,92]. More recently, the review papers by Christian and Laughlin^[93], Yoo^[94], and Yoo, Fu and Lee^[25] have also been published for various superlattice structures. It is commonly believed that mechanical twinning makes many important contributions to mechanical properties of ordered intermetallic alloys^[94]. In this section, the mechanical twinning modes in superlattice structures will be summarized.

The main difference between the twinning in superlattices and that in disordered structures is that the twinning shear of superlattice creates not only a true-twin in some

twinning variants but also a pseudo-twin in other twinning variants. In the pseudo-twin, the atomic sites are in twin positions but these sites are incorrectly occupied by anti-site atoms. In the true-twin, however, the twin relations of the atomic sites are not only satisfied crystallographically but also true in chemistry. True-twins may be further classified into following three types ^[93,95],

- (i) type-I/II twin, in which the direct variant gives a twin with a type-I orientation relation (equivalent to orientation relations (2.1) and (2.4)), and the conjugate variant gives a type-II orientation relation (equivalent to orientation relations (2.2) and (2.3)),
- (ii) type-II/I twin, which is the reversed of type-I/II, and
- (iii) combined twin, in which all four classical orientation relations are equivalent.

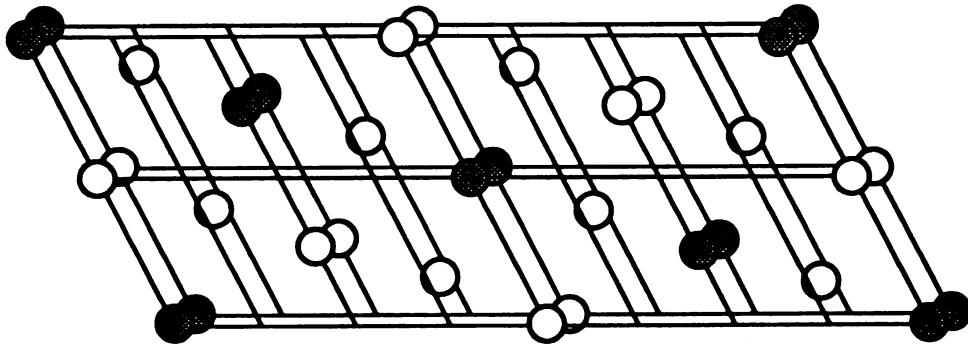
If K_1 plane is a mirror plane in the parent structure, the type-I/II is defined as type-I since the conjugate modes do not actually represent twins. Similarly, if η_1 is a two-fold axis in the parent structure, the type-II/I becomes type-II.

The twinning modes discussed in the previous sections are referred to the disordered structure. When the normal twinning mode of the disordered structure is applied to the superlattice, it frequently leads to the incorrectly ordered product, and the true-twinning mode requires a larger shear. This applies to all variants of the normal twinning mode in almost all cubic superlattices, but only to some of the variants in a non-cubic superlattice ^[93].

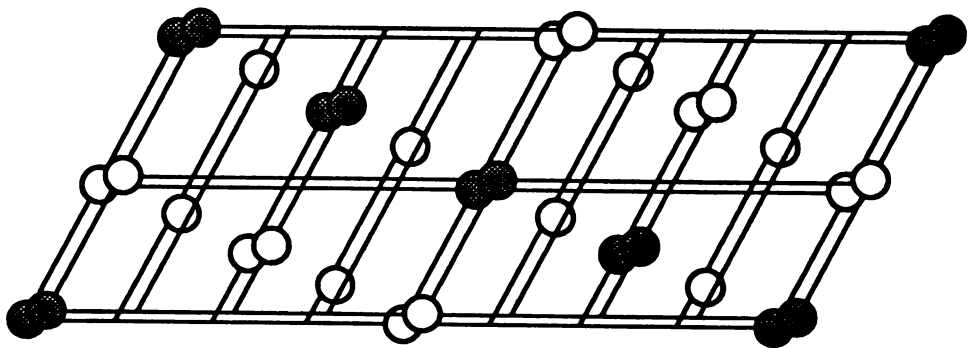
In general, for the twinning of a single lattice structure in which the primitive unit

cell contains only one atom, when the shuffle parameters q and \bar{q} are both less than or equal to 2, the superlattice twinning leads to a true-twin; otherwise, if both q and \bar{q} are larger than 2, the product of twinning is a pseudo-twin ^[93]. For the twinning of a multiple superlattice structure in which the primitive unit cell contains more than one atom, however, a structure shuffle is required. In addition, for the twinning of both single and multiple superlattice structures, an interchange shuffle (or an order shuffle) is needed to form true-twin.

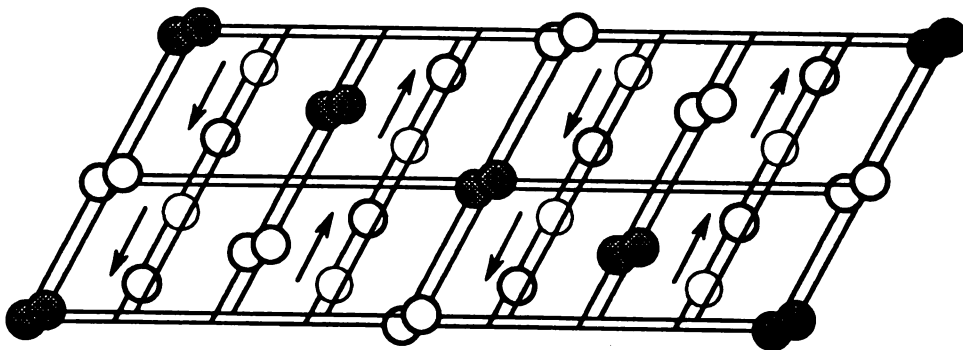
If we define a unit cell in the parent in a such way that the primitive lattice vectors are parallel to η_1 , η_2 and the positive normal to the plane of shear S , the frame of this unit cell is sheared into the cell whose frame is twin related with the parent cell. However, the further relative displacement of the atoms within the unit cell is required to complete the twinning operation and restore the original structure. This atomic displacement in the unit cell is called structure shuffle. The structure shuffle can only complete the twinning operation in crystallography but not in chemistry. So various atomic interchange shuffles in the unit cell are also necessary to obtain a true-twin. The structure shuffle and interchange shuffle are schematically shown in Fig. 2.20 which shows the formation of $(1\bar{2}0)$ twin in DO_3 ^[93]. Fig. 2.20 (a) is the parent unit cell. Fig. 2.20 (b) is the unit cell after twinning shear, which shows that the crystal structure of the parent has been changed by the simple shear. In order to finish the twinning operation, the structure shuffle is needed to restore the parent crystal structure, which is shown in Fig. 2.20 (c). Fig. 2.20 (d) shows a possible interchange shuffle configuration to produce a true-twin as shown in Fig. 2.20 (e).



(a)

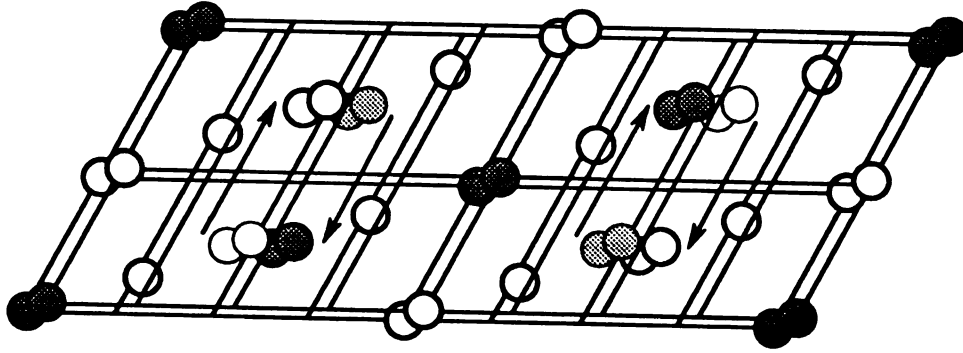


(b)

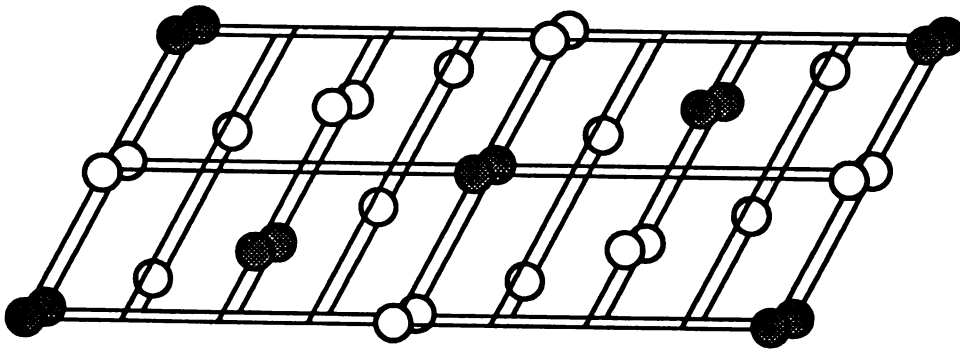


(c)

Figure 2.20 - The structure and interchange shuffles during $(\bar{1}20)$ twinning in DO_3 .



(d)



(e)

(Figure 2.20 continued)

Table 2.3 ^[93] lists some twinning modes in cubic superlattice structures which is directly derived from the modes in disordered cubic lattice structures listed in table 2.2 and from some other references ^[70,96]. The shuffles of one half of the atoms are allowed in table 2.3. The twinning modes in table 2.3 are listed in the order of increment of twinning shear.

Table 2.3. Twinning modes in cubic lattices

Mode No.(m.n)	g^2	m	m_l	m_F	Twin type
4.2	1/8	4	8	2	combined
4.2 ^{T*}	1/8	4	2	8	combined
4.5	3/8	4	2	8	II
4.5 ^T	3/8	4	8	2	I
2.2	1/2	2	4	1	combined
2.2 ^T	1/2	2	1	4	combined
2.3	1/2	2	4	2	combined
2.3 ^T	1/2	2	2	4	combined
4.10	7/8	4	8	2	I
4.10 ^T	7/8	4	2	8	II
1.2	1	1	2	2	combined
2.5	1	2	2	2	combined
2.8	3/2	2	1	4	I
2.8 ^T	3/2	2	4	1	II

Table 2.3. Twinning modes in cubic lattices. (Continued)

Mode No.(m.n)	g^2	m	m_I	m_F	Twin type
1.3	2	1	2	1	combined
1.3 ^T	2	1	1	2	combined
2.18	7/2	2	4	1	I-II
2.18 ^T	7/2	2	1	4	II-I
1.9	8	1	1	1	combined
1.9 ^T	8	1	1	1	combined

* m.n^T is the "transposed " mode obtained by interchanging K_1 and η_1 , K_2 and η_2 , and changing the signs of the new K_2 and η_1 referred to preceding twinning mode.

For the cubic superlattices B2, DO₃ and L1₂, a true-twinning mode without shuffles is predicted if a 1 appears in the shuffle columns of table 2.3 for both the disordered and the superlattice structures. For B32, however, additional examination is required in addition to the shuffle parameter equal to 1 since the primitive unit cell contains two B atoms. The possible true-twinning modes in cubic superlattices are listed in table 2.4.

For non cubic superlattices, the primary and complementary twinning modes of L1₀ (the tetragonal), DO₂₂ (the tetragonal) and DO₁₉ (the hexagonal) are listed in table 2.5 [94]. In table 2.5, λ is the ratio of c/a , which is based on disordered cell dimensions,

and $e/2$ is defined in equation $\mathbf{b}_x = (e/2) \boldsymbol{\eta}$ in which \mathbf{b}_x is the Burgers vector of a zonal twinning dislocation ^[97]. The numerical value of $(e/2)$ for the twinning mode in cubic structure is $1/3$.

Table 2.4. Possible true-twinning modes in cubic superlattices

Mode No. (m.n)	S	K_1	K_2	η_1	η_2	g^2	Structures
(a) Modes without Shuffles							
1.3	1 1 0	1 $\bar{1}$ 1	0 0 1	$\bar{1}$ 1 2	1 $\bar{1}$ 0	2	$L1_2$
1.3 ^T	1 1 0	$\bar{1}$ 1 2	$\bar{1}$ 1 0	$\bar{1}$ 1 $\bar{1}$	0 0 1	2	B2
1.9	$\bar{1}$ $\bar{1}$ 0	$\bar{1}$ 1 2	0 0 1	1 $\bar{1}$ 1	$\bar{1}$ 1 0	8	B2,B32,DO ₃ , $L1_2$
1.9 ^T	$\bar{1}$ $\bar{1}$ 0	1 $\bar{1}$ 1	1 $\bar{1}$ 0	1 $\bar{1}$ $\bar{2}$	0 0 1	8	B2,B32,DO ₃ , $L1_2$
(b) Modes with 50% (non interchange) shuffles							
2.3 ^T	1 1 0	1 $\bar{1}$ $\bar{4}$	1 $\bar{1}$ 0	2 $\bar{2}$ 1	0 0 $\bar{1}$	1/2	B2
1.2	0 0 1	1 $\bar{2}$ 0	1 0 0	2 1 0	0 $\bar{1}$ 0	1	B2, $L1_2$
2.5	0 0 1	$\bar{1}$ 3 0	1 1 0	3 1 0	$\bar{1}$ 1 0	1	B2,B32,DO ₃
1.3	1 1 0	1 $\bar{1}$ 1	0 0 1	$\bar{1}$ 1 2	1 $\bar{1}$ 0	2	B2,B32,DO ₃
1.3 ^T	1 1 0	$\bar{1}$ 1 2	$\bar{1}$ 1 0	$\bar{1}$ 1 $\bar{1}$	0 0 1	2	$L1_2$

Table 2.5. Twinning modes in non-cubic superlattices

Structure	Twin type	q	S	K ₁	K ₂	η_1	η_2	g	e/2	
									(η_1)	(η_2)
L1 ₀	P	2	$1/2\langle\bar{1}\bar{1}0\rangle$	{111}	{ $1\bar{1}\bar{1}$ }	$1/2\langle\bar{1}\bar{1}\bar{2}\rangle$	$1/2\langle 112\rangle$	$(2\lambda^2-1)/(\lambda\sqrt{2})$	$(2\lambda^2-1)/(2\lambda^2+1)$	
	C	1	$1/2\langle\bar{1}\bar{1}0\rangle$	{111}	{001}	$1/2\langle\bar{1}\bar{1}\bar{2}\rangle$	$1/2\langle 110\rangle$	$\sqrt{2}/\lambda$	$1/(2\lambda^2+1)$	1
DO ₂₂	P	2	$1/2\langle\bar{1}\bar{1}0\rangle$	{111}	{ $1\bar{1}\bar{1}$ }	$1/2\langle\bar{1}\bar{1}\bar{2}\rangle$	$1/2\langle 112\rangle$	$(2\lambda^2-1)/(\lambda\sqrt{2})$	$(2\lambda^2-1)/(2\lambda^2+1)$	
	C	2	$1/2\langle\bar{1}\bar{1}0\rangle$	{111}	{001}	$1/2\langle\bar{1}\bar{1}\bar{2}\rangle$	$\langle 110\rangle$	$\sqrt{2}/\lambda$	$2/(2\lambda^2+1)$	1
DO ₁₉	(a)	4	$\pm 1/3\langle\bar{1}\bar{1}\bar{2}0\rangle$	{ $1\bar{1}02$ }	{ $1\bar{1}0\bar{2}$ }	$\pm\langle\bar{1}\bar{1}01\rangle$	$\pm\langle\bar{1}\bar{1}01\rangle$	$\pm(3-\lambda^2)/(\lambda\sqrt{3})$	$(3-\lambda^2)/(3+\lambda^2)$	
	(b)	2	$\langle\bar{1}100\rangle$	{ $11\bar{2}1$ }	{0001}	$1/3\langle\bar{1}\bar{1}\bar{2}6\rangle$	$1/3\langle\bar{1}\bar{1}\bar{2}0\rangle$	$1/\lambda$	$1/(4\lambda^2+1)$	1

2.2.9. Mechanical Twin Nucleation and Propagation

Mechanical twinning mechanisms can be classified into three categories, that is, (1) dislocation pole mechanism ^[98-100], (2) twinning dislocation homogeneous glide mechanism ^[101,104], and (3) twin-matrix tilt boundary migration mechanism ^[105]. The main differences between them are the details in the mechanical twin nucleation and propagation. In the third model in which the twin interface is thought to be a tilt boundary, the interface dislocations glide in the planes almost normal to the twin interface. It was supposed that once such a tilt boundary was established, it could migrate easily under a very small shear stress. However, the most intensively studied model is the dislocation pole mechanism. This mechanism describes the twinning as a result of a twinning dislocation rotation around an existing pole dislocation whose screw component is perpendicular to the twinning plane and the component Burgers vector is

equal to the spacing of the planes parallel to the twinning plane ^[98,99]. Much experimental work has been done to try to validate this model. However, some experimental results had indicated that no pole dislocations existed during mechanical twinning, but mechanical twinning was found to occur by a homogeneous shearing of the twinning portion of the crystal with respect to the matrix ^[100,101].

The dislocation pole mechanisms were first proposed by Cottrell and Bilby ^[98] in 1951 for bcc crystals, Thompson ^[99] in 1952 for hcp crystals and Venables ^[100] in 1961 for fcc crystals. Since the first observation of mechanical twinning in fcc metal (in copper) was in 1957 ^[106], the twinning theory in fcc was developed much latter than those in bcc and hcp.

Since the dislocation pole mechanism has been well developed, in what follows, the dislocation pole mechanism in three common crystal structures, bcc, fcc and hcp, will be analyzed in order to illustrate the mechanical twin nucleation and propagation phenomena.

(a) Dislocation Pole Mechanism in bcc Metals

The dislocation pole mechanism in bcc metals is based on the dissociation of normal dislocation $\mathbf{b} = 1/2[111]$ in a (112) plane into two partial dislocations: a sessile $1/3[112]$ and a glissile $1/6[11\bar{1}]$, i.e.,

$$1/2 [111] \rightarrow 1/3 [112] + 1/6 [11\bar{1}] \quad (2.27)$$

Since the partial dislocation $1/6[11\bar{1}]$ is also glissile in the $(\bar{1}21)$ plane, it can cross-glide onto the $(\bar{1}21)$ plane. The rotation of this glissile partial dislocation $1/6[11\bar{1}]$ about the normal dislocation $1/2[111]$ creates a monolayer twin. Since the screw part of the normal dislocation in $[\bar{1}21]$ direction has a Burgers vector equal to the interplanar spacing of $(\bar{1}21)$ plane in length, each complete rotation of $1/6[11\bar{1}]$ partial dislocation about $1/2[111]$ normal dislocation in the $(\bar{1}21)$ plane will bring the partial dislocation onto the next adjacent $(\bar{1}21)$ plane. Continuous rotation of this partial dislocation about the normal dislocation thickens the twin layer. So the partial dislocation $1/6[11\bar{1}]$ is called twinning dislocation and the normal dislocation $1/2[111]$ is called twinning pole. The twinning plane in this case is then the $(\bar{1}21)$ plane. The propagation of the twin layer in a direction parallel to the twinning plane occurs by the glide of twinning dislocations on every twinning plane.

The twin nucleation and propagation model in bcc is schematically illustrated in Fig. 2.21. One complete rotation of twinning dislocation OF in Fig. 2.21 (a) about the twinning pole OA creates a monolayer twin, i.e., a twinning nucleus. The glide of twinning dislocations forming incoherent twin boundary, as shown in Fig. 2.21 (b), results in the propagation of twin layer along the twinning plane.

(b) Dislocation Pole Mechanism in hcp Metals

The twinning modes in hcp structures depend on the c/a ratio (λ). Table 2.6 summarizes some twinning modes in hcp metals ^[107-110]. Since the $(10\bar{1}2)$ twinning is a common twinning mode in hcp, as shown in table 2.6, the dislocation pole mechanism

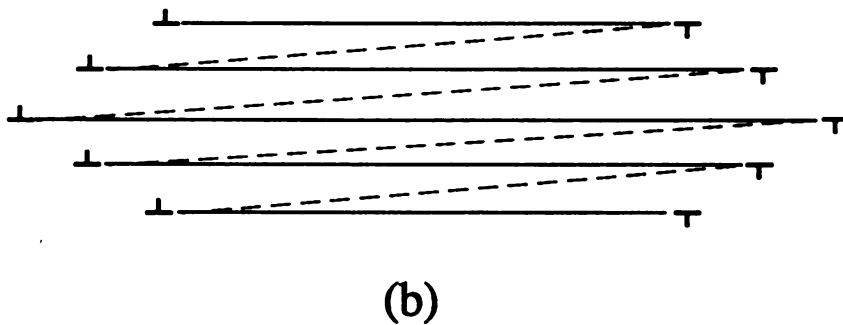
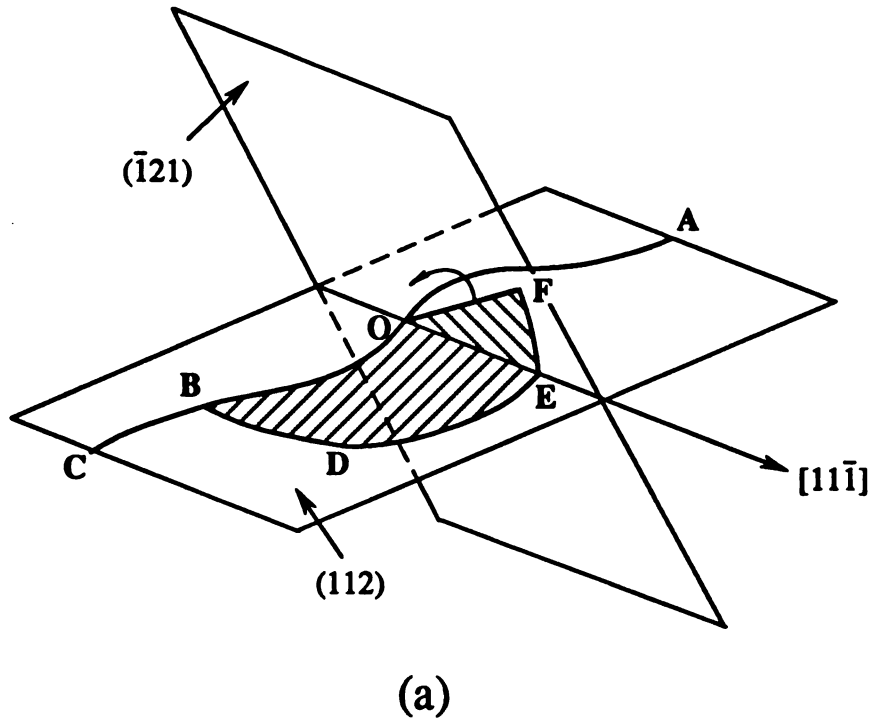


Figure 2.21 - Dislocation pole mechanism for twinning in bcc lattice.

in hcp is illustrated based on this twinning mode. In this mechanism, the homogeneous shear occurs on every other corrugated plane while the atoms between these planes are involved in a shuffle, as shown in Fig. 2.22. The Burgers vector of the zonal twinning dislocation in this case would be $(\lambda^2-3)/(\lambda^2+3) [10\bar{1}1]^{(111)}$. Fig. 2.22 shows two

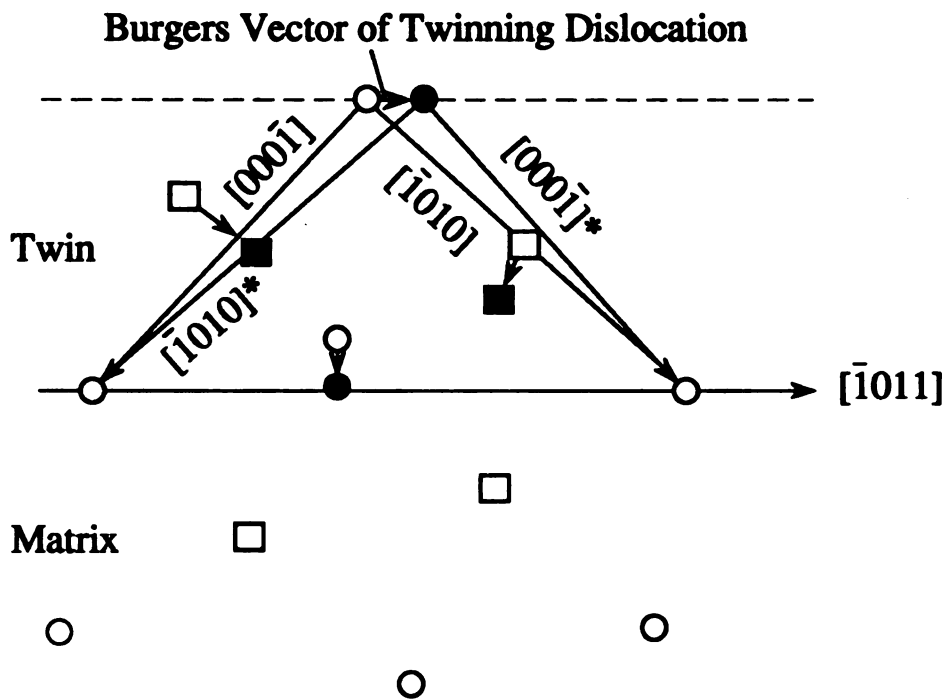


Figure 2.22 - $(10\bar{1}2)$ twinning in zirconium. Projection of the lattice on the $(\bar{1}2\bar{1}0)$ plane. Circles are in the plane of paper. Squares are $a/2$ above and below the paper. Solid symbols indicate atom positions in the twin.

possibilities for the formation of zonal twinning dislocation:

- (i) a $[000\bar{1}]$ dislocation dissociates into the zonal twinning dislocation and a $[\bar{1}010]^*$ pole dislocation (the asterisk indicates that the indexes refer to the twinned lattice);
- (ii) a $[\bar{1}010]$ dislocation dissociates into a zonal twinning dislocation and a $[000\bar{1}]^*$ pole dislocation.

Thus, as the zonal twinning dislocation finishes a revolution about the pole dislocation, it will be on the next adjacent twinning plane.

Table 2.6. Twinning modes in hcp metals

q	S	K ₁	K ₂	η ₁	η ₂	g	c/a
4	$\bar{1}210$	$10\bar{1}2$	$10\bar{1}2$	$\bar{1}011$	$10\bar{1}1$	$(\lambda^2-3)/(\lambda\sqrt{3})^*$	all
8	$\bar{1}210$	$10\bar{1}1$	$10\bar{1}3$	$10\bar{1}2$	$30\bar{3}2$	$(4\lambda^2-9)/(4\lambda^4\sqrt{3})$	≈ 1.633
6	$1\bar{1}00$	$11\bar{2}2$	$11\bar{2}4$	$11\bar{2}3$	$22\bar{4}3$	$(2\lambda^2-4)/3\lambda$	$\langle 1.633$
2	$\bar{1}100$	$11\bar{2}1$	0002	$\bar{1}126$	1120	$1/\lambda$	$\langle 1.633$

* $\lambda = c/a$

(c) Dislocation Pole Mechanism in fcc Metals

The dissociation of normal dislocation $1/2[110]$ in fcc lattice is as follows:

$$1/2 [110] \rightarrow 1/3 [111] + 1/6 [11\bar{2}] \quad (2.28)$$

But rotation of the $1/6[11\bar{2}]$ twinning dislocation about the nodes would be confined to the (111) plane, and after the formation of a monolayer twin by one revolution, the twinning dislocation would reunite with the sessile $1/3[111]$ dislocation to reform $1/2[110]$ dislocation. This reformed $1/2[110]$ dislocation would glide onto the next (111) plane and dissociate into $1/3[111] + 1/6[11\bar{2}]$ again, so that the revolution of twinning dislocation $1/6[11\bar{2}]$ is in a new (111) plane. Repetition of this dissociation-revolution-reunion procedure thickens the twin layer. This mechanism is schematically shown in Fig. 2.23 ^[100]. At beginning, a normal dislocation AC lies in plane (a) between the nodes

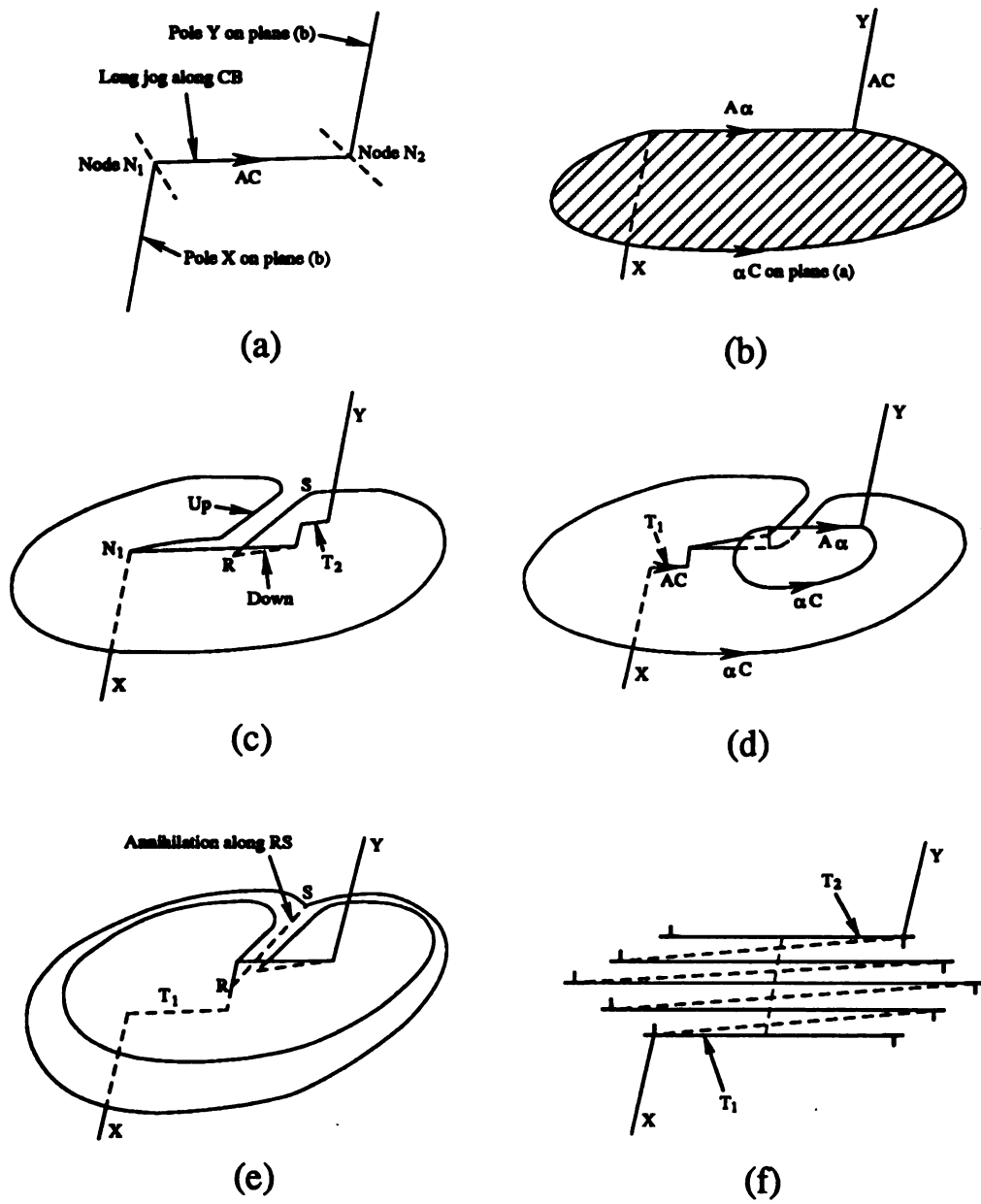


Figure 2.23 - Dislocation pole mechanism in fcc lattice.

N_1 and N_2 , and the poles X and Y lie on plane (b), as shown in Fig. 2.23 (a). The normal dislocation AC dissociates into $A\alpha + \alpha C$ on (a) plane as shown in Fig. 2.23 (b), and when the twinning dislocation line reaches a semicircle it is unstable and quickly extends to the configuration as shown in Fig. 2.23 (c). The partials marked "up" and "down" in Fig. 2.23 (c) reunite with $A\alpha$ to form AC, and a unit jog traveling along the AC from the node N_2 (or N_1) move the AC into the next (a) plane and repeat the revolution as shown in Fig. 2.23 (d) and (e). In this way, a lenticular twin can be built up, as shown in Fig. 2.23 (f). The twin thickness is limited by the backward stress and by the length of the pole dislocation.

2.2.10. Twin Shape

There are two models to predict the twin shape: one model considers system energy change associated with twin nucleation and propagation, and the other model considers forces acting on individual twinning dislocations. These two models have been frequently used in modelling the mechanical twinning behavior and predicting the twin shape ^[112-114].

(a) A Model Concerning The Energy Change Associated With Twinning

The energy associated with twinning was expressed by Cooper in 1965 ^[115]. When we predict the equilibrium shape of a twin, we usually consider the minimum total energy change in the specimen during the twinning. This can be done by differentiation of an expression for the total energy of the twinned specimen.

The energy terms considered in this model are:

- (i) twin boundary energy, which corresponds to the twin boundary surface tension;
- (ii) twinning dislocation interaction energy, which corresponds to the mutual repulsive forces between the twinning dislocations making up the incoherent twin boundaries;
- (iii) the elastic strain energy due to the external stresses (the externally applied stress and the local stress concentration);
- (iv) dislocation line energy due to the dislocation line tension.

The expressions of these four energy terms reported by Cooper ^[115] are briefly summarized in the following section.

(1) Twin Boundary Energy

The twin boundary energy is equal to the twin boundary surface energy multiplied by the total twin boundary area:

$$E_t = A\gamma h(p-1) \quad (2.29)$$

where A is a twin shape constant, $A = 1$ when one side boundary of twin is considered, $A = 2$ when considering both side boundaries; h is the spacing between neighboring twinning dislocations in the incoherent twin boundary; p is the total number of twinning dislocations in one side of a twin boundary. When the twin boundary consists of a large number of twinning dislocations, the twin boundary energy term can be expressed as

$$E_1 = A\gamma hp. \quad (2.30)$$

(2) Twinning Dislocation Interaction Energy

Since the length and the width of a twin are much larger than the spacing between the twinning dislocations which form the incoherent twin boundary, the twinning dislocations can be thought to be parallelly distributed. In addition, the following two assumptions are made for the expression of dislocation interaction energy term: (i) any pair of twinning dislocations will have zero interaction energy when separated by a suitably large distance L ; (ii) the twin is reasonably thin compared with its length so that the dislocations behave as if all are in the same glide plane but there is no interaction between one boundary and the other. The twinning dislocation interaction energy (E_2) for one side of twin boundary is as follows,

$$E_2 \approx \frac{Gb^2}{2\pi(1-\nu)} \left[p^2 \ln \frac{L}{h} - K(p) \right] \quad (2.31)$$

where

$$K(p) = \ln(p-2)! + \sum_{i=2}^{i=p-1} [\ln(p-1)! + \ln(i-1)!] \quad (2.32)$$

G is the elastic shear modulus, b is the Burgers vector of a twinning dislocation, and ν is Poisson's ratio.

(3) Strain Energy Due to The External Stress

The work done by the externally applied shear stress on the formation of a twin,

i.e., the strain energy, is expressed as

$$E_3 = 2g\tau_o a p^2 f(\alpha) h \quad (2.33)$$

where g is the twinning shear,

τ_o is the applied shear stress,

a is the interplanar spacing of the twin composition plane, and

$$f(\alpha) = \alpha^{-2} (e^{-\alpha} - 1) + \frac{1}{\alpha}. \quad (2.34)$$

If $\alpha = 0$, $f(\alpha) = 1$, and if α is large, $f(\alpha) \rightarrow 1/\alpha$.

(4) Twinning Dislocation Line Energy

The total dislocation line energy on one side of a twin boundary is

$$E_4 = 0.5pGb^2. \quad (2.35)$$

Therefore, the total energy on one side of a twin boundary associated with twinning is the summation of all these four energy terms, that is,

$$E = E_1 + E_2 + E_3 + E_4 \quad (2.36)$$

or

$$E = \gamma h (p-1) + \frac{Gb^2}{2\pi(1-\nu)} \left[p^2 \ln \frac{L}{h} - K(p) \right] + 2g\tau_o a p^2 f(\alpha) h + \frac{1}{2} p G b^2. \quad (2.37)$$

It must be noted that in this model the energy due to the lattice friction on twinning dislocations is not considered.

(b) A Model Based on Twinning Dislocation Interaction Forces

Cooper ^[116] first proposed a model based on twinning dislocation interaction forces in 1966. Marcinkowski and Sree Harsha ^[117] first used this model to predict the twin shape. This model has also been used by others to predict twin shape ^[108,112].

The forces considered in this model include

- (i) the force due to the surface tension of twin interface,
- (ii) the force due to the twinning dislocation line tension,
- (iii) the force due to the applied stress
- (iv) the force due to the repulsion between twinning dislocations.

This model can give more detailed results than the model considering the system energy change. The expression of each force in this model is briefly summarized in the following.

(1) The Force Due to The Surface Tension

The force due to the surface tension, $F_{S.F.}$, is numerically equal to the specific surface energy,

$$F_{s.T.} = -\gamma \quad (2.38)$$

where γ is the twin boundary energy. The negative sign in the equation indicates that the positive direction of this force points to the outside of the surface considered. The unit is dyn/cm or N/m.

The twin plane energy is approximately equal to one half of the intrinsic stacking fault energy. This is because the number of mis-stacking with respect to the second neighbor planes across the intrinsic stacking fault has twice as many as that across the twin plane.

(2) The Force Due to The Twinning Dislocation Line Tension

The line tension of a dislocation half loop causes a force (per unit length), $F_{L.T.}$, on the edge part of the loop,

$$F_{L.T.} = - 2Gb^2/l \quad (3.39)$$

where G = the shear modulus,

b = the Burgers vector,

l = the radius of curvature of the dislocation loop at the twin tip.

(3) The Force Due to The Applied Stress

This force (per unit length), F_s , is equal to the resolved shear stress times the

Burgers vector,

$$F_a = \tau b. \quad (2.40)$$

The applied stress can be either the externally applied stress, or the locally concentrated stress, or the residual stress in the matrix, or all of them.

(4) The Force Due to The Twinning Dislocation Interaction

Since the twinning dislocations in a twin boundary are all the same type of dislocations, i.e., they have the same Burgers vector, the interaction force between them is repulsive. The dislocation interaction force, F_d , between two twinning dislocations, b_1 and b_2 , can be expressed as follows

$$F_d = \frac{G}{2\pi(1-\nu)R} [b_1 \times \zeta] \cdot (b_2 \times \zeta) + \frac{G}{2\pi R} [(b_1 \cdot \zeta) * (b_2 \cdot \zeta)] \quad (2.41)$$

where ζ is the dislocation line direction,

R is the distance between two dislocations,

G is the shear modulus,

ν is Poison's ratio.

Since many twinning dislocations are involved in a twin boundary, the total interaction force on a twinning dislocation (on the m th twinning dislocation in this case) will be the sum of all interaction forces,

$$F_{d.m.} = \frac{G}{2\pi R} \sum_{\substack{i=1 \\ i \neq m}}^n \left[\frac{1}{1-\nu} (b_m \times \zeta) \cdot (b_i \times \zeta) + (b_m \cdot \zeta) * (b_i \cdot \zeta) \right] . \quad (2.42)$$

The total force on a twinning dislocation (on the m th twinning dislocation) is equal to the sum of all these forces,

$$F_m = F_{S.T.} + F_{L.T.} + F_a + F_{d.m.} \quad (2.43)$$

2.3. Creep Theory

Creep is defined as a time dependent deformation. Creep deformation mechanisms are strongly dependent upon temperature and applied stress. At sufficiently low temperatures ($T < 0.3T_m$) (T_m is the melting temperature of the materials concerned), when the applied stress is less than the elastic limit of a specimen, only elastic strain occurs; when a higher stress (less than a stress needed to cause immediate fracture) is applied to a ductile specimen, both elastic and plastic strains occur within the specimen on loading, and a subsequent time dependent strain accumulates while the stress is maintained on the specimen, which is called logarithmic creep. The logarithmic creep results in only very limited creep strains ($< 1\%$) and does not cause eventual fracture. However, as the temperature increases to above $0.4T_m$, the deformation appears as a normal creep, the curve of which usually shows primary, secondary and tertiary stages. Since logarithmic creep is generally of very limited practical significance, normal creep (to be called creep hereafter) will be discussed in the following sections.

2.3.1. Microstructural Correspondences to Creep

Microstructural response to creep deformation varies with stress, strain, temperature and materials. During creep of most metallic materials, particularly those characterized by a high stacking fault energy, a relatively uniform dislocation arrangement initially observed changes gradually as a result of the formation of a subgrain structure. In the early primary stage, a heterogeneous subgrain structure forms, that is, a high density of subgrains form in some region but not in others. With increasing primary creep strain, the subgrain structure becomes more homogeneous; the average misorientation across the sub-boundaries increases and remains constant at about 1° - 2° throughout the secondary stage ^[118,119]. Although the average subgrain size at a certain stress is observed to remain constant in the secondary stage, the locations of sub-boundaries do not appear to be fixed.

The total dislocation density appears to increase with increasing strain in the primary stage and to become constant during the secondary stage. It has also been reported for various materials that coarse slip bands form during creep deformation ^[120-122]. The average spacing of slip bands decreases with increasing stress.

Grain boundary sliding is thought to be significant particularly for creep at high temperatures and low stress and for small grain size materials. The activation energy of grain boundary sliding is between the values for self-diffusion in the lattice and along grain boundaries ^[123]. In general, at the same stress and temperature, a decrease in average grain size decreases creep resistance ^[124,125]. The creep rate is insensitive to

grain size for dislocation creep except with very fine grain size, for which the increase in creep rate is attributed to an increase in the contribution of grain boundary sliding to the overall strain rate ^[121,126]. However, in the low stress or diffusional creep regime, the creep rate increases rapidly with decreasing grain size.

2.3.2. Mechanical Model

The creep deformation at elevated temperature, $T \geq 0.4T_m$, is generally expressed in a form of ^[127]

$$\dot{\epsilon}_{ss} = A \frac{GbD_0}{kT} \left(\frac{b}{d} \right)^p \left(\frac{\sigma}{G} \right)^n \exp(-Q_c/RT) \quad (2.44)$$

where $\dot{\epsilon}_{ss}$ = the steady state creep rate,

A = the pre-exponential (structural) constant,

G = the shear modulus,

D_0 = the frequency factor,

k = Boltzmann's constant,

T = the absolute temperature,

b = the Burgers vector,

d = the grain size,

p = the grain size exponent,

σ = the imposed stress,

n = the creep stress exponent,

Q_c = the activation energy for creep,

R = the ideal gas constant.

In this equation, the stress exponent " n " indicates a specific creep deformation mechanism, the activation energy " Q_c " indicates the rate limiting deformation process of creep, and the grain size exponent " p " indicates the extent of grain size dependence of creep.

Therefore, the creep deformation mechanisms, in general, can be characterized by these three values, Q_c , n and p . A number of creep deformation mechanisms are summarized in table 2.7 in terms of these three values. In table 2.7, Q_l , Q_{gb} , Q_p and Q_i are the activation energies for lattice self diffusion, grain boundary diffusion, pipe diffusion and interdiffusion of solute atoms, respectively, and B is a constant.

Diffusional creep (Nabarro-Herring or Coble creep) is considered to be important at stresses that are too low for dislocation creep processes to be significant. Nabarro-Herring creep is characterized that the steady state creep rate is controlled by diffusion through the lattice ^[128,129]. In Coble creep, the creep rate is determined by grain boundary diffusion ^[130].

Harper-Dorn creep is characterized by a stress and temperature dependence of the steady state creep rate comparable with the values expected for diffusional creep processes, but deformation occurs by the generation and movement of dislocations ^[131]. This indicates that stress exponents close to unity are not necessarily indication of diffusional creep.

Table 2.7. Creep Deformation Mechanisms At Temperature $T \geq 0.4T_m$

Temperature	Stress	n	Q_c	p	Mechanism
Low	Low	1	Q_{gb}	3	Coble diffusion creep
		1	Q_l	0	Harper-Dorn creep
	Intermediate	7	Q_p	0	Climb recovery (L.T.)
	High	$\dot{\epsilon} = A \cdot \exp(B\sigma)$	$Q_l(?)$	0	Power-law breakdown
High creep	Low	1	Q_l	2	Nabarro-Herring diffusion
		1	Q_l	0	Harper-Dorn creep
	Intermediate	5	Q_l	0	Climb recovery (H.T.)
		3	Q_i	0	Viscous glide
	High	$\dot{\epsilon} = A \cdot \exp(B\sigma)$	$Q_l(?)$	0	Power-law breakdown

Dislocation creep is classified into two types, alloy type (Class I or Class A) and pure metal type (Class II or Class M) ^[132]. In general, the creep of Class I or alloy type materials is thought to be governed by the dislocation glide that becomes the slowest step due to the viscous drag exerting on a moving dislocation by its solute atmosphere ^[133,134], where n is equal to 3. However, for pure metal type or Class II materials, the creep rate is controlled by dislocation climb processes in which n is generally close to 5.

A change in p value from 2 to 3 should accompany the change in Q_c value from that for lattice diffusion to that for preferential diffusion along grain boundaries, as a transition from Nabarro-Herring creep to Coble creep occurs with decreasing temperature.

2.3.3. Microstructural Model

Diffusional creep occurs by stress induced vacancy flow at low stresses. The vacancy flow from boundaries experiencing a tensile stress to those experiencing compression may occur predominantly through the lattice or along the grain boundaries depending on the stress and temperature applied. In this case the grain boundaries are assumed to be perfect sources and sinks for vacancies. In the case of high dislocation density and large grain size conditions, the vacancy flow along the dislocation cores, the pipe diffusion may be the significant creep deformation mechanism.

For dislocation creep, two mechanisms exist: dislocation climb controlled creep and dislocation glide controlled creep. Dislocation climb controlled creep (e.g. recovery creep, jerky glide creep, network growth theory) is based on a three dimensional dislocation network observed in steady state creep ^[135,136]. Under the applied stress, dislocations are generated to form dislocation network. Some dislocations in the network can break away due to thermal fluctuations. The released dislocation can move through the network and at the same time refine the dimension of the network. This process is responsible for the work hardening stage of creep. The recovery process takes place by the annihilation of dislocations in the network walls. Recovery results in a time

dependent increase in the dimension of network and decrease in dislocation density. At a sufficiently long time, the hardening and recovery processes will balance to give a constant creep rate. In this model, the slip process is athermal and can not occur until the recovery has changed the substructure sufficiently.

Contrary to the recovery creep, in dislocation glide controlled creep (or viscous glide creep) the rate controlling process is the rate of dislocation movement in their slip planes. The slip rate is controlled by the diffusion of solute atoms or by the non-conservative motion of jogs on screw dislocations ^[137-139]. At high temperatures, where the jogs on dislocations will be saturated with vacancies, the rate of movement of the dislocations will depend on the rate of emission and absorption of vacancies that is equal to the rate of vacancy diffusion from the dislocations to the sinks.

CHAPTER THREE

MECHANICAL TWIN NUCLEATION AND PROPAGATION IN TiAl

Mechanical twinning has long been thought to occur in crystalline materials only at low temperature and high strain rate deformation conditions. However, several recent studies in intermetallic compound TiAl have shown that the mechanical twinning not only occurs at room temperature under the normal tensile testing conditions ^[4,27] but also in creep deformation conditions ^[22,26,28,30,140], i.e., at intermediate temperatures and very low strain rates. The contributions of mechanical twinning to the deformation of TiAl have been shown to be significant.

In addition, Jin ^[28] analyzed the mechanical twinning behavior in creep deformation and found that pseudo-twinning obeyed a maximum resolved shear stress criterion. Mechanical twinning accommodation of the stress concentration at grain triple points has also been observed ^[30]. This mechanical twinning led to formation of zigzagged grain boundaries that would resist grain boundary sliding during creep deformation.

However, the details about mechanical twinning in TiAl, such as how the mechanical twins nucleate, how they grow and what type of morphology they have, have

not been clearly understood. In order to understand the mechanical twinning mechanisms in TiAl, the mechanical twin nucleation and propagation phenomena are studied using the electron beam illuminating method in this chapter. The electron beam illuminating method permits the investigation of mechanical twin nucleation and propagation processes *in situ*. The results are analyzed in terms of the maximum resolved shear stress criterion. The twin nucleation and propagation mechanisms are discussed. Based on the observed results, a mechanical twin nucleation and propagation mechanism in TiAl is proposed.

3.1. Material and Experimental Procedure

The material used in this study was investment cast γ TiAl made by Vacuum Arc Remelting (VAR) and casting at Howmet Corp., Whitehall, MI. Cast rods (152 mm in length and 16 mm in diameter) were HIP'ed (Hot Isostatic Pressed) at 1260 °C, 172 MPa for 4 hours to eliminate solidification porosity. The composition of this material is shown in table 3.1. The material was then heat treated in inert Ar atmosphere at 1300°C

Table 3.1 Composition of the γ TiAl specimens

	Ti	Al	Nb	Cr	Fe	Cu	Si	O	N	H
(wt%)	bal	32.85	4.47	2.95	0.03	<0.01	0.02	555ppm	53ppm	23ppm
(at%)	bal	47.4	1.9	2.2						

for 20 hours and gas fan cooled with a cooling rate of 65 °C/min to produce a duplex microstructure with ($\gamma + \alpha_2$) lamellar grains plus equiaxed γ grains. The rods were machined into 62 mm long tensile specimens having a 25 mm gage length and diameter of 5 mm.

The specimens were deformed in tension in an ATS Stress-Relaxation/Creep testing machine. Strain was measured using an external extensometer. Two specimens were investigated for the study of twin nucleation and propagation mechanisms:

- (i) The first specimen investigated was creep deformed under a constant stress, 176 MPa, at 765 °C in air to the strain of 4%, near the end of primary creep, and furnace cooled under the load.
- (ii) The second specimen investigated was deformed under a multi-stress-jump creep condition at 765 °C in air with an initial stress of 290 MPa, a final stress 103 MPa and a total strain of about 20 %. The specimen was furnace cooled to room temperature at the final stress.

The temperature gradient along the gage length was less than 3 °C for both specimens.

For TEM investigation, 0.7 mm thick slices were cut in both longitudinal and transverse directions from both crept specimens. 3 mm diameter disks were cut from the slices using an ultrasonic cutting machine and ground to about 0.1 mm thick. The disks were finally thinned using a double jets electropolishing system using a 10% sulfuric acid + methanol solution at -20 °C. The electron beam illuminating technique was used in order to directly observe the mechanical twin nucleation and propagation behavior. The

investigation was performed in a HITACHI H800 transmission electron microscope at 200 kV.

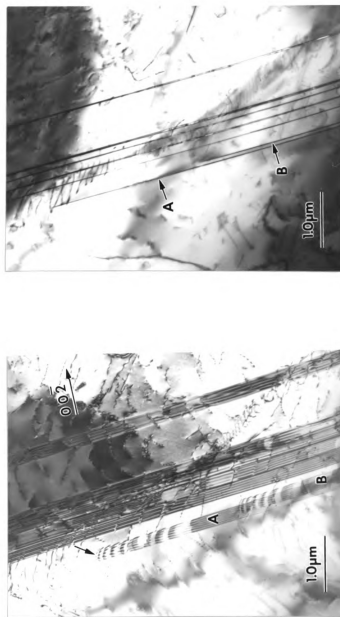
3.2. Results and Analyses

3.2.1. *In Situ* Observations of Mechanical Twin nucleation and Propagation

(a) Twin nucleation at Grain Boundaries

The electron beam illuminating method is a useful technique for investigating the dislocation movement *in situ* in a normal transmission electron microscope. When the electron beam hits the sample in TEM, the sample is heated due to the dissipated energy from the electron beam. Therefore, the dislocation motion can be thermally activated. If the local stress concentration exists in the place where the electron beam is illuminating, the local stress may be relaxed by emission of dislocations. Since the creep specimen investigated was cooled under the applied creep stress, the local stress state at grain triple points and grain boundaries at the applied creep stress was frozen. When the sample was heated by the electron beam without any external stress, the frozen local residual stress could be relaxed by the emission of dislocations at the grain boundaries.

Mechanical twin nucleation and propagation were observed *in situ* using the electron beam illuminating method. Fig. 3.1 shows images of an intermediate stage of a twin propagation event. Fig. 3.1 (a) is the tilted image of fine mechanical twins within



(b)

(a)

Figure 3.1 - Mechanical twin propagation configuration which was observed *in situ* in TiAl: (a) the tilted image of fine mechanical twins within a grain interior; (b) the image of fine mechanical twins viewed parallel to the twinning plane; (c) the diffraction pattern across several fine twin layers; and (d) indexes of the diffraction pattern which shows a twin relationship across the twin-matrix interfaces.

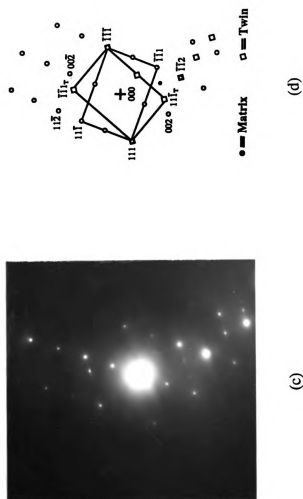


(Figure 3.1 continued)

a grain interior, and Fig. 3.1 (b) is the image of fine mechanical twins viewed parallel to the twinning plane. The sequential images of twin nucleation and propagation resulting in the current twin configuration were not recorded although it was observed *in situ*. The diffraction pattern taken across the thin twin layers is shown in Fig. 3.1 (c). The indexed diffraction pattern is shown in Fig. 3.1 (d). These fine twin layers originated at a grain boundary and propagated toward the grain interior by the emission of twinning dislocations at the grain boundary.

The observed formation of the fine twin layers is schematically drawn in Fig. 3.2. At first, a twinning dislocation was formed at a grain boundary, and then, this dislocation gradually bowed out from the grain boundary, Fig. 3.2 (a). After the dislocation bowed out to a certain radius, it left the grain boundary and moved very quickly toward the grain interior. This dislocation left a stacking fault behind it, Fig. 3.2 (b), which was a twin nucleus. This twin nucleus did not grow further until the second twinning dislocation was emitted from the grain boundary. The second twinning dislocation caught up to the first one quickly after it left the grain boundary, and it appeared to push the leading twinning dislocation further away from the grain boundary. In some instances, two twinning dislocations, which might be in two adjacent twinning planes and were very close to each other, were observed to bow out simultaneously, Fig. 3.2 (c), and propagated together, Fig. 3.2 (d). The emission of subsequent individual twinning dislocations following the second one was similar to that of the second one and the trailing twinning dislocations appeared to push the leading twinning dislocations to move forward. The twin propagation occurred by the continuing emission of twinning

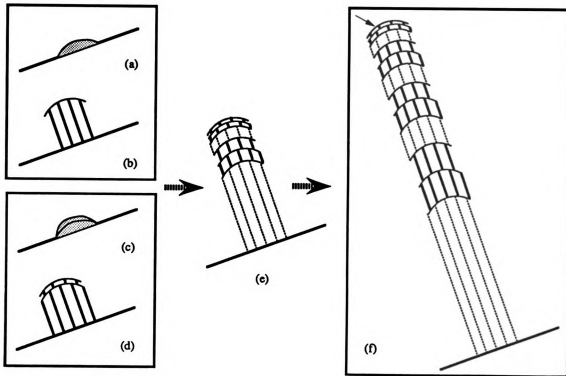


Figure 3.2 - Schematic diagram of mechanical twin nucleation and propagation procedure in TiAl, which shows that the mechanical twin nucleates at a grain boundary and propagates into the grain interior. (a) and (b) are the configuration of mechanical twin nucleation at the grain boundary with the emission of one twinning dislocation from the grain boundary; (c) and (d) are the same configuration as (a) and (b) except that two twinning dislocations are emitted from the grain boundary simultaneously; (e) is an intermediate state of twin propagation; and (f) is the final state in which the twin propagation ceases in the grain interior as twin layers **A** and **B** in Fig. 3.1 (a).

dislocations from the grain boundary, Fig. 3.2 (e) and (f).

Once a twinning dislocation was emitted, it glided quickly in its own slip plane to a position near but behind the previously emitted twinning dislocations. The effect of this phenomenon is evident in the twin layers indicated by letters **A** and **B** in Fig. 3.1 (a), which were at an intermediate stage of twin propagation. The spacing between two twinning dislocations varied depending on their locations with reference to the leading dislocation, which is indicated by an arrow in Fig. 3.1 (a) and Fig. 3.2 (f). The dislocations located near the leading dislocation are more closely spaced than the dislocations farther away from the leading dislocation.

From analysis of crystal orientations of matrix and twins in Fig. 3.1 (a) and (b) according to the diffraction pattern given in Fig. 3.1 (c) and (d), the interface between the thin twin layer and the matrix, i.e., the twin plane, was determined to be a (111) plane, and the twin propagation direction in Fig. 3.1 was determined to be the $[1\bar{1}2]$ direction. It is easily seen in Fig. 3.1 (c) and (d) that the crystal direction $[\bar{1}\bar{1}0]$ in the matrix is parallel to the crystal direction $[\bar{1}\bar{1}0]$ of the twin. This is the case of the antiparallel ($A // A'$) orientation relationship between two γ laths, which gives a true twin relation between two adjacent γ lamellae, as defined by Yamaguchi and Umakoshi^[141]. It is also the true twin condition in which the orientation variant A, $[\bar{1}\bar{1}0]$, in one γ lath is parallel to the orientation variant B, $[\bar{1}\bar{1}0]$, in the other γ lath ($A // B$) as defined by Yang and Wu^[64]. Therefore, these thin twins in Fig. 3.1 are true twins. The twinning system of the thin twin layers in Fig. 3.1 thus must be (111) $[1\bar{1}2]$, and the

Burgers vector of the twinning dislocations must be $1/6[11\bar{2}]$ ^[28,30,94], a Burgers vector of Shockley partials. In order to form a true twin, each twinning dislocation must glide on each adjacent (111) plane. Therefore, we can determine that the mechanical twin nucleus in Fig. 3.2 (b) is an intrinsic stacking fault. Similarly, in the case that the two twinning dislocations emitted from the grain boundary as in Fig. 3.2 (d), the twin nucleus is an extrinsic stacking fault including two adjacent (111) planes. However, after the third twinning dislocation emission, the twin layer does not possess any specific stacking fault feature, but it does create a four atomic layer twin. Subsequent twinning dislocation emission on the next twinning plane causes the twin to become thicker. These emitted twinning dislocations form an incoherent twin boundary at the edge of the twin layer, and the migration of this incoherent twin boundary results in the propagation of twin layer. Therefore, the incoherent twin boundary of twin layers A and B in Fig. 3.1 can be characterized as shown in Fig. 3.3. The boundary between any two adjacent twinning dislocations beyond the third twinning dislocation are identical and have the feature of (111) twin plane. According to the incoherent twin boundary structure shown in Fig. 3.3, the true-twin plane energy can be estimated to be about one half of the intrinsic or extrinsic stacking fault energy in TiAl, assuming that the intrinsic stacking fault energy and the extrinsic stacking fault energy are equal to one another. Based on the intrinsic stacking fault energy existing in the literature, 70 mJ/m^2 ^[6], the true twin plane energy in TiAl is about 35 mJ/m^2 .

The twinning elements for twins in Fig. 3.1 are easily characterized, and the result is listed in table 3.2. The relative orientations between them are shown in Fig.

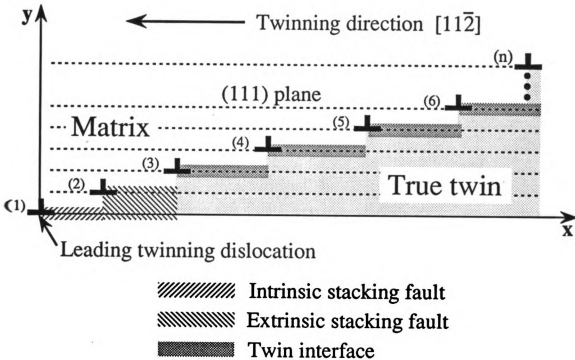


Figure 3.3 - Schematic diagram of the incoherent twin boundary structure in terms of individual twinning dislocations, which is viewed in $[110]$ direction. The boundary between the first dislocation and the second dislocation at the twin tip is an intrinsic stacking fault, the boundary between the second and the third dislocations is an extrinsic stacking fault, and the boundary between any two adjacent dislocations after the third dislocation is a twin plane. The twinning dislocations are denoted by numbers: the leading dislocation at the twin tip is counted as the first dislocation, the one just behind it is the second one, and so on.

3.4, which is viewed along $[\bar{1}\bar{1}0]$ direction. The dashed line in Fig. 3.4 indicates the position of K_2 plane after true-twinning.

Table 3.2. The mechanical twinning elements in Fig. 3.1

K_1	K_2	η_1	η_2	Shear
(111)	(11 $\bar{1}$)	[11 $\bar{2}$]	[112]	0.707

The Schmid factors of all possible twinning directions in the (111) twin plane were calculated with respect to the tensile axis of the creep specimen. The result in table 3.3 shows that the operating twinning system, the twinning system (111)[11 $\bar{2}$], in this

Table. 3.3 Schmid factors on all possible twinning systems within the (111) plane

Twinning System	Schmid Factor
(111)[11 $\bar{2}$]	0.0364
(111)[$\bar{2}$ 11]	-0.4372
(111)[1 $\bar{2}$ 1]	0.3783

Case is not the one with the highest Schmid factor with respect to the applied creep stress state. This indicates that the mechanical twin nucleation and propagation in Fig. 3.1 is

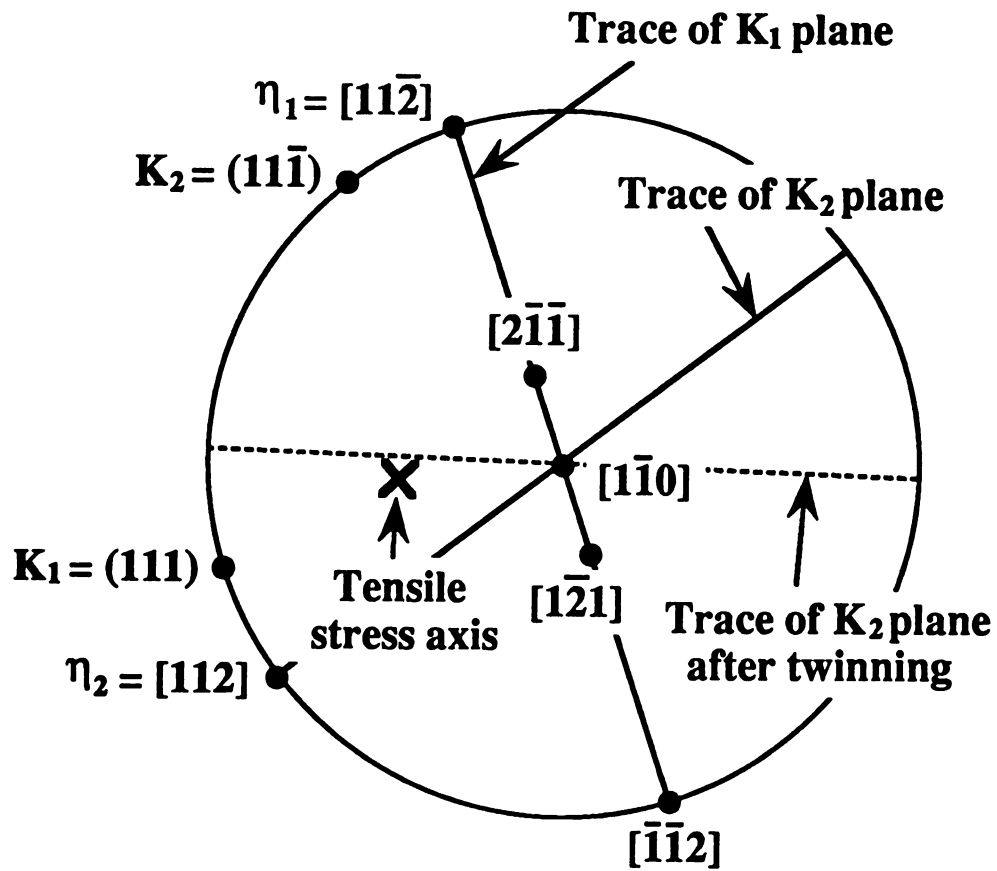


Figure 3.4 - Crystal orientation relationships of the twinning elements and the possible twinning directions in (111) plane. The cross mark indicates the direction of creep tensile axis.

not related to the applied creep stress but it is a result of the local stress concentration. Based on this result, a local principal stress state that caused the $(111)[\bar{1}\bar{1}\bar{2}]$ twinning is determined by assuming that the tensile local principal stress is such that it makes the Schmid factor on $(111)[\bar{1}\bar{1}\bar{2}]$ twinning system the largest, as shown in Fig. 3.5, although the actual local stress state might be much more complicated. The equal Schmid factor contour lines in Fig. 3.5 are plotted with respect to the $(111)[\bar{1}\bar{1}\bar{2}]$ twinning system. This shows that the principal axis of the local tensile stress for $(111)[\bar{1}\bar{1}\bar{2}]$ twinning in TiAl should be in the vicinity of the crystal direction of $[5\bar{5}1]$ within the grain where the twinning occurs.

Twinning dislocations were observed to be emitted from the grain boundary in this case. But investigating the grain boundary by tilting the sample in TEM, we did not find any evidence of existence of dislocation poles in the grain boundary as indicated in the dislocation pole mechanism ^[98,100,142]. Based on the experimental observation that the mechanical twins in Fig. 3.1 were formed by glide of $1/6[\bar{1}\bar{1}\bar{2}]$ twinning dislocations, it can be proposed that the twin propagation observed in this case occurs by a $1/6[\bar{1}\bar{1}\bar{2}]$ twinning dislocation homogeneous glide mechanism, that is, $1/6[\bar{1}\bar{1}\bar{2}]$ twinning dislocations glide homogeneously on every adjacent (111) twinning plane with one $1/6[\bar{1}\bar{1}\bar{2}]$ twinning dislocation on each (111) twinning plane. This twin propagation mechanism is schematically illustrated in Fig. 3.6. The left side column in Fig. 3.6 shows the glide sequence of $1/6[\bar{1}\bar{1}\bar{2}]$ twinning dislocations in the (111) twinning plane during the twin propagation. The middle column shows the atomic arrangements of resultant twins corresponding to the twinning dislocation glide, in which the open circles

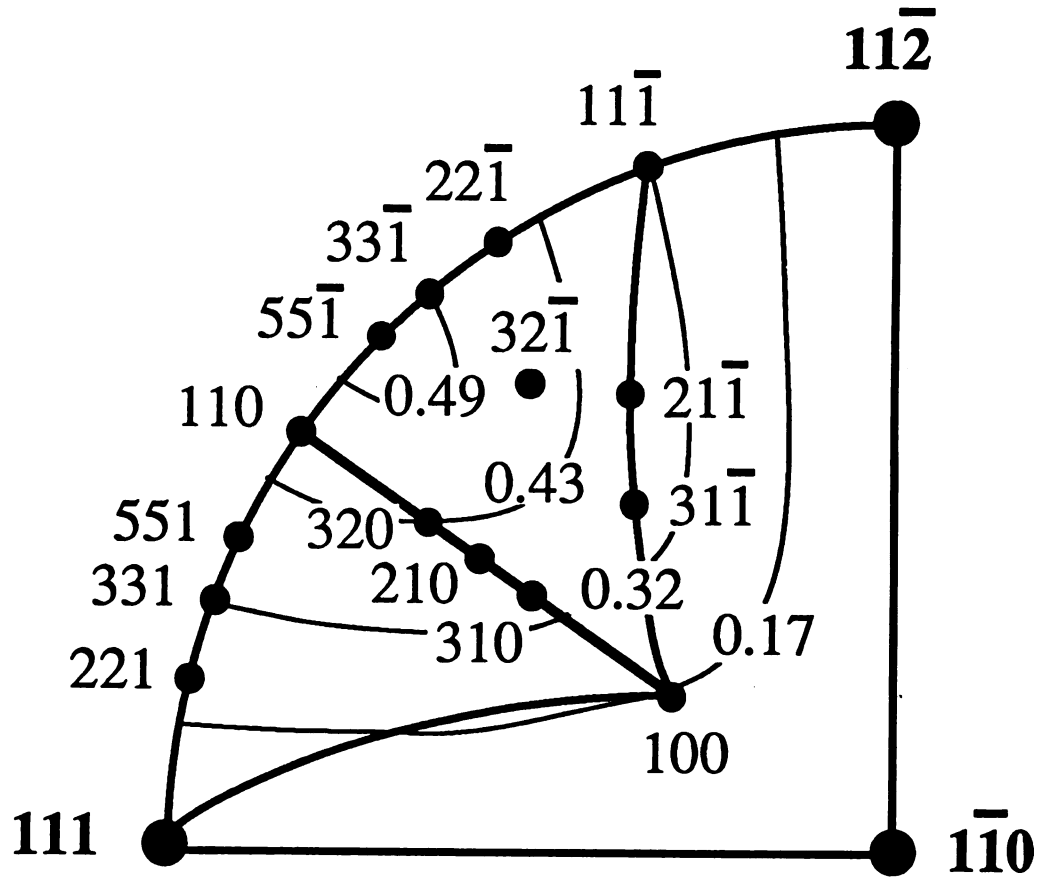


Figure 3.5 - Schmid factor contours with respect to the true-twinning system of (111)[112], which indicates that a tensile principal stress should be in the vicinity of [551] crystal direction in order to operate the (111)[112] twinning system.

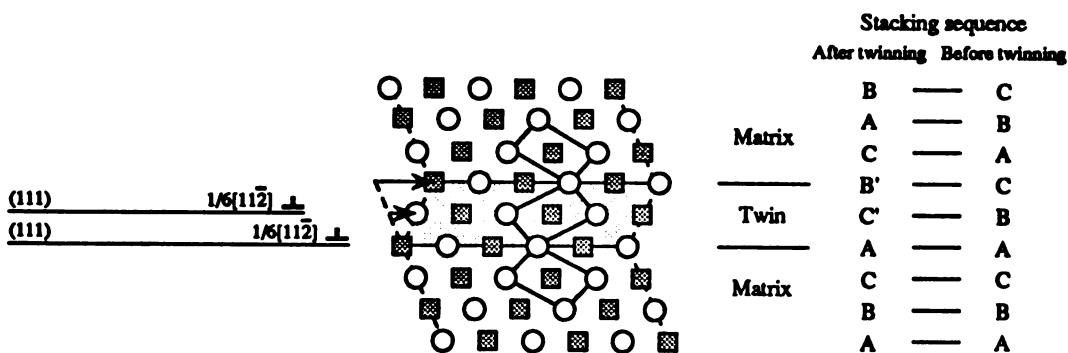
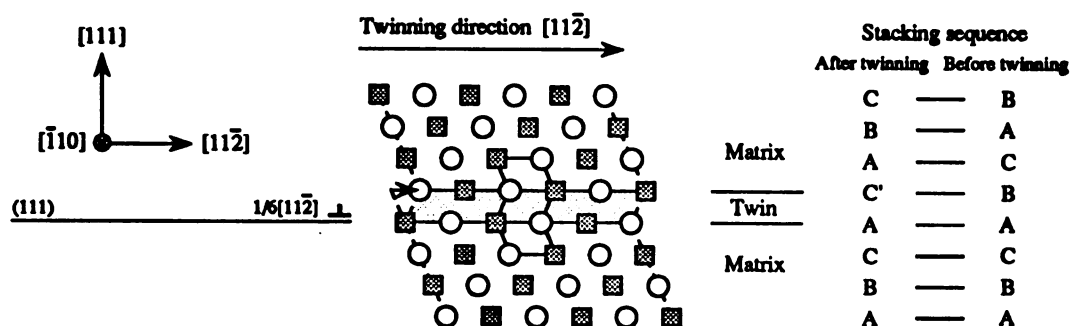
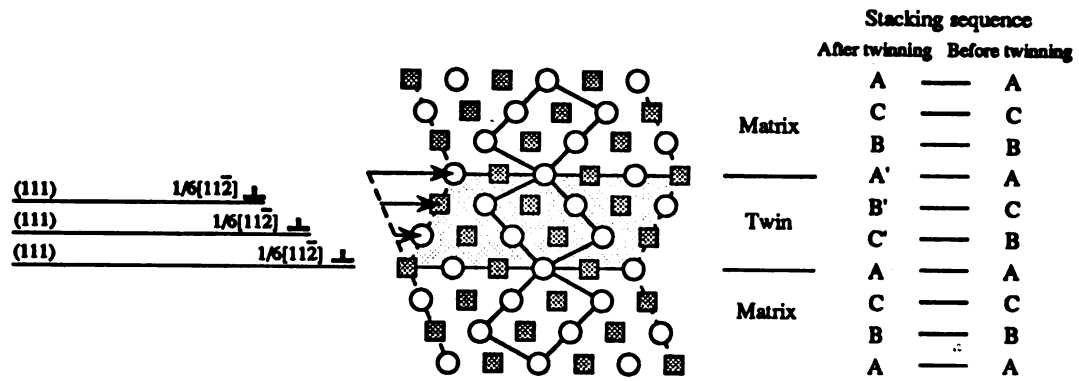
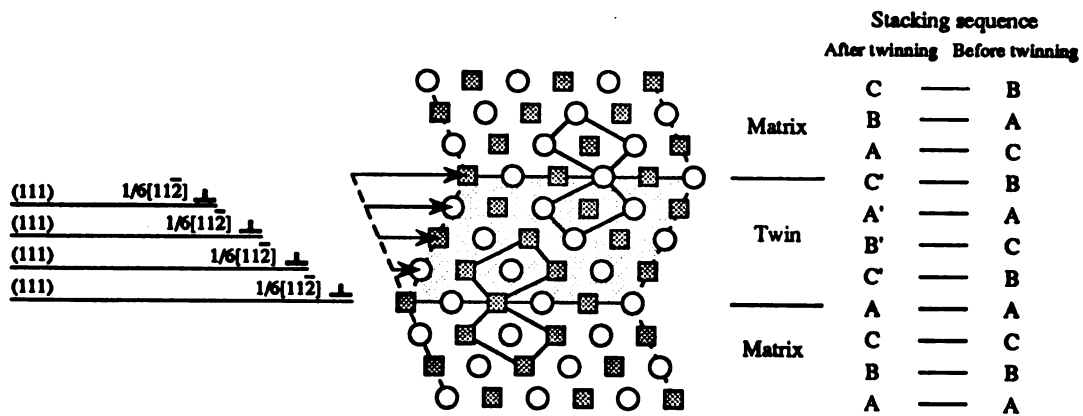


Figure 3.6 - Mechanical twin propagation mechanism in TiAl, which shows the twin layers resulting from the glide of (a) one, (b) two, (c) three, and (d) four twinning dislocations in the (111) twinning plane during the twinning propagation. The left side column is the glide sequence of $1/6[112]$ twinning dislocations. The middle column is the atomic arrangements of resultant twins viewed in $[110]$ direction, in which the open circles indicate the atoms located in the plane of the paper and the shaded squares indicate the atoms in the plane just beneath the paper. The right side column is the atomic stacking sequences along $[111]$ direction before and after twinning, in which the primed letters indicate the sheared planes.



(c)



(d)

(Figure 3.6 continued)

indicate the atoms located in the plane of the paper and the shaded squares indicate the atoms in the plane just beneath the paper. The atomic arrangements are viewed in $[\bar{1}10]$ direction. The right side column shows the atomic stacking sequences along $[111]$ direction before and after twinning, in which the primed letters indicate the sheared planes. Therefore, the glide of the first twinning dislocation (the leading twinning dislocation in Fig. 3.1) creates a twin of two atomic layers, as shown in Fig. 3.6 (a). Investigating the atomic stacking sequence change after the twinning, one can see that this two atomic layer twin actually is an intrinsic stacking fault. The glide of the two twinning dislocations in two adjacent (111) planes creates a twin with three atomic layers, see Fig. 3.6 (b), which is an extrinsic stacking fault as shown in the right side column. After the glide of the third twinning dislocation on the next adjacent (111) plane with respect to the first two twinning dislocations, a four atomic layer twin is formed, and it has no single stacking fault feature, but it does have two twin planes, see Fig. 3.6 (c). Therefore, following the second twinning dislocation, the glide of any $1/6[\bar{1}1\bar{2}]$ twinning dislocation on the (111) twinning plane does not change the features of twin interfaces but it thickens the twin with one more atomic plane, see Fig. 3.6 (c) and (d).

The thickness of the thin twin layers can be calculated based on the twin nucleation and propagation mechanism proposed above. Although the crystal structure of TiAl is anisotropic, the atomic stacking along any $\langle 111 \rangle$ directions is similar. This means that the spacings of all $\{111\}$ planes are identical. Therefore, the thin twin layer thickness can be calculated by counting the number of emitted twinning dislocations, assuming that the observed twin layers are perfect twins. For the longer twin A in Fig.

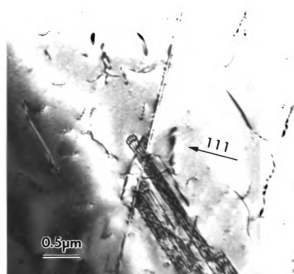
3.1 (a), the thickness is 7.2 nm, and the thickness of the shorter one **B** in Fig. 3.1 (a) is 5.8 nm. For the rest of the twins in Fig. 3.1 (a), since most twinning dislocations have already propagated farther away from the region shown in Fig. 3.1 (a), the thicknesses can not be calculated.

(b) Twin Nucleation at Twin Interfaces

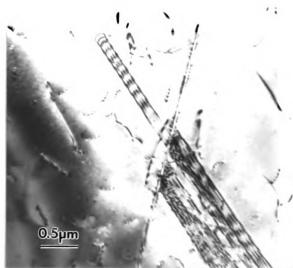
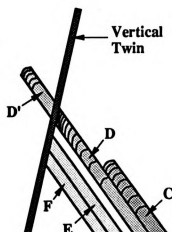
The long twin layers in Fig. 3.1 were continuously illuminated by the electron beam, and it was found that these twin layers were continuously growing into the grain interior. These growing twin layers then met an existing thin twin lath (called "vertical twin" in this case), whose twin plane was $(11\bar{1})$ plane, and crossed the vertical twin by the initiation of new twinning dislocations on the other side of the vertical twin. This is the case of twin nucleation at twin interfaces.

Fig. 3.7 shows the entire sequences of twin nucleation and propagation procedure. In Fig. 3.7, the left sides are the TEM micrographs, which were taken sequentially during the twin intersection, twinning dislocation emission and twin propagation; the right side column is a schematic illustration of twin nucleation and propagation sequence corresponding to the left side pictures. Fig. 3.8 (a) is the thin twin image taken by tilting the specimen such that the electron beam was parallel to the twin layer interfaces. The diffraction pattern taken across these thin layers is shown in Fig. 3.8 (b).

The four thin twin layers in Fig. 3.7 are denoted by **C**, **D**, **E** and **F**. The configuration shown in Fig. 3.7 (a) is the starting state of these sequential images, where



(a)



(b)

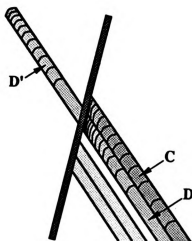
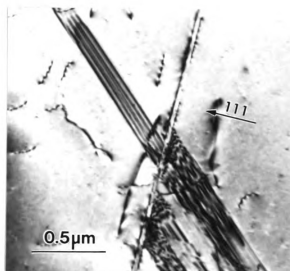
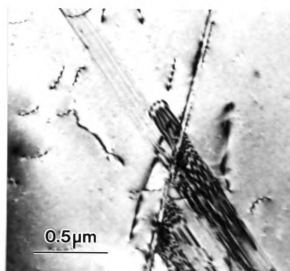
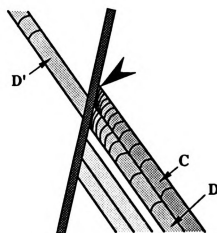


Figure 3.7 - The sequences of mechanical twin nucleation and propagation in TiAl.



(c)



(d)

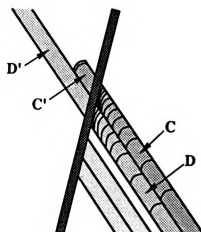
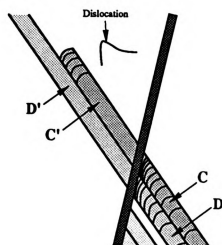
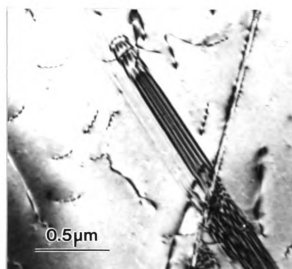
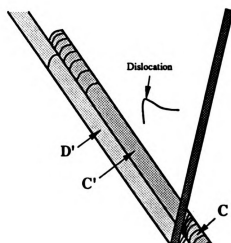
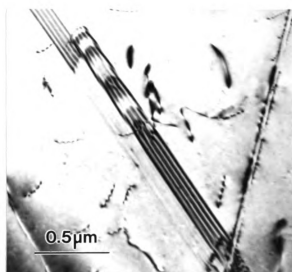


(Figure 3.7 continued)



(e)



(f)

(Figure 3.7 continued)

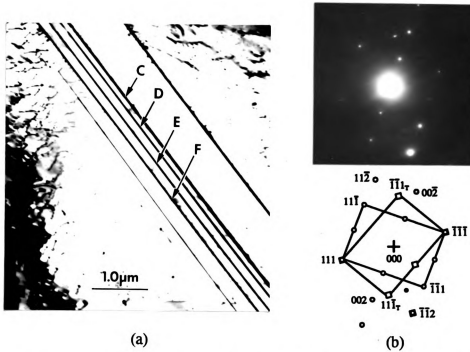


Figure 3.8 - (a) The side view of twin layers C, D, E, and F in Figure 3.7, and (b) the diffraction pattern taken across these twin layers.

the thin twin layers C, D, E and F in (a) originated from the grain boundary, which was located to the right and below the picture. At the beginning, twin C was in the intermediate state of propagation and did not reach the existing vertical twin, as shown in Fig. 3.7 (a). While twin layers E and F had intersected with the vertical twin lath, and the high density twinning dislocation pile-ups had formed within these two twin layers at the intersection, which indicates that the existing twin lath was acting as a barrier for the propagation of twins E and F. However, for twin D, in addition to the high density of twinning dislocation pile-up in the twin layer at the intersection, this twin had crossed the vertical twin lath and extended to a certain length in the other side of the vertical twin. Investigating the intersection portion within the vertical twin lath, there

is no evidence of structure and crystal orientation changes within it.

As time passed, the twin C propagated and met the vertical twin, and the twin D' further elongated, as shown in Fig. 3.7 (b). The twinning dislocations within twin C were not densely piled up at the intersection, indicating that a stress concentration at the intersection was not formed at this moment. It was found that the propagation of twin D' occurred as the twinning dislocations were emitted from the interface of vertical twin. So more dislocations can be seen in twin D' in Fig. 3.7 (b).

With the longer time, as shown in Fig. 3.7 (c), the twin D' further propagated so that the twin tip was out of this picture; more and more twinning dislocations within the twin C came and piled up against the vertical twin interface resulting in the stress concentration at the intersection as indicated by an arrow in Fig. 3.7 (c).

In Fig. 3.7 (d), the stress concentration resulting from the twinning dislocation pile-up at the intersection within the twin C was so large that the two twinning dislocations were emitted on the other side of the vertical twin lath. The sequence of these two twinning dislocation emission is as follows: Two twinning dislocations were first gradually bowing out from the interface of vertical twin, and then, after the radius of dislocation lines reached a certain value, they jumped into the matrix very quickly and propagated to a certain distance. The layer formed by the glide of these two twinning dislocations is a three atomic plane twin, as shown in Fig. 3.2 (c) and (d) and Fig. 3.6 (c), and is called the twin nucleus as mentioned in the previous section.

As more and more twinning dislocations were emitted from the vertical twin interface, this twin nucleus grew into the matrix and became a thicker twin layer. The propagation of this twin layer is clearly seen from Fig. 3.7 (e) and (f). Taking an existing dislocation line in the matrix as a reference, the relative locations of twin layer C' with respect to the reference dislocation line in Fig. 3.7 (e) and Fig. 3.7 (f) indicate that twin C' in Fig. 3.7 (e) has propagated to a longer twin layer C' as shown in Fig. 3.7 (f).

However, it was found that the twin layer could not propagate continuously until more twinning dislocations were emitted from the interface. It appeared that the trailing twinning dislocations were pushing the front twinning dislocations to move forward and this push resulted in the continuous propagation of the twin layers. Once a twinning dislocation was pushed out from the source, the twin interface at the intersection in this case, it caught up to the front dislocations very quickly compared to its bowing out period. This indicates that the twin propagation might be controlled by the twinning dislocation emission procedure, not by the twinning dislocation glide in the twinning plane. Since twin D' had extensively propagated so that the twin tip was far away from the location where the images were taken, very few twinning dislocations can be seen in twin D' in Fig. 3.7 (e) and (f).

During the investigation, the twin E and the twin F were not found to cross the vertical twin lath even though the dislocation pile-ups were seen within them at the intersections. This was probably because no more twinning dislocations were emitted

within these two twin layers from the original twinning dislocation source, i.e., the grain boundary. Therefore, the stress concentration caused by the dislocation pile-up was not large enough to transfer the twinning strain across the vertical twin lath.

(c) Twin Layer Morphology Near The Twin Tip

According to the twin nucleation and propagation procedure analyzed above, the morphology of thin twin layers shown in Fig. 3.1 and in Fig. 3.7 can be easily determined. Fig. 3.9 shows a schematic three dimensional diagram of a thin twin layer. The curved surface near the twin tip (with darker shading) is an incoherent twin boundary, which is composed of twinning dislocations lying in the boundary. On an atomic scale, this twin boundary is not a smooth interface but has a stair-like shape with the stair height equal to the interplanar spacing of twin planes. The top and bottom flat interfaces (with diagonal line shading) are coherent with the matrix, which are normal twin planes. The lower diagram in Fig. 3.9 is a side view (cross section) of the thin twin layer. Therefore, the shape of thin twin layer near the twin tip is semi-lenticular.

3.2.2. Post-Mortem Observation of Mechanical Twinning During Creep Deformation

A post-mortem investigation of a creep specimen deformed up to the end of primary creep state (the first specimen as indicated in the experimental section) indicates that fine mechanical twins nucleated at grain boundaries and propagated into the grain interior during the early stage of creep deformation in γ grains in a similar way as described in the previous section. Fig. 3.10 is an example which shows that a large

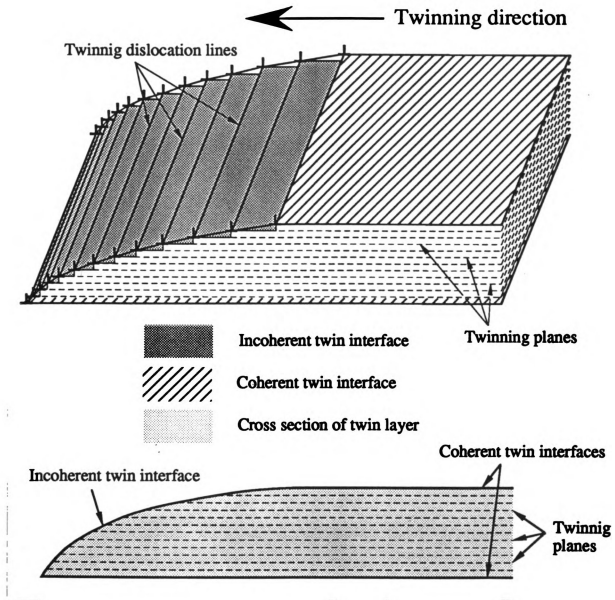


Figure 3.9 - The thin twin morphology near the twin tip.

number of fine mechanical twins were formed by the mechanism described above. In this case, the fine mechanical twins formed to accommodate the local stress concentration at a grain triple point ^[30]. Looking at the area between the fine mechanical twins and the untwinned matrix, one can easily see that some fine mechanical twins did not propagate all the way across the grain, as indicated by an arrow in Fig. 3.10. Diffraction patterns taken within the fine twin area and within the untwinned matrix region, as shown in Fig. 3.10 (b) and (d) respectively, show that the matrix within this fine mechanical twin region has the same orientation as the equiaxed γ grain within which the fine mechanical twins formed. This indicates that fine mechanical twins in Fig. 3.10 (a) are formed by deforming the γ grain.

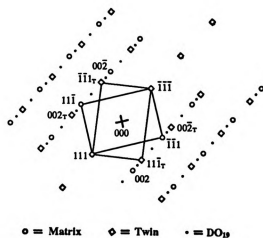
If we assume that the volume percent of twins in the fine twin region in Fig. 3.10 (a) is about 50%, the shear strain in this region is a half of the twin shear (0.707), i.e., the shear strain is equal to 0.354. The distance between two points "P" and "R" in Fig. 3.10 (a) is about 10 μm . So, the relative shear displacement of point "P" to point "R" in the direction parallel to the twin-matrix interfaces is about 3.54 μm , if we assume that all fine twins sheared in the same direction. In a similar way, by counting the number of laths between points "P" and "R" and assuming that the thicknesses of all laths are roughly equal and one half of these laths are fine twins, we calculated the thickness of a fine twin lath to be typically about 50 nm ^[30].

In the diffraction pattern shown in Fig. 3.10 (b), an extra set of diffraction spots (dots in the figure) in addition to the spots from fine twins and the matrix indicates that



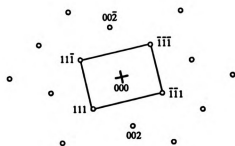
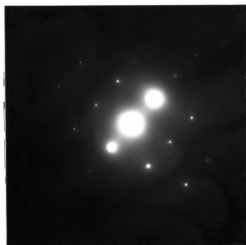
(a)

Figure 3.10 - The configuration of fine mechanical twins resulting from the accommodation of local stress concentration at a grain triple point (a). Diffraction pattern across the interfaces (b) shows that these fine laths are twin-related with matrix and the existence of fine DO_{19} phase between them (c). Diffraction pattern taken in untwinned area within the same grain without tilting the sample (d) shows that the untwinned region has the same crystal orientation as the matrix of fine mechanical twins as shown in (b). (e) is the indexes of (d). It also shows that the growth of fine mechanical twins as pointed out with an arrow between the completely developed fine twins and the matrix stopped in the grain interior.



(b)

(Figure 3.10 continued)



(c)

(Figure 3.10 continued)

there exists a third phase in this fine twin region shown in Fig. 3.10 (a). An analysis of these diffraction spots showed that these diffraction spots resulted from a DO_{19} type structure.

3.3. Discussion

3.3.1. Mechanical Twin Nucleation in TiAl

Mechanical twinning was observed to nucleate by bowing out of one (or two) $1/6[11\bar{2}]$ twinning dislocation(s) from the grain boundaries and the twin interfaces in this study. The twin nucleus can be either an intrinsic stacking fault or an extrinsic stacking fault. However, the size of twin nucleus, i.e., the distance that leading twinning dislocation propagated into the grain interior before the second twinning dislocation was emitted, was observed to vary for each twin. Since the size of electron beam used in TEM was very small, the volume illuminated by electron beam was small too. The thermal activation in the region near the leading twinning dislocation resulting from the electron beam illumination varied from place to place. In addition, the local stress state was probably not the same along the grain boundary, and it would change with the emission of twinning dislocations from the grain boundary. Therefore, both the thermal and the stress conditions at each location along the grain boundary were different. However, a certain amount of local stress with the principal stress axis in the vicinity of $[55\bar{1}]$ direction in the case of tensile stress state is necessary for the $(111)[11\bar{2}]$ twinning to nucleate.

As the twin nucleus grows, i.e., as the leading twinning dislocation propagates into the grain interior, the region of stacking fault behind the leading dislocation increases, and therefore a backward force on the leading dislocation develops in the direction opposite to its propagating direction (The detailed analysis on the backward force will be presented in the next chapter). When the twin nucleus reaches a certain size, the backward force will balance the driving force on the leading dislocation and the motion will cease. With the emission of the second dislocation, the twin propagates farther, but the second dislocation can not reach or overtake the leading dislocation since they repel each other due to the same type of $1/6[11\bar{2}]$ dislocations ^[142]. Therefore, the second dislocation appears to push the leading dislocation forward. However, since the stacking fault behind the second dislocation is the extrinsic stacking fault (see Fig. 3.3), which possesses a similar stacking fault energy to the intrinsic stacking fault, the twinning dislocations only move slightly farther into the grain. After glide of the third twinning dislocation, the interface between the twin and the matrix is a twin plane, whose interface energy is about a half of the intrinsic stacking fault energy. The backward force on the twinning dislocations following the second one is approximately one half of that on the first two twinning dislocations. Therefore, the twin propagation is easier than the nucleation.

Since the effect of a local stress concentration is limited, the local stress state could not directly provide the twinning driving force to cross the entire grain. A possible scenario for a transgranular twinning is the following: The twinning dislocations are emitted from the grain boundaries and the twin interfaces due to the local stress

concentrations and forced to move forward to the limited range within which the local stress is effective. Subsequent twinning dislocations push the front twinning dislocations beyond the local stress field. In this case, the twin propagation occurs under the continuous emission of twinning dislocations from the grain boundaries and the twin interfaces.

Since the nucleus of mechanical twin is formed by bowing out a twinning dislocation from the dislocation source, the driving force arising from the local stress concentration must be large enough to overcome another backward force resulting from the dislocation line tension. As the twinning dislocation bows out, the radius of the twinning dislocation line decreases. This results in an increase in the backward force due to the dislocation line tension. After the radius of twinning dislocation line reaches a minimum value, the radius will increase as the twin nucleus grows, that is, the backward force due to the dislocation line tension decreases with twin nucleus growth. Therefore, there should exist a maximum backward force on leading twinning dislocation corresponding to the minimum radius of twinning dislocation line during twin nucleation. In order to form a twin nucleus, the driving force resulting from local stress state must be large enough to compensate this maximum backward force besides the backward force due to the increment of stacking fault area. So, to emit twinning dislocations continuously at the grain boundaries and the twin interfaces, the local stress must maintain being larger than a certain value, the critical stress for twinning dislocation emission from the grain boundaries and the twin interfaces. If the magnitude of local stress is lower than this critical stress, according to the twin propagation mechanism

proposed in the previous section, the twin could not propagate since no more twinning dislocations would be emitted.

3.3.2. Mechanical Twinning Mechanisms in TiAl

Mechanical twinning mechanisms can be classified into three categories, that is, (1) dislocation pole mechanism ^[98,100], (2) twinning dislocation homogeneous glide mechanism ^[101,102], and (3) twin-matrix tilt boundary migration mechanism ^[103]. The main differences between them are the details in the mechanical twin nucleation and propagation. In the third model in which a twin interface is thought to be a tilt boundary, the interface dislocations glide in the planes almost normal to the twin interface. This theory assumes that once such a tilt boundary was established, it could migrate easily under a very small shear stress. However, the most intensively studied model is the dislocation pole mechanism. This mechanism describes the twinning as a result of a twinning dislocation rotating around an existing pole dislocation whose screw component is perpendicular to the twinning plane and the component Burgers vector is equal to the spacing of the planes parallel to the twinning plane ^[98,100]. Much experimental work has been done to try to validate this model. However, some experimental results indicated that mechanical twinning was found to occur by a homogeneous shear of the twinning portion of crystal with respect to the matrix ^[101,102]. This homogeneous shear mechanism requires that the individual twinning dislocations glide successively on every neighboring plane parallel to the twinning plane.

Comparing our observations with the twinning mechanisms described above, the

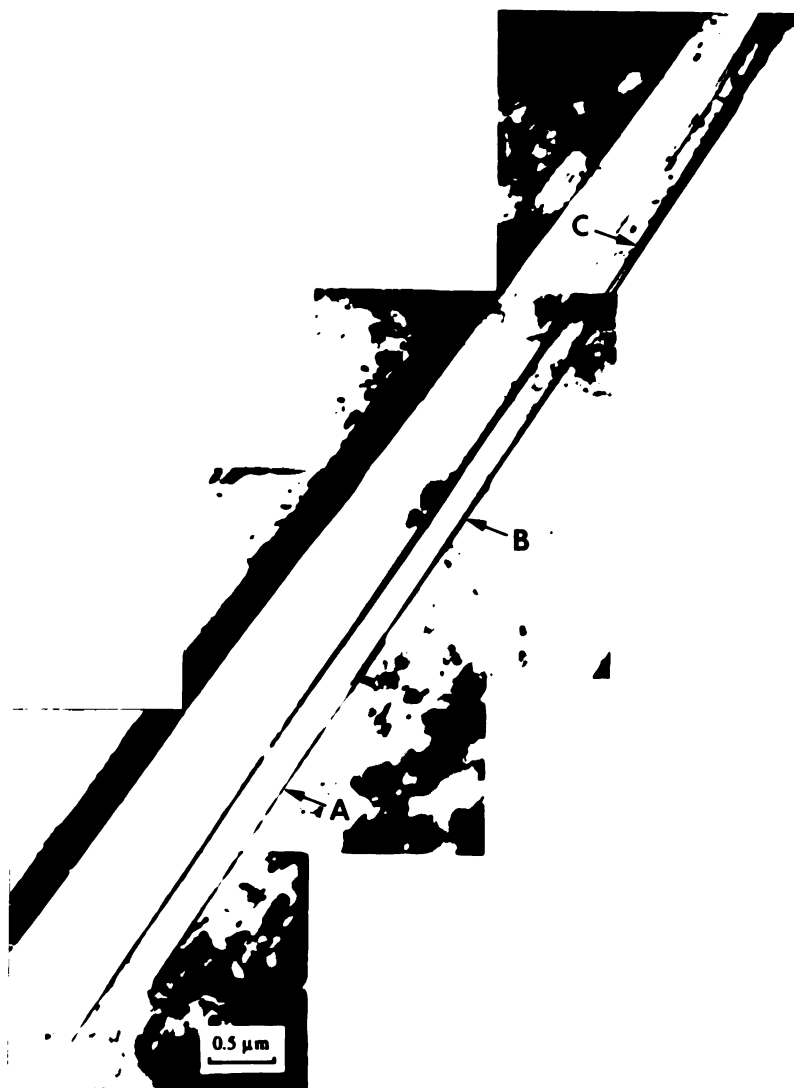
twinning in TiAl is consistent with the twinning dislocation homogeneous glide mechanism. Since the twin nuclei were formed by bowing out twinning dislocations at the grain boundaries, it was not necessary to form a dissociated dislocation jog in the twin plane. The normal dislocations and the superdislocations in TiAl are usually in the state of dissociated forms due to the relatively low stacking fault energy of this material. The more commonly dissociated configurations are such that the stacking faults are bounded by the Shockley partial dislocations, i.e., the Shockley partial dislocations are common and stable in TiAl ^[6]. Thus the emission of Shockley partial dislocations (twinning dislocations) at the grain boundaries and the twin interfaces instead of perfect dislocations (normal dislocations or superdislocations) is reasonable. It is due to the low stacking fault energy that the twin nuclei can propagate easily by the successive glide of these Shockley partial dislocations on every adjacent plane.

However, a recent study by Farenc, Coujou and Couret ^[32] indicates that a dislocation pole mechanism was observed *in situ* in a TiAl specimen deformed at room temperature in tension. These authors identified the twinning dislocations by characterizing the stacking fault fringe configurations in the tilted twin images. The twin propagation procedure is the same as the one observed in our study, but the twinning dislocation source is within the grain interior and the twinning proceeds by the rotation of an $a/6 \langle 112 \rangle$ type partial dislocation around a perfect dislocation. In our study on a large strain specimen, which was deformed up to a tertiary state of creep deformation, an evidence of twin nucleation within the grain interior was also found, as shown in Fig. 3.11. Three individual thin twin layers, indicated by letters "A", "B" and "C", can be

seen in Fig. 3.11. These twin layers are completely within a γ grain interior. So the nuclei of these twin layers were formed inside the γ grain. The source of twinning dislocations might be some defects in the grain. Because no inclusions and second phases were found near the twin layers, the possible source of twinning dislocations might be the dislocation jogs. Thus, the twin layers probably propagated by the dislocation pole mechanism.

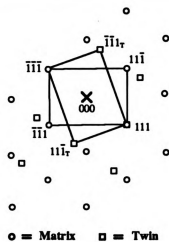
Therefore, the mechanical twinning mechanism in TiAl may depend on the location of twin nucleation and the amount of strain. Since the large strain creates more dislocations within the γ grains, the possibility of formation of dislocation jogs and pole dislocations within the γ grains increases with increasing strain. So the dislocation pole mechanism is reasonable at large strain. If the twin nuclei are formed at grain boundaries, the twinning dislocation homogeneous glide mechanism is preferred, but in the case that the twin nuclei are formed in the grain interior, the dislocation pole mechanism is more probable.

It must be noted that the image of dissociated perfect dislocations in a tilted microslip band is similar to that of the fine mechanical twins since the perfect dislocations in TiAl easily dissociate into the partial dislocations with the stacking faults between the partials. Therefore, it is necessary to identify whether the observed images are fine mechanical twin layers or microslip bands before further analysis. A diffraction pattern analysis is necessary to make this distinction.



(a)

Figure 3.11 - (a) shows three thin twin layers indicated by letters "A", "B" and "C" within a γ grain interior, which indicates that the nuclei of these twin layers were formed inside the γ grain; (b) is a diffraction pattern taken across the twin layers.



(b)

(Figure 3.11 continued)

3.3.3. On The DO_{19} Phase in Fine Mechanical Twins

The diffraction pattern in Fig. 3.10 (b) indicates that fine mechanical twin region at grain triple point as shown in Fig. 3.10 (a) consists of three different layers: the matrix, the fine twins and the DO_{19} structural phase. The formation of fine mechanical twins has been analyzed in previous section. But the formation of DO_{19} layers accompanying the twinning is not clear. No experimental results clearly show how the DO_{19} layers form. Therefore, in the following, some possibilities of DO_{19} diffraction spots are discussed. (a) If the stress concentration at the grain triple points and/or grain boundaries is such that it does not emit $1/6 \langle 11\bar{2} \rangle$ twinning dislocations on every (111) plane, four atomic layers of DO_{19} structure, i.e., a nucleus of the Ti_3Al crystal structure, will be formed by glide of a single $1/6 \langle 11\bar{2} \rangle$ twinning dislocation on a (111) plane ^[143]. So, in the case that a large volume of γ crystal is deformed by the heterogenous glide of $1/6[11\bar{2}]$ partial dislocations, the diffraction spots resulting from the nuclei of DO_{19} crystal structure may be visible. (b) The crystal structure across a true-twin plane in TiAl is also a three atomic layer DO_{19} structure, see Fig. 3.6 (d). If one uses a large size of aperture in selecting area diffraction, the total volume of DO_{19} layers in the fine twin region will be large, and therefore, its contribution to DO_{19} diffraction spots is also considerable.

It is worth noting that such a uniformly distributed thin lath configuration in Fig. 3.10 (a) is unlikely to be formed by phase transformations such as $\alpha_2 \rightarrow \alpha_2 + \gamma$ and $\alpha \rightarrow \alpha_2 + \gamma$ due to its large interfacial energy. Such a thin γ phase layer could not be thermodynamically stable during a phase transformation. Therefore, the thin γ phase

layer should either grow and become thicker or be eliminated by the growth of adjacent γ laths. The resultant configuration in the case of phase transformation should be the lamellae containing coarse γ laths with different thickness. The observation of fine twin configurations only near the equiaxed γ grain triple points in this study also provides an evidence that the fine mechanical twins are formed due to the local stress concentration at the equiaxed γ grain triple points but not by the phase transformation. In addition, the composition of the γ phase is the same at the creep test temperature, 760 °C, as at a higher phase transformation temperature, so the chemical driving force to decompose γ phase is zero.

3.3.4. Twin Morphology

Twin morphology has long been described as either a lenticular shape or an elliptic shape, particularly when modelling the mechanical properties, such as elastic strain energy and stress field, of twins ^[113,144,145]. There are two methods that have been generally used to predict twin shapes: one is based on the twinning energy calculation, and the other is based on the elastic forces acting on individual twinning dislocations. Both methods assumed that a twin has a symmetric shape so that the lenticular or elliptic shape was predicted. However, the thin twin layers observed in this study do not have a symmetric shape but a semi-lenticular shape near the twin tip, as shown in Fig. 3.9. Since the energy of the flat coherent twin plane is lower than that of the curved incoherent twin boundary and the strain energy resulting from the twinning shear can be neglected for very thin twin layer ^[113], the semi-lenticular twin shape may be energetically more stable than the fully elliptic twin shape.

Based on the traditional symmetric twin morphology, Marcinkowski and Sree Harsha ^[117] first calculated the twinning dislocation distributions in incoherent twin boundaries and the stress distribution surrounding the twin tip by considering the elastic forces acting on the twinning dislocations. The result shows that the twinning dislocations close to the twin tip are distributed more densely than those away from the tip. This trend of dislocation distribution is consistent with the observations in this study as shown in Fig. 3.1 and Fig. 3.7. But the twinning dislocations in the upper and the lower incoherent twin boundaries of a symmetric twin layer tend to be vertically aligned one to another ^[117]. If this were true in this study, the overlapped stacking fault fringe images and the coupled twinning dislocation lines would be seen. But the twin layer images observed in this study show only one set of periodically changed stacking fault fringes and the single dislocation lines. This indicates that the twin layers observed in this study are thickened by the glide of twinning dislocations on only one side of the twin layer and the shape near the twin tip is semi-lenticular.

3.4. Summary

The following summary can be made concerning the mechanical twin nucleation and propagation in investment cast near gamma TiAl (Ti-48Al-2Nb-2Cr) specimens creep deformed at 765 °C.

1. Mechanical twin is nucleated by the bowing out of twinning dislocations at the grain boundaries and the twin interfaces due to the local stress concentration. The

nucleus for true-twinning observed in this study is either a superlattice intrinsic stacking fault (SISF) or a superlattice extrinsic stacking fault (SESF). The superlattice intrinsic stacking fault is formed by bowing out one $1/6[11\bar{2}]$ twinning dislocation from the grain boundaries or the twin interfaces. The superlattice extrinsic stacking fault is formed by emission of two $1/6[11\bar{2}]$ twinning dislocations from the grain boundaries or the twin interfaces on adjacent (111) planes.

2. The mechanical twin propagation mechanism in TiAl observed in this study is a homogeneous glide of twinning dislocations on every adjacent twinning plane.

3. Mechanical twin propagation mechanisms in TiAl depend on the locations of twin nucleation. If a twin nucleates at the grain boundary, it propagates by the twinning dislocation homogeneous glide mechanism. However, if a twin nucleates within a γ grain interior, the twin propagation is controlled by the dislocation pole mechanism.

4. The locations of twin nucleation seem to be affected by strain. In low strain creep specimen (4 %) investigated, we found that all fine mechanical twins resulting from the accommodation of stress concentration at grain triple points initiated at grain boundaries. But in a large strain creep specimen, twins originating in the grain interior were observed.

5. The reason of occurrence of DO_{19} diffraction spots is not clear at present. It seems to be the result of the heterogenous glide of $1/6[11\bar{2}]$ partial dislocations and the

existence of three layers of DO_{19} structure at each true-twin interface. Further work is needed to test these hypotheses.

6. The thin twin morphology near the twin tip observed in this study has a semi-lenticular shape rather than a lenticular or an elliptic shape.

CHAPTER FOUR

FORCE AND STRESS ANALYSES ON TWIN PROPAGATION

The stress required for mechanical twin propagation is supposed to be such that the driving force for mechanical twin propagation must be equal to or larger than the backward force (F_b) on the twinning dislocations. This backward force acts on the twinning dislocations in an opposite direction to the twinning dislocation moving direction, i.e., the twin propagation direction. At an equilibrium condition, i.e., at a constant propagation rate, the backward force is equal to the driving force on each twinning dislocation. Thus, the stress necessary for mechanical twin propagation must be such that the driving force on the twinning dislocations at least equals the backward force on the same twinning dislocations.

Because the twinning dislocations are the same type of $1/6[11\bar{2}]$ Shockley partial dislocations (see section 3.2.1), a repulsive force exists between the twinning dislocations. This repulsive interaction force results in a separation between the twinning dislocations. But, the stress imposed on a twin layer results in a reduction in spacing between twinning dislocations. So, we can obtain the stress distribution along a twin layer by calculating the forces on the twinning dislocations in the twin layer.

4.1. Theory

4.1.1. Forces on Each Twinning Dislocation

Before the forces on each twinning dislocation are computed, the forces acting on each twinning dislocation in a twin layer are identified. The incoherent twin boundary structure shown in Fig. 3.3 is used for the force analysis. On the first (the leading) twinning dislocation, four forces are identified, as shown in Fig. 4.1 (a):

- (i) the forward dislocation interaction force, $F_{f.d.}$, which results from the repulsive force of the twinning dislocations behind the leading dislocation;
- (ii) the applied force, F_a , (or external force F_{ex} as defined later), which results from the externally applied stress, the local stress state (including residual stress), and is in the same direction as the twinning propagation direction;
- (iii) the internal friction force, F_{fric} , which always acts in the opposite direction to the twin propagation direction;
- (iv) the force due to the superlattice intrinsic stacking fault behind the leading twinning dislocation, F_{SISF} , which pulls the leading twinning dislocation backward.

On the second twinning dislocation, six forces are identified, as shown in Fig. 4.1

(b):

- (i) the forward dislocation interaction force, $F_{f.d.}$, which is due to the dislocations behind the second twinning dislocation within the twin layer;
- (ii) the applied force, F_a ;

- (iii) the force due to the superlattice intrinsic stacking fault, F_{SISF} , which pulls the second twinning dislocation forward;
- (iv) the backward dislocation interaction force, $F_{\text{b.d.}}$, due to the leading twinning dislocation;
- (v) the internal friction force, F_{fric} .
- (vi) the force due to the superlattice extrinsic stacking fault, F_{SESF} , which pulls the second twinning dislocation backward.

On the third twinning dislocation, six forces are identified, as shown in Fig. 4.1

(c).

- (i) the forward dislocation interaction force $F_{\text{f.d.}}$;
- (ii) the applied force F_{a} ;
- (iii) the force due to superlattice extrinsic stacking fault, F_{SESF} , which pulls the third dislocation forward;
- (iv) the backward dislocation interaction force, $F_{\text{b.d.}}$, due to the first two twinning dislocations;
- (v) the internal friction force, F_{fric} ;
- (vi) the force due to the twinning plane surface tension, $F_{\text{t.p.}}$, which pulls the third twinning dislocation backward.

On the fourth twinning dislocation, the forces F_{a} , $F_{\text{f.d.}}$, F_{fric} and $F_{\text{b.d.}}$ are similar to those defined for the third dislocation, but there are no stacking fault forces on this dislocation. Forward and backward $F_{\text{t.p.}}$ forces exist on the fourth twinning dislocation,

as shown in Fig. 4.1 (d). However, since they are the same type of forces acting in the opposite direction, the net force from them is assumed to be zero, so they can be eliminated during the force calculation.

On the rest of the twinning dislocations, the forces on each twinning dislocation are exactly the same as those on the fourth one.

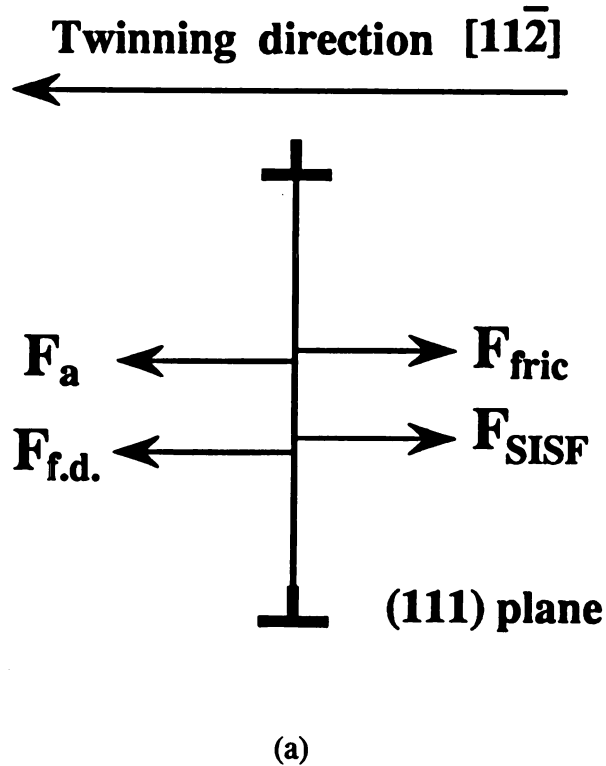
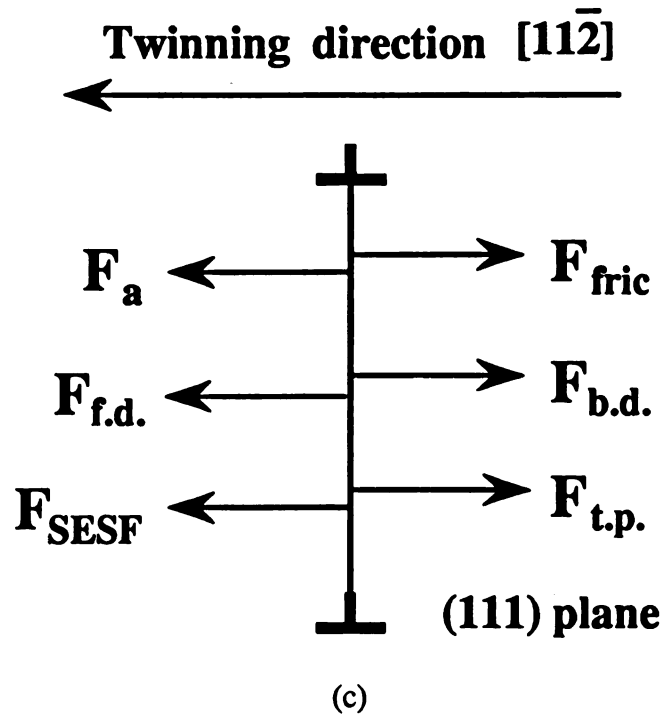
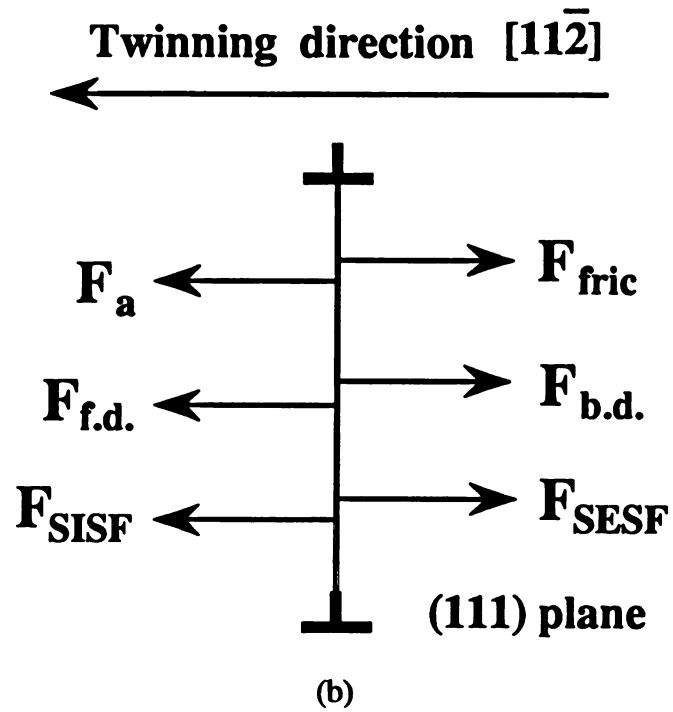
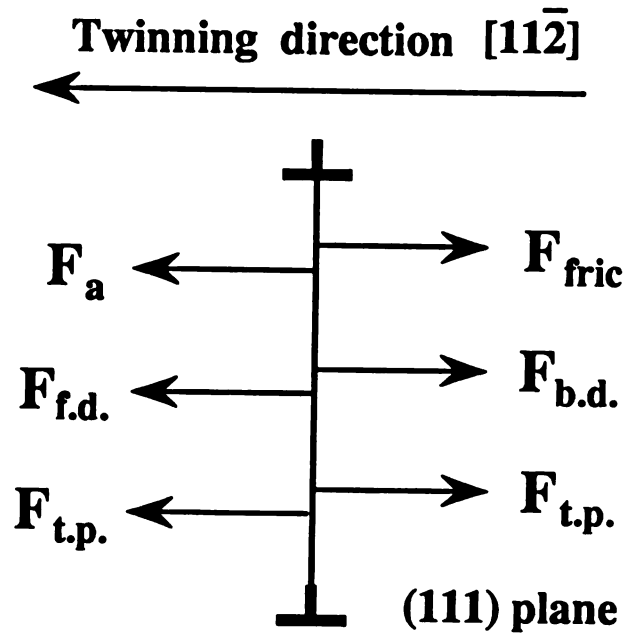


Figure 4.1 - Forces on each twinning dislocation in the thin twin layer. (a) On the first twinning dislocation, (b) on the second one, (c) on the third, and (d) on the fourth.



(Figure 4.1 continued)



(Figure 4.1 continued).

4.1.2. Dislocation Interaction Forces

Since all the twinning dislocations within the twin layer shown in Fig. 3.1 are the same type of dislocations, i.e., they are all the Shockley partials of $1/6\langle 11\bar{2} \rangle$, the interaction force between any two twinning dislocations is repulsive. If we calculate the interaction force resulting from dislocations located in front of a specific dislocation, the result will be the backward dislocation interaction force ($F_{b.d.}$). Similarly, the force calculated from the dislocations behind a specific dislocation is the forward dislocation interaction force ($F_{f.d.}$).

Since the distance between two neighboring twinning dislocations near the twin tip are small compared to their lengths as shown in Fig. 3.1, the twinning dislocations are considered as parallel dislocations, and the dislocation end effects can be neglected. Therefore, the repulsive interaction force between two twinning dislocations can be expressed as

$$F_d = \frac{G}{2\pi(1-\nu)R} [b_1 \times \zeta] \cdot [b_2 \times \zeta] + \frac{G}{2\pi R} [(b_1 \cdot \zeta)(b_2 \cdot \zeta)] \quad (4.1)$$

where F_d is a twinning dislocation interaction force between two dislocations per unit length in the direction perpendicular to the dislocation line,

b_1 and b_2 are Burgers vectors of two twinning dislocations,

ζ is a dislocation line direction,

R is a distance between two dislocations,

G is the shear modulus,

ν is Poison's ratio.

The first term in the right hand side is due to the edge component of the dislocations, and the second term is due to the screw components.

Since $F_{f,d}$ and $F_{b,d}$ are the forces referring to the interactions of a specific dislocation with many other twinning dislocations behind and ahead of it in the twin layer, respectively, $F_{f,d}$ and $F_{b,d}$ should be the summations of all F_d 's for the twinning dislocations behind the dislocation considered and of those ahead of it, respectively.

Using a cartesian orthogonal coordinates as shown in Fig. 3.3 and considering the general situation based upon mixed dislocations, the forward dislocation interaction force $F_{f.d.}$ for the m th twinning dislocation is expressed as follows,

$$\begin{aligned} \frac{F_{f.d.}}{Gb} = & \sum_{i=m+1}^n \frac{b \sin^2 \alpha}{2\pi(1-\nu)} \frac{(x_i - x_m) * [(x_i - x_m)^2 - (d_{t.p.} * (i-m))^2]}{[(x_i - x_m)^2 + (d_{t.p.} * (i-m))^2]^2} \\ & + \sum_{i=m+1}^n \frac{b \cos^2 \alpha}{2\pi} \frac{(x_i - x_m)}{(x_i - x_m)^2 + [d_{t.p.} * (i-m)]^2}. \end{aligned} \quad (4.2)$$

where, α is the angle between the Burgers vector and the dislocation line,

$d_{t.p.}$ is the interplanar spacing of the twinning plane,

x_m is the location of the m th twinning dislocation,

x_i is the location of the i th twinning dislocation that is behind the m th twinning dislocation,

and the forward dislocation interaction force $F_{f.d.}$ is normalized with Gb so that $F_{f.d.}/Gb$ is dimensionless.

For the backward dislocation interaction force $F_{b.d.}$, we can get a similar expression, but only difference is that the dislocations ahead of the m th dislocation should be considered in this case:

$$\begin{aligned} \frac{F_{b.d.}}{Gb} = & \sum_{i=1}^{m-1} \frac{b \sin^2 \alpha}{2\pi(1-\nu)} \frac{(x_m - x_i) * [(x_m - x_i)^2 - (d_{t.p.} * (m-i))^2]}{[(x_m - x_i)^2 + (d_{t.p.} * (m-i))^2]^2} \\ & + \sum_{i=1}^{m-1} \frac{b \cos^2 \alpha}{2\pi} \frac{(x_m - x_i)}{(x_m - x_i)^2 + [d_{t.p.} * (m-i)]^2} . \end{aligned} \quad (4.3)$$

4.1.3. Internal Friction Force

For the internal friction force, we consider only a lattice friction force that is due to the Peierls (or Peierls-Nabarro) stress, σ_p , on the twinning dislocations. The stress necessary for a dislocation to pass from one Peierls potential valley to the next has been calculated by Peierls ^[146] and Nabarro ^[147] as

$$\sigma = \sigma_p \sin(2\pi u/a) \quad (4.4)$$

where σ_p is the Peierls stress,

u is the displacement of a dislocation perpendicular to itself,

a is the distance between one close-packed atomic row and the next.

The Peierls stress is directly related to the Peierls energy, as shown in Fig. 4.2, and it is expressed as

$$\sigma_p = \frac{2W_p}{ab} = \frac{2G}{(1-\nu)} \exp\left(-\frac{4\pi\zeta}{b}\right) . \quad (4.5)$$

where W_p = the Peierls energy,

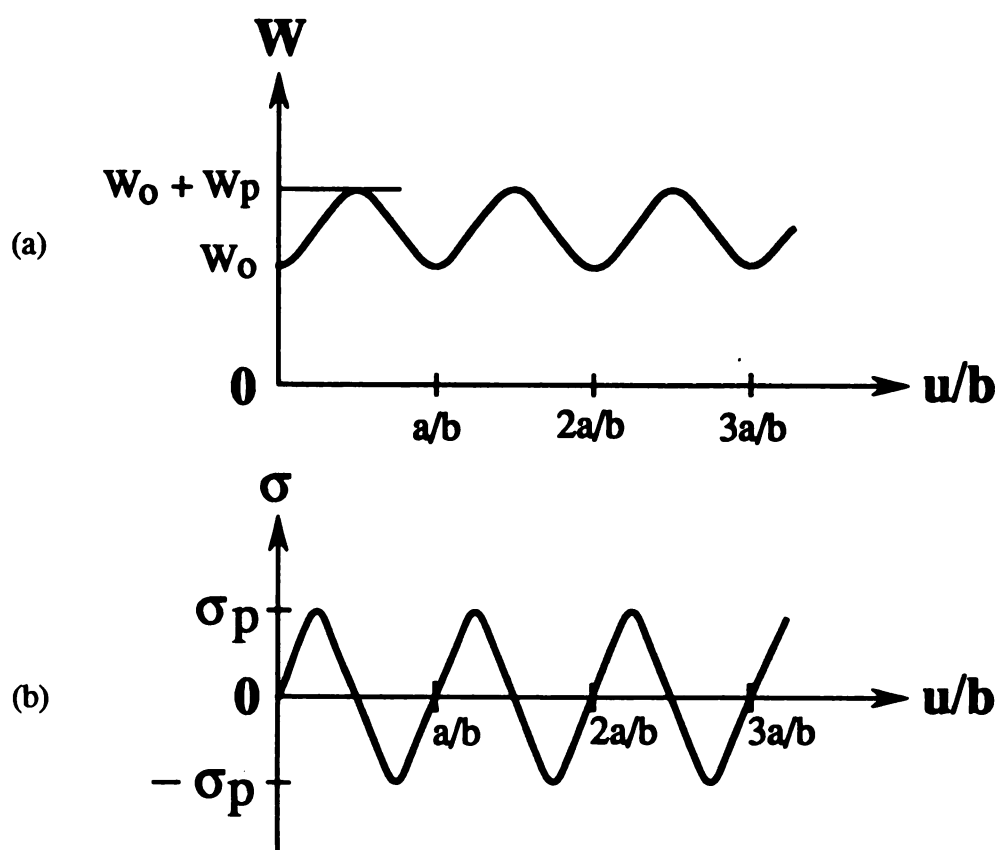


Figure 4.2 - (a) Variation of Peierls energy as a function of transverse displacement (u), (b) Variation of the lattice friction stress. ($W_0 \approx Gb^2$). (After Fantozzi, Esnouf, Benoit and Ritchie ^[148]).

ζ = the half-width of the dislocation characterizing its degree of delocalization,
 $\zeta = d / [2(1-\nu)]$ for an edge dislocation, and $\zeta = d / 2$ for a screw dislocation,
 d = the spacing of the glide plane.

According to the above equation for the Peierls stress, it can be concluded that the Peierls stress for a partial dislocation is much smaller than that for a perfect dislocation because the Burgers vector effect on the Peierls stress is in the negative exponential ^[148,149].

The internal friction force F_{fric} on a dislocation per unit length then can be calculated in a normalized form

$$\frac{F_{fric.}}{Gb} = \frac{2}{(1-\nu)} \sin(2\pi u/a) \exp\left(-\frac{4\pi\zeta}{b}\right). \quad (4.7)$$

4.1.4. The Force Due to The Stacking Faults

The forces due to the stacking faults, such as F_{SISF} , F_{SESF} and $F_{t.p.}$, are all numerically equal to the corresponding stacking fault energies, γ_{SISF} , γ_{SESF} and $\gamma_{t.p.}$, respectively. Since the intrinsic stacking fault energy is approximately equal to the extrinsic stacking fault ^[150,151], we have

$$F_{SISF} \approx F_{SESF}. \quad (4.8)$$

For the force $F_{t.p.}$ exerted by the twinning plane surface tension, since the twinning plane energy is about one half of the stacking fault energy ^[151,152], it is numerically equal to one half of the magnitude of the force resulting from the stacking fault (F_{SISF} or F_{SESF}):

$$F_{t.p.} = 1/2 F_{SISF} = 1/2 F_{SESF}. \quad (4.9)$$

4.1.5. Applied Force

The applied force is expressed as the following:

$$F_a = \sigma_a (m_e * b_e + m_s * b_s) \quad (4.10)$$

or

$$F_a = \sigma_a b (\cos \alpha * \cos \beta * \cos \gamma + \cos \alpha * \cos \gamma * \cos \theta) \quad (4.11)$$

where σ_a = the externally applied stress,

m_e = the Schmid factor for edge dislocation component,

m_s = the Schmid factor for screw dislocation component,

b_e = the edge component of the twinning dislocation,

b_s = the screw component of the twinning dislocation,

α = the acute angle between the Burgers vector and the dislocation line,

β = the angle between the applied tensile axis and the direction of b_e ,

γ = the angle between the applied tensile axis and the twinning plane normal,

θ = the angle between the applied tensile axis and the direction of b_s .

Thus in the case of an equilibrium condition, since the net total force imposed on a twinning dislocation is zero, the following equation is established:

$$\mathbf{F}_a + \mathbf{F}_{f.d.} + \mathbf{F}_{fric.} + \mathbf{F}_{b.d.} + \mathbf{F}_{SISF} + \mathbf{F}_{SESF} + \mathbf{F}_{t.p.} = 0 \quad (4.12)$$

4.1.6. Definitions of External Force, Forward Force and Backward Force

For the analysis convenience, we define some new forces in terms of their acting directions and sources. At first, we define the force resulting from the externally applied stress, the locally concentrated stress and the residual stress as an external force, \mathbf{F}_{ex} . Here, we assume that all these external stresses result in forces acting on a twinning dislocation in the same direction as the twin propagation direction, so that the external force, \mathbf{F}_{ex} , is always parallel to the twin propagation direction in this analysis. Secondly, we define the sum of forces acting in the twin propagation direction, except for the external force, as a internal forward force or simply a forward force, \mathbf{F}_f . Finally, we define the sum of forces acting in the opposite direction to the twin propagation direction as an internal backward force or simply a backward force, \mathbf{F}_b . The terminology "internal force" means that this force is an intrinsic character of a twin, in other words, the internal force coexists with the twin, i.e., no twin then no internal force. While the external force is different, whether a twin exists or not, this force still exists in the matrix.

Thus we have the following equations for each twinning dislocation according to the previous analysis. For the first dislocation,

$$\mathbf{F}_{\text{ex}} = \mathbf{F}_a, \quad (4.13)$$

$$\mathbf{F}_f = \mathbf{F}_{f.d.}, \quad (4.14)$$

$$\mathbf{F}_b = \mathbf{F}_{\text{fric.}} + \mathbf{F}_{\text{SISF}}. \quad (4.15)$$

For the second dislocation,

$$\mathbf{F}_{\text{ex}} = \mathbf{F}_a, \quad (4.16)$$

$$\mathbf{F}_f = \mathbf{F}_{f.d.} + \mathbf{F}_{\text{SISF}}, \quad (4.17)$$

$$\mathbf{F}_b = \mathbf{F}_{b.d.} + \mathbf{F}_{\text{SESF}} + \mathbf{F}_{\text{fric.}}. \quad (4.18)$$

For the third dislocation,

$$\mathbf{F}_{\text{ex}} = \mathbf{F}_a, \quad (4.19)$$

$$\mathbf{F}_f = \mathbf{F}_{f.d.} + \mathbf{F}_{\text{SESF}}, \quad (4.20)$$

$$\mathbf{F}_b = \mathbf{F}_{b.d.} + \mathbf{F}_{t.p.} + \mathbf{F}_{\text{fric.}}. \quad (4.21)$$

For the dislocations beyond the third one,

$$\mathbf{F}_{\text{ex}} = \mathbf{F}_a, \quad (4.22)$$

$$\mathbf{F}_f = \mathbf{F}_{f.d.} + \mathbf{F}_{t.p.}, \quad (4.23)$$

$$\mathbf{F}_b = \mathbf{F}_{b.d.} + \mathbf{F}_{t.p.} + \mathbf{F}_{\text{fric.}}. \quad (4.24)$$

In what follows, we will calculate all these three forces, \mathbf{F}_f , \mathbf{F}_b and \mathbf{F}_{ex} , within twin A of Fig. 3.1 (a).

4.2. Twinning Dislocation Distribution Within A Thin Twin Layer

Let us take a thin twin layer A in Fig. 3.1 as an example to see how the twinning dislocations are distributed within the thin twin layer. For the determination of twinning

dislocation position, the image of this thin twin layer is further amplified to a magnitude of 120,000X, as shown in Fig. 4.3 (a) and it is schematically illustrated in Fig. 4.3 (b). The twinning dislocations in this twin layer are labeled using numbers as shown in Fig. 4.3 (b).

The distances of these twinning dislocations from the leading twinning dislocation are measured and the results are listed in table 4.1. For the second twinning dislocation, the distance was determined by taking the one-third of the distance of the third twinning dislocation that was directly measured from the image, since the exact location of the second dislocation line was hard to be determined from the image. This estimation will be evaluated in section 4.6.1. The distances of twinning dislocations from the leading twinning dislocation were measured up to the sixteenth dislocation. Since the seventeenth dislocation is blocked by an extrinsic dislocation as shown in Fig. 4.3 (b), the distance of the dislocations beyond the sixteenth are not simply related to the forces analyzed before, and a force due to the dislocation reaction between the seventeenth and the extrinsic dislocations should be considered for the seventeenth dislocation. This effect can be seen in Fig. 4.3 (a) in which the spacings between the twinning dislocations behind the seventeenth are less than those just ahead of it due to the extrinsic dislocation blocking. So the extrapolated positions of dislocations beyond the sixteenth are considered when calculating the forward forces on the dislocations from 11 to 16.

The directly measured dislocation locations vs. the dislocation number is plotted in Fig. 4.4, and the data fit the following equation,

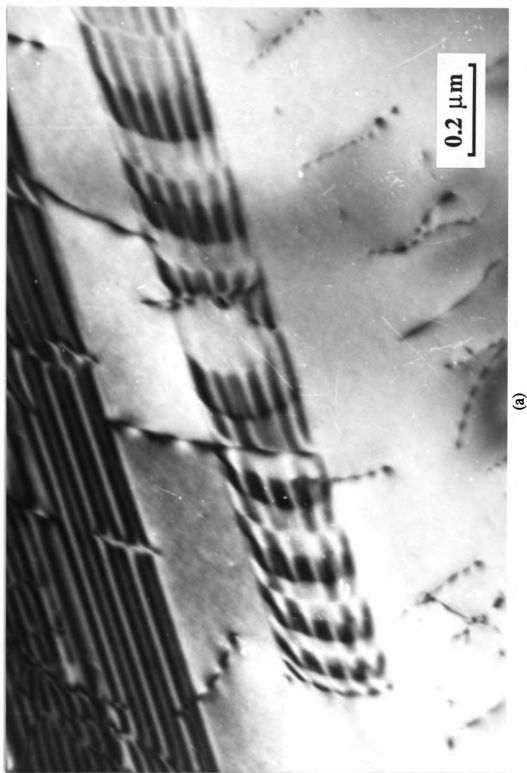
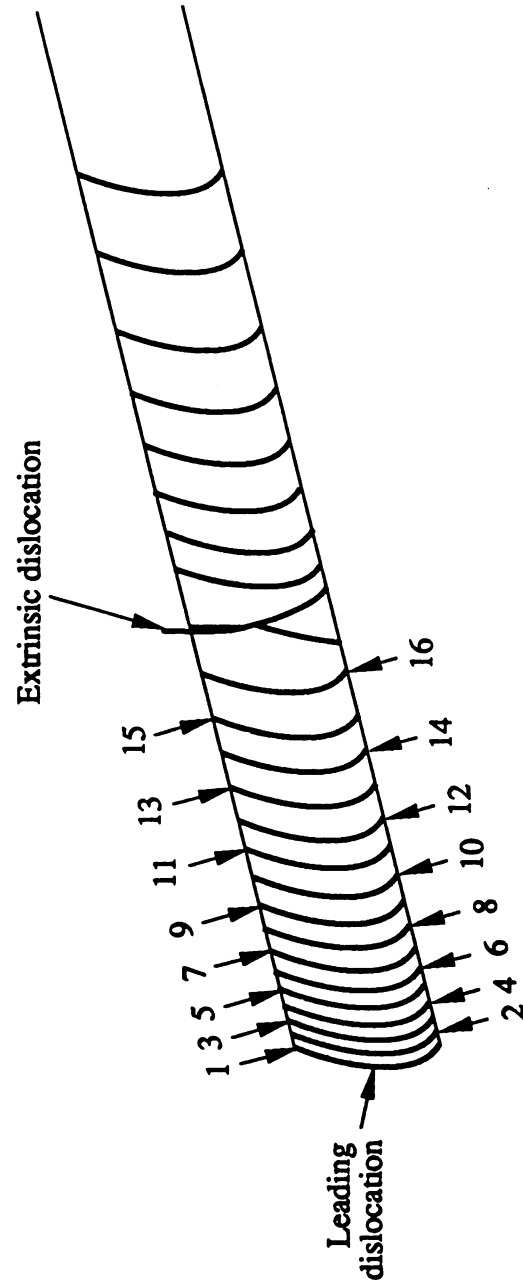


Figure 4.3 - (a) is the amplified image of a thin twin layer and (b) is a schematic drawing of the twinning dislocation distribution in the thin twin layer.



(b)

(Figure 4.3 continued)

Table 4.1. The distance of twinning dislocations from the twin tip

Dislocation	Distance (Å)	Dislocation	Distance (Å)
1	0	12	2803
2	48	13	3247
3	145	14	3787
4	290	15	4333
5	480	16	5167
6	694	17	6000
7	916	18	7000
8	1249	19	8200
9	1582	20	9600
10	1915	21	11400
11	2359		

$$x_i = 163.04 - 179.69 * i + 66.71 * i^2 - 4.47 * i^3 + 0.14 * i^4. \quad (4.25)$$

where x_i = the distance of the i th dislocation from the twin tip,

i = the dislocation number.

Thus the extrapolated positions of the dislocations beyond the sixteenth dislocation are obtained by extrapolating the plot in Fig. 4.4. The extrapolated distances of the dislocations beyond the sixteenth are also listed in table 4.1.

4.3. Force Calculation

4.3.1. Calculation of Forward Force F_f

According to the previous analysis, the forward force on each twinning dislocation can be expressed as follows.

On the leading twinning dislocation,

$$\begin{aligned} \frac{F_{f,1}}{Gb} = \frac{F_{f,d}}{Gb} = \frac{b \sin^2 \alpha}{2\pi(1-\nu)} \sum_{i=2}^n \frac{(x_i - x_1) * [(x_i - x_1)^2 - d_{(111)}^2 * (i-1)^2]}{[(x_i - x_1)^2 + d_{(111)}^2 * (i-1)^2]^2} \\ + \frac{b \cos^2 \alpha}{2\pi} \sum_{i=2}^n \frac{(x_i - x_1)}{(x_i - x_1)^2 + d_{(111)}^2 * (i-1)^2}. \end{aligned} \quad (4.26)$$

On the second twinning dislocation,

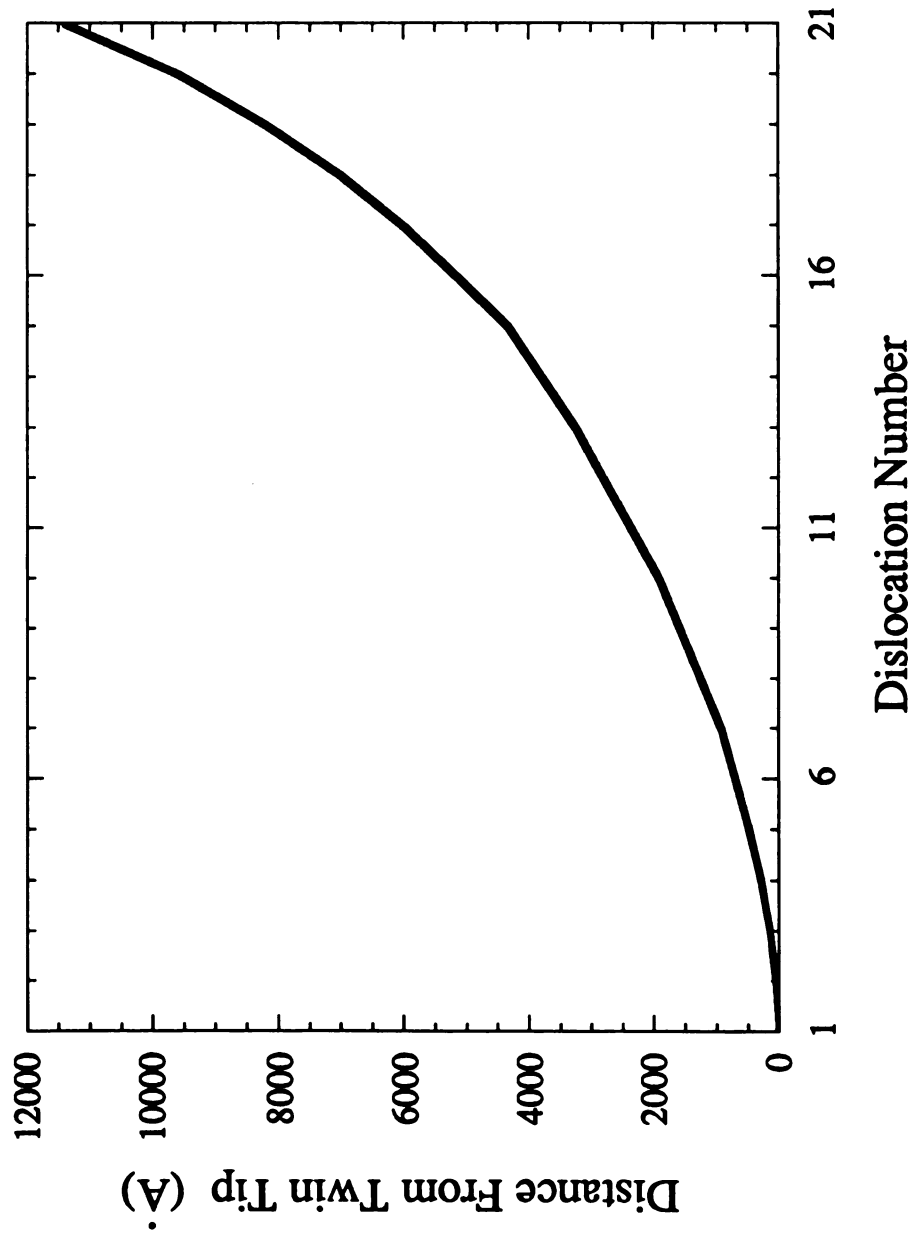


Figure 4.4 - The location of twinning dislocations with respect to the twin tip.

$$\begin{aligned} \frac{F_{f,2}}{Gb} = \frac{F_{f,d.}}{Gb} + \frac{F_{SISF}}{Gb} = \frac{b \sin^2 \alpha}{2\pi(1-\nu)} \sum_{i=3}^n \frac{(x_i - x_2) * [(x_i - x_2)^2 - d_{(111)}^2 * (i-2)^2]}{[(x_i - x_2)^2 + d_{(111)}^2 * (i-2)^2]^2} \\ + \frac{b \cos^2 \alpha}{2\pi} \sum_{i=3}^n \frac{(x_i - x_2)}{(x_i - x_2)^2 + d_{(111)}^2 * (i-2)^2} + \frac{\gamma_{SISF}}{Gb}. \end{aligned} \quad (4.27)$$

On the third twinning dislocation,

$$\begin{aligned} \frac{F_{f,3}}{Gb} = \frac{F_{f,d.}}{Gb} + \frac{F_{SESF}}{Gb} = \frac{b \sin^2 \alpha}{2\pi(1-\nu)} \sum_{i=4}^n \frac{(x_i - x_3) * [(x_i - x_3)^2 - d_{(111)}^2 * (i-3)^2]}{[(x_i - x_3)^2 + d_{(111)}^2 * (i-3)^2]^2} \\ + \frac{b \cos^2 \alpha}{2\pi} \sum_{i=4}^n \frac{(x_i - x_3)}{(x_i - x_3)^2 + d_{(111)}^2 * (i-3)^2} + \frac{\gamma_{SESF}}{Gb}. \end{aligned} \quad (4.28)$$

On the m th twinning dislocation, i.e., on any twinning dislocation beyond the third twinning dislocation,

$$\begin{aligned} \frac{F_{f,m}}{Gb} = \frac{F_{f,d.}}{Gb} + \frac{F_{t.p.}}{Gb} = \frac{b \sin^2 \alpha}{2\pi(1-\nu)} \sum_{i=m+1}^n \frac{(x_i - x_m) * [(x_i - x_m)^2 - d_{(111)}^2 * (i-m)^2]}{[(x_i - x_m)^2 + d_{(111)}^2 * (i-m)^2]^2} \\ + \frac{b \cos^2 \alpha}{2\pi} \sum_{i=m+1}^n \frac{(x_i - x_m)}{(x_i - x_m)^2 + d_{(111)}^2 * (i-m)^2} + \frac{\gamma_{SISF}}{2Gb}. \end{aligned} \quad (4.29)$$

where $m \geq 4$.

In the previous chapter, it has been proved that the twinning dislocations in the twin layer shown in Fig. 4.3 (a) are edge shockley partials $1/6[11\bar{2}]$, so the angle between the Burgers vector and the twinning dislocation line (α) is 90° , and the magnitude of the Burgers vector of twinning dislocations (b) is 1.633 Å. The interplanar spacing of the twinning plane ($d_{(111)}$) is 2.3166 Å for the stoichiometric composition. The shear modulus $G = 69620$ MPa, and Poisson's ratio $\nu = 0.265$ are from [154]. The superlattice intrinsic stacking fault energy (γ_{sisf}) is equal to 70 mJ/m² according to the work done by Hug, Loiseau and Veyssiere ^[6]. Therefore, the superlattice extrinsic stacking fault energy (γ_{sesf}) is 70 mJ/m², and the twinning plane energy ($\gamma_{\text{t.p.}}$) is 35 mJ/m².

If we replace all these values and dislocation positions in table 4.1 into above equations, we have

$$\frac{F_{f.1}}{Gb} = 0.3537 \sum_{i=2}^n \frac{x_i * [x_i^2 - 5.3666 * (i-1)^2]}{[x_i^2 + 5.3666 * (i-1)^2]^2}, \quad (4.30)$$

$$\frac{F_{f.2}}{Gb} = 0.3537 \sum_{i=3}^n \frac{(x_i - 48) * [(x_i - 48)^2 - 5.3666 * (i-2)^2]}{[(x_i - 48)^2 + 5.3666 * (i-2)^2]^2} + 6.1571 \times 10^{-3}, \quad (4.31)$$

$$\frac{F_{f.3}}{Gb} = 0.3537 \sum_{i=4}^n \frac{(x_i - 145) * [(x_i - 145)^2 - 5.3666 * (i-3)^2]}{[(x_i - 145)^2 + 5.3666 * (i-3)^2]^2} + 6.1571 \times 10^{-3}, \quad (4.32)$$

$$\frac{F_{f,m}}{Gb} = 0.3537 \sum_{i=m+1}^n \frac{(x_i - x_m) * [(x_i - x_m)^2 - 5.3666 * (i - m)^2]}{[(x_i - x_m)^2 + 5.3666 * (i - m)^2]^2} + 3.0786 \times 10^{-3}. \quad (4.33)$$

where $m \geq 4$.

When calculating the forward forces, we considered only six dislocations beyond the dislocation concerned, that is, $n - m = 6$ in the above equations, because the interaction force between two dislocations separated with a large distance can be neglected. The calculated results are tabulated as shown in table 4.2 and plotted in Fig. 4.5. The calculation was carried out up to the sixteenth twinning dislocation in the twin layer shown in Fig. 4.3. For the last six dislocations, dislocations 11 to 16, we used some extrapolated dislocation positions in the calculation.

4.3.2. Calculation of Backward Force F_b

Before calculating the backward force, let's first calculate the internal friction force $F_{fric.}$. The internal friction force on a unit length dislocation is

$$\frac{F_{fric.}}{Gb} = \frac{2}{(1-\nu)} \sin(2\pi u/a) \exp\left(-\frac{4\pi\zeta}{b}\right). \quad (4.34)$$

Here the internal friction force is normalized with Gb . If we take the maximum value of $\sin(2\pi u/a)$, i.e., assume $\sin(2\pi u/a) = 1$, the equation (4.34) can be rewritten as

Table 4.2 The forces on each twinning dislocation

Dislocation	Normalized force (F_f/Gb)	Normalized force (F_b/Gb)	Normalized force (F_{ex}/Gb)
1	1.2598×10^{-2}	6.1718×10^{-3}	-6.4262×10^{-3}
2	1.3324×10^{-2}	1.3560×10^{-2}	2.3550×10^{-4}
3	1.1319×10^{-2}	1.2843×10^{-2}	1.5236×10^{-3}
4	7.2392×10^{-3}	8.2083×10^{-3}	9.6910×10^{-4}
5	6.7571×10^{-3}	7.5630×10^{-3}	8.0630×10^{-4}
6	6.3764×10^{-3}	7.3210×10^{-3}	9.4460×10^{-4}
7	5.6098×10^{-3}	7.3130×10^{-3}	1.7032×10^{-3}
8	5.5341×10^{-3}	6.2352×10^{-3}	7.0110×10^{-4}
9	5.3869×10^{-3}	5.9253×10^{-3}	5.3830×10^{-4}
10	4.9830×10^{-3}	5.7939×10^{-3}	8.1090×10^{-4}
11	4.9235×10^{-3}	5.3094×10^{-3}	3.8590×10^{-4}
12	4.8103×10^{-3}	5.1606×10^{-3}	3.5030×10^{-4}
13	4.5376×10^{-3}	5.0948×10^{-3}	5.5720×10^{-4}
14	4.4683×10^{-3}	4.8440×10^{-3}	3.7570×10^{-4}
15	4.0562×10^{-3}	4.7521×10^{-3}	6.9590×10^{-4}
16	3.9493×10^{-3}	4.3423×10^{-3}	3.9300×10^{-4}

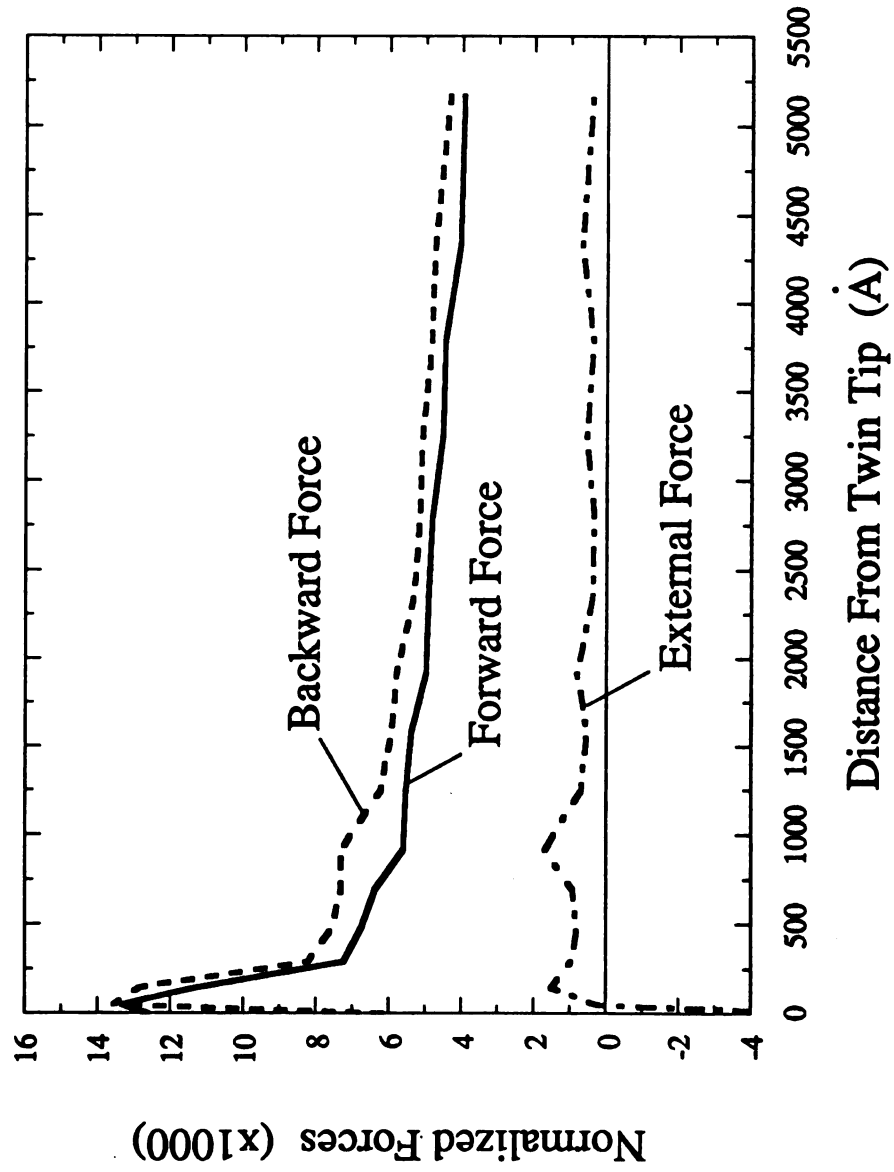


Figure 4.5 - The forces distribution along the twin layer.

$$\frac{F_{fric.}}{Gb} = \frac{2}{1-\nu} \exp\left(-\frac{4\pi\zeta}{b}\right). \quad (4.35)$$

For an edge dislocation, $\zeta = d / (2-2\nu)$, then the equation (4.35) becomes

$$\frac{F_{fric.}}{Gb} = \frac{2}{1-\nu} \exp\left[-\frac{4\pi d}{2b(1-\nu)}\right]. \quad (4.36)$$

We know that $\nu = 0.265$, $d = 2.3166 \text{ \AA}$, $b = 1.633 \text{ \AA}$, so the magnitude of normalized internal friction force ($F_{fric.}/Gb$) is equal to 1.4723×10^{-5} . The direction of $F_{fric.}$ is opposite to the twin propagation direction. This result indicates that the internal friction force is a constant for any twinning dislocation.

The forces due to SISF, SESF and twin interface tension have been calculated in the previous section, that is,

$$\frac{F_{SISF}}{Gb} = \frac{F_{SESF}}{Gb} = \frac{\gamma_{SISF}}{Gb} = 6.1571 \times 10^{-3}. \quad (4.37)$$

$$\frac{F_{t.p.}}{Gb} = \frac{\gamma_{SISF}}{2Gb} = 3.0786 \times 10^{-3}. \quad (4.38)$$

In the following, we will calculate the backward dislocation interaction force. Since the first (leading) twinning dislocation does not have any twinning dislocations ahead of it, there is no backward dislocation interaction force on the first twinning dislocation.

According to the equation (4.3), the backward dislocation interaction force on the second twinning dislocation is

$$\begin{aligned} \frac{F_{b.d.2}}{Gb} = & \frac{b \sin^2 \alpha}{2\pi(1-\nu)} \frac{(x_2 - x_1) * [(x_2 - x_1)^2 - d_{(111)}^2 (2-1)^2]}{[(x_2 - x_1)^2 + d_{(111)}^2 (2-1)^2]^2} \\ & + \frac{b \cos^2 \alpha}{2\pi} \frac{(x_2 - x_1)}{(x_2 - x_1)^2 + d_{(111)}^2 * (2-1)^2}. \end{aligned} \quad (4.39)$$

Since $\alpha = 90^\circ$, $b = 1.633 \text{ \AA}$, $\nu = 0.265$, $d_{(111)} = 2.3166 \text{ \AA}$, $x_2 = 48 \text{ \AA}$, $x_1 = 0$, equation (4.39) becomes

$$\begin{aligned} \frac{F_{b.d.2}}{Gb} = & \frac{1.633}{2 * 3.14 * (1 - 0.265)} \frac{48 * (48^2 - 2.3166^2)}{(48^2 + 2.3166^2)^2} \\ = & 7.3877 \times 10^{-3}. \end{aligned}$$

For the third twinning dislocation,

$$\begin{aligned} \frac{F_{b.d.3}}{Gb} = & \frac{b}{2\pi(1-\nu)} \left\{ \frac{(x_3 - x_2) * [(x_3 - x_2)^2 - d_{(111)}^2]}{[(x_3 - x_2)^2 + d_{(111)}^2]^2} \right. \\ & \left. + \frac{(x_3 - x_1) * [(x_3 - x_1)^2 - d_{(111)}^2 * 2^2]}{[(x_3 - x_1)^2 + d_{(111)}^2 * 2^2]^2} \right\} \end{aligned} \quad (4.40)$$

Putting the known numerical values into (4.40), we have

$$\frac{F_{b.d.3}}{Gb} = 0.3537 * \left[\frac{48 * (48^2 - 2.3166^2)}{(48^2 + 2.3166^2)^2} + \frac{145 * (145^2 - 4 * 2.3166^2)}{(145^2 + 4 * 2.3166^2)^2} \right]$$

$$= 9.7493 \times 10^{-3}$$

Similarly, for the fourth twinning dislocation, we have

$$\begin{aligned} \frac{F_{b.d.4}}{Gb} = & 0.3537 * \left\{ \frac{(x_4 - x_3) * [(x_4 - x_3)^2 - d_{(111)}^2]}{[(x_4 - x_3)^2 + d_{(111)}^2]^2} \right. \\ & + \frac{(x_4 - x_2) * [(x_4 - x_2)^2 - 4 * d_{(111)}^2]}{[(x_4 - x_2)^2 + 4 * d_{(111)}^2]^2} \\ & \left. + \frac{(x_4 - x_1) * [(x_4 - x_1)^2 - 9 * d_{(111)}^2]}{[(x_4 - x_1)^2 + 9 * d_{(111)}^2]^2} \right\}. \end{aligned} \quad (4.41)$$

Here $x_1 = 0$, $x_2 = 48$, $x_3 = 145$, and $x_4 = 290$. So the backward dislocation interaction force on the fourth twinning dislocation is equal to

$$\frac{F_{b.d.4}}{Gb} = 1.4461 \times 10^{-2}$$

In general, the backward dislocation interaction force on the m th twinning dislocation ($m \geq 4$) can be written as

$$\frac{F_{b.d.m}}{Gb} = 0.3537 * \sum_{i=1}^{m-1} \frac{(x_m - x_i) * [(x_m - x_i)^2 - 5.3666 * (m-i)^2]}{[(x_m - x_i)^2 + 5.3666 * (m-i)^2]^2}.$$

(4.42)

Therefore, the backward force for each twinning dislocation in the twin layer shown in Fig. 4.3 can be calculated as follows.

$$\frac{F_{b.1}}{Gb} = \frac{F_{SISF}}{Gb} + \frac{F_{fric.}}{Gb}$$

$$= 6.1571 \times 10^{-3} + 1.4723 \times 10^{-5}$$

$$= 6.1718 \times 10^{-3}$$

$$\frac{F_{b.2}}{Gb} = \frac{F_{b.d.2}}{Gb} + \frac{F_{SESF}}{Gb} + \frac{F_{fric.}}{Gb}$$

$$= 7.3877 \times 10^{-3} + 6.1571 \times 10^{-3} + 1.4723 \times 10^{-5}$$

$$= 1.3560 \times 10^{-2}$$

$$\frac{F_{b.3}}{Gb} = \frac{F_{b.d.3}}{Gb} + \frac{F_{t.p.}}{Gb} + \frac{F_{fric.}}{Gb}$$

$$= 9.7493 \times 10^{-3} + 3.0786 \times 10^{-3} + 1.4723 \times 10^{-5}$$

$$= 1.2843 \times 10^{-2}$$

$$\frac{F_{b.m}}{Gb} = \frac{F_{b.d.m}}{Gb} + \frac{F_{t.p.}}{Gb} + \frac{F_{fric.}}{Gb}$$

(4.43)

$$\begin{aligned}
&= 0.3537 * \sum_{i=1}^{m-1} \frac{(x_m - x_i) * [(x_m - x_i)^2 - 5.3666 * (m-i)^2]}{[(x_m - x_i)^2 + 5.3666 * (m-i)^2]^2} \\
&\quad + 3.0786 \times 10^{-3} + 1.4723 \times 10^{-5} \\
&= 0.3537 \sum_{i=1}^{m-1} \frac{(x_m - x_i) * [(x_m - x_i)^2 - 5.3666 * (m-i)^2]}{[(x_m - x_i)^2 + 5.3666 * (m-i)^2]^2} + 3.0933 \times 10^{-3}.
\end{aligned}$$

where $m \geq 4$. The calculated backward forces are tabulated in table 4.2 and plotted in Fig. 4.5.

4.3.3. Calculation of External Force F_{ex}

According to the definition of the external force in section 4.1.6, we have

$$F_{ex} + F_f + F_b = 0 \quad (4.44)$$

or

$$F_{ex} = F_b - F_f \quad (4.45)$$

that is, the external force is numerically equal to the magnitude of backward force minus the magnitude of corresponding forward force. Thus, the magnitude of external force, F_{ex} , on each twinning dislocation is expressed as follows,

$$\frac{F_{ex.1}}{Gb} = \frac{F_{b.1} - F_{f.1}}{Gb}$$

$$=6.1718 \times 10^{-3} - 0.3537 \sum_{i=2}^n \frac{x_i * (x_i^2 - 5.3666 * (i-1)^2)}{[x_i^2 + 5.3666 * (i-1)^2]^2}. \quad (4.46)$$

$$\frac{F_{ex.2}}{Gb} = \frac{F_{b.2} - F_{f.2}}{Gb}$$

$$=0.3537 \sum_{\substack{i=1 \\ i \neq 2}}^n \frac{(48-x_i) * [(48-x_i)^2 - 5.3666 * (2-i)^2]}{[(48-x_i)^2 + 5.3666 * (2-i)^2]^2}. \quad (4.47)$$

$$\frac{F_{ex.3}}{Gb} = \frac{F_{b.3} - F_{f.3}}{Gb}$$

$$=0.3537 \sum_{\substack{i=1 \\ i \neq 3}}^n \frac{(145-x_i) * [(145-x_i)^2 - 5.3666 * (3-i)^2]}{[(145-x_i)^2 + 5.3666 * (3-i)^2]^2} - 3.0786 \times 10^{-3}.$$

(4.48)

$$\frac{F_{ex.m}}{Gb} = \frac{F_{b.m} - F_{f.m}}{Gb}$$

$$0.3537 \sum_{\substack{i=1 \\ i \neq m}}^n \frac{(x_m - x_i) * [(x_m - x_i)^2 - 5.3666 * (m-i)^2]}{[(x_m - x_i)^2 + 5.3666 * (m-i)^2]^2}, \quad (4.49)$$

where $m \geq 4$. The subscripts "m" and "i" represent the corresponding dislocation number.

The calculated results are listed in table 4.2 and plotted in Fig. 4.5. From the results, we can see that the external force on the first twinning dislocation is negative. This will be discussed later.

4.4. Stresses in The Thin Twin Layer

Stresses in the thin twin layer are classified into three categories similar to the forces on the twinning dislocation: (i) forward shear stress, τ_f , that produces the forward force (F_f); (ii) backward shear stress (or back stress), τ_b , corresponding to the backward force (F_b); and (iii) external shear stress, τ_{ex} , corresponding to the external force (F_{ex}). The external shear stress includes the externally applied stress, the locally concentrated stress and the residual stress within the matrix. Since the effect of stress normal to the twin plane on the twinning dislocation glide are negligible comparing to that of the shear stresses ^[154], we will not consider the normal stress in the stress calculation. Therefore, the above three shear stresses are simply called forward stress, back stress and external stress, respectively. The terminology "external" here means that the stress is from the sources outside the twin layer, that is, it exists in the matrix even before the formation of the twin layer. However, the internal stress (either forward stress or back stress) is an intrinsic stress that is related to the formation of the twin, that is, it results from the internal sources such as twinning dislocation interaction, twin interface tension, and lattice friction on twinning dislocation motion.

The shear stress and the force on a dislocation per unit length, which is

perpendicular to the dislocation line, are correlated in the form of

$$F = \tau \cdot b \quad (4.50)$$

Therefore, the shear stress τ can be easily obtained by dividing the magnitude of force (F) by the length of Burgers vector (b), i.e.,

$$\tau = F/b \quad (4.51)$$

This calculated shear stress is the stress at the location of the corresponding twinning dislocation.

In what follows, we will list all formulas used in the calculation of shear stresses.

The calculated results will be shown in table 4.3 and Fig. 4.6.

For the forward stress τ_f

$$\tau_{f.1} = 24624.29 \sum_{i=2}^n \frac{x_i * [x_i^2 - 5.3666 * (i-1)^2]}{[x_i^2 + 5.3666 * (i-1)^2]^2}, \quad (4.52)$$

$$\tau_{f.2} = 24624.29 \sum_{i=3}^n \frac{(x_i - 48) * [(x_i - 48)^2 - 5.3666 * (i-2)^2]}{[(x_i - 48)^2 + 5.3666 * (i-2)^2]^2} + 428.66, \quad (4.53)$$

$$\tau_{f.3} = 24624.29 \sum_{i=4}^n \frac{(x_i - 145) * [(x_i - 145)^2 - 5.3666 * (i - 3)^2]}{[(x_i - 145)^2 + 5.3666 * (i - 3)^2]^2} + 428.66, \quad (4.54)$$

$$\tau_{f.m} = 24624.29 \sum_{i=m+1}^n \frac{(x_i - x_m) * [(x_i - x_m)^2 - 5.3666 * (i - m)^2]}{[(x_i - x_m)^2 + 5.3666 * (i - m)^2]^2} + 214.33, \quad (4.55)$$

where $m \geq 4$. The subscripts indicate the correspondent twinning dislocation numbers. This notation is also applicable to the following formulas. The unit of stress is MPa, and this is the same in the following equations.

For the back stress τ_b

$$\tau_{b.1} = \frac{F_{b.1}}{b} = 429.68 \text{ (MPa)}, \quad (4.56)$$

$$\tau_{b.2} = \frac{F_{b.2}}{b} = 944.01 \text{ (MPa)}, \quad (4.57)$$

$$\tau_{b.3} = \frac{F_{b.3}}{b} = 894.10 \text{ (MPa)}, \quad (4.58)$$

$$\tau_{b.m} = 24624.29 \sum_{i=1}^{m-1} \frac{(x_m - x_i) * [(x_m - x_i)^2 - 5.3666 * (m - i)^2]}{[(x_m - x_i)^2 + 5.3666 * (m - i)^2]^2} + 215.36, \quad (4.59)$$

Table 4.3 The stresses at each twinning dislocation

Dislocation	τ_f (MPa)	τ_b (MPa)	τ_{ex} (MPa)
1	877.07	429.68	-447.39
2	926.92	944.01	17.09
3	781.97	894.10	112.04
4	503.99	571.46	70.94
5	470.43	526.54	57.10
6	443.92	509.69	65.68
7	390.55	509.13	118.12
8	385.28	434.09	48.09
9	375.04	412.51	36.40
10	346.92	399.55	55.44
11	342.77	369.64	25.84
12	334.89	359.28	23.36
13	315.91	354.70	37.77
14	311.08	337.24	30.33
15	282.39	330.84	47.41
16	274.95	302.31	26.33

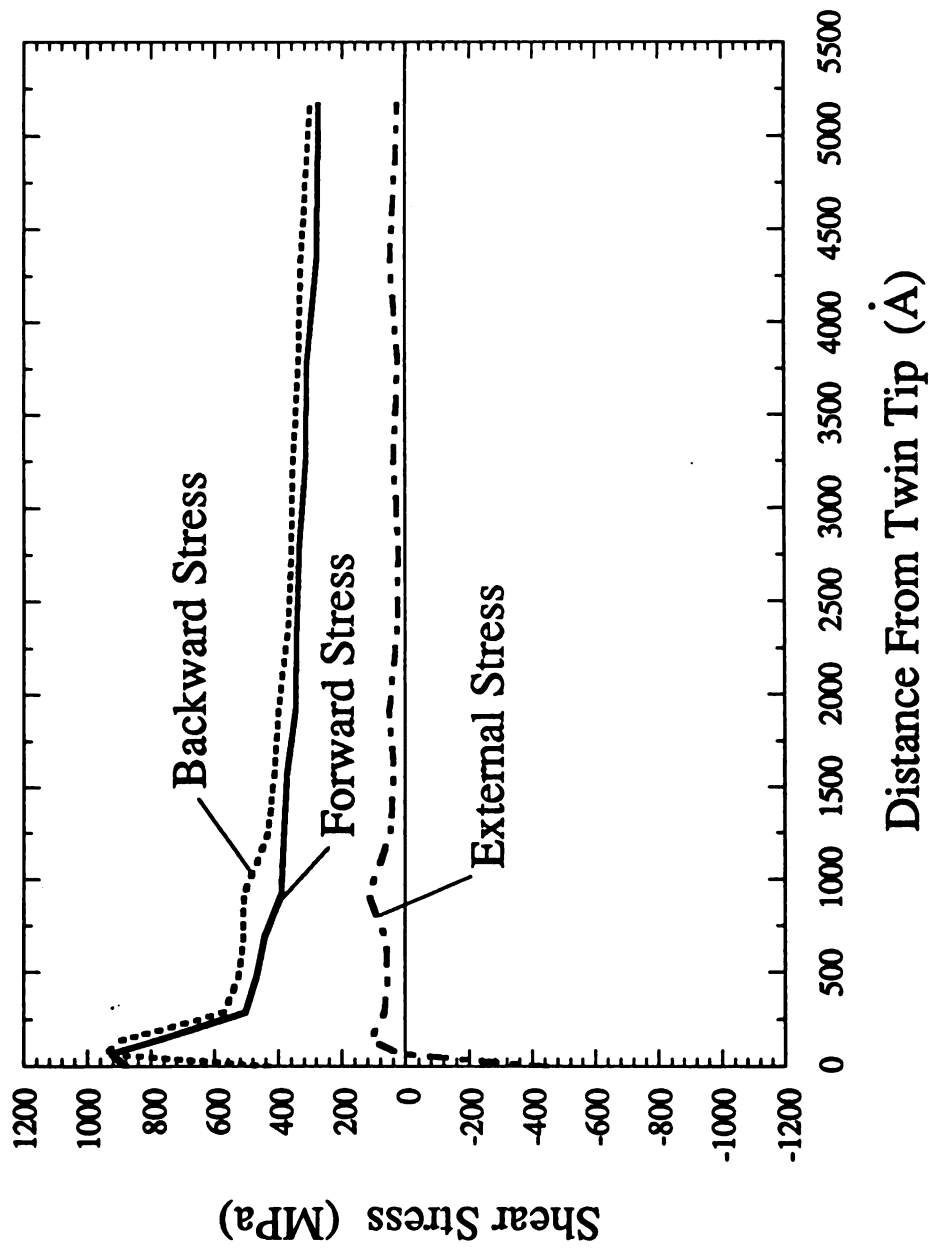


Figure 4.6 - Shear stresses distribution in the thin twin layer.

where $m \geq 4$.

For the external stress τ_{ex}

$$\tau_{ex.1} = 429.68 - 24624.29 \sum_{i=2}^n \frac{x_i * (x_i^2 - 5.3666 * (i-1)^2)}{[x_i^2 + 5.3666 * (i-1)^2]^2}, \quad (4.60)$$

$$\tau_{ex.2} = 24624.29 \sum_{\substack{i=1 \\ i \neq 2}}^n \frac{(48 - x_i) * [(48 - x_i)^2 - 5.3666 * (2-i)^2]}{[(48 - x_i)^2 + 5.3666 * (2-i)^2]^2}, \quad (4.61)$$

$$\tau_{ex.3} = 24624.29 \sum_{\substack{i=1 \\ i \neq 3}}^n \frac{(145 - x_i) * [(145 - x_i)^2 - 5.3666 * (3-i)^2]}{[(145 - x_i)^2 + 5.3666 * (3-i)^2]^2} - 214.33, \quad (4.62)$$

$$\tau_{ex.m} = 24624.29 \sum_{\substack{i=1 \\ i \neq m}}^n \frac{(x_m - x_i) * [(x_m - x_i)^2 - 5.3666 * (m-i)^2]}{[(x_m - x_i)^2 + 5.3666 * (m-i)^2]^2}. \quad (4.63)$$

4.5. Simplified Equations for F_f , F_b and F_{ex}

Let's see an example how the equations are simplified. The equation (4.26) can be rewritten as

$$\begin{aligned}
\frac{F_{f.1}}{Gb} = & \frac{b \sin^2 \alpha}{2\pi(1-\nu)} \sum_{i=2}^n \frac{1}{x_i - x_1} \frac{1 - \frac{d^2_{(111)} * (i-1)^2}{(x_i - x_1)^2}}{\left[1 + \frac{d^2_{(111)} * (i-1)^2}{(x_i - x_1)^2}\right]^2} \\
& + \frac{b \cos^2 \alpha}{2\pi} \sum_{i=2}^n \frac{1}{x_i - x_1} \frac{1}{1 + \frac{d^2_{(111)} * (i-1)^2}{(x_i - x_1)^2}}. \quad (4.64)
\end{aligned}$$

Since

$$\frac{d^2_{(111)} * (i-1)^2}{(x_i - x_1)^2} \ll 1,$$

the equation (4.64) can be reduced as

$$\frac{F_{f.1}}{Gb} = \left[\frac{b \sin^2 \alpha}{2\pi(1-\nu)} + \frac{b \cos^2 \alpha}{2\pi} \right] \sum_{i=2}^n \frac{1}{x_i - x_1}. \quad (4.65)$$

In a similar way, we can simplify all equations used for the calculation of F_f , F_b and F_{ex} as follows.

For the forward force F_f

$$\frac{F_{f.1}}{Gb} = 0.3537 \sum_{i=2}^n \frac{1}{x_i}, \quad (4.66)$$

$$\frac{F_{f.2}}{Gb} = 0.3537 \sum_{i=3}^n \frac{1}{x_i - 48} + 6.1571 \times 10^{-3}, \quad (4.67)$$

$$\frac{F_{f.3}}{Gb} = 0.3537 \sum_{i=4}^n \frac{1}{x_i - 145} + 6.1571 \times 10^{-3}, \quad (4.68)$$

$$\frac{F_{f.m}}{Gb} = 0.3537 \sum_{i=m+1}^n \frac{1}{x_i - x_m} + 3.0786 \times 10^{-3}. \quad (4.69)$$

For the backward force F_b

$$\frac{F_{b.m}}{Gb} = 0.3537 \sum_{i=1}^{m-1} \frac{1}{x_m - x_i} + 3.0933 \times 10^{-3}. \quad (4.70)$$

where $m \geq 4$.

For the external force F_{ex}

$$\frac{F_{ex.1}}{Gb} = 6.1718 \times 10^{-3} - 0.3537 \sum_{i=2}^n \frac{1}{x_i}, \quad (4.71)$$

$$\frac{F_{ex.2}}{Gb} = 0.3537 \sum_{\substack{i=1 \\ i \neq 2}}^n \frac{1}{48-x_i}, \quad (4.72)$$

$$\frac{F_{ex.3}}{Gb} = 0.3537 \sum_{\substack{i=1 \\ i \neq 3}}^n \frac{1}{145-x_i} - 3.0786 \times 10^{-3}, \quad (4.73)$$

$$\frac{F_{ex.m}}{Gb} = 0.3537 \sum_{\substack{i=1 \\ i \neq m}}^n \frac{1}{x_m-x_i}, \quad (4.74)$$

where $i \geq 4$.

The results calculated using these simplified equations are shown in table 4.4. The comparison between the results calculated from the original equations and the results from the simplified equations, as shown in Fig. 4.7, indicates that the results from the simplified equations can perfectly represent the results obtained from the original equations. The deviations between the results from the simplified equations and the results from the original equations are very small, only about ± 0.024 . So we can directly use the simplified equations in the calculation of forces on the twinning dislocations.

Table 4.4 The forces calculated using simplified equations

Dislocation	F_f/Gb	F_b/Gb	F_{cx}/Gb
1	1.2660×10^{-2}	6.1718×10^{-3}	-6.4882×10^{-3}
2	1.3039×10^{-2}	1.3644×10^{-2}	6.0500×10^{-4}
3	1.1322×10^{-2}	1.2901×10^{-2}	1.5790×10^{-4}
4	7.2409×10^{-3}	8.2139×10^{-3}	9.7300×10^{-4}
5	6.7583×10^{-3}	7.5663×10^{-3}	8.0800×10^{-4}
6	6.3773×10^{-3}	7.3230×10^{-3}	9.4570×10^{-4}
7	5.6102×10^{-3}	7.3151×10^{-3}	1.7049×10^{-3}
8	5.5345×10^{-3}	6.2365×10^{-3}	7.0200×10^{-4}
9	5.3871×10^{-3}	5.9257×10^{-3}	5.3860×10^{-4}
10	4.9831×10^{-3}	5.7944×10^{-3}	8.1130×10^{-4}
11	4.9235×10^{-3}	5.3096×10^{-3}	3.8610×10^{-4}
12	4.8104×10^{-3}	5.1607×10^{-3}	3.5030×10^{-4}
13	4.5376×10^{-3}	5.0950×10^{-3}	5.5740×10^{-4}
14	4.3936×10^{-3}	4.8442×10^{-3}	4.5060×10^{-4}
15	4.0562×10^{-3}	4.752×10^{-3}	6.9580×10^{-4}
16	3.9493×10^{-3}	4.3423×10^{-3}	3.9300×10^{-4}

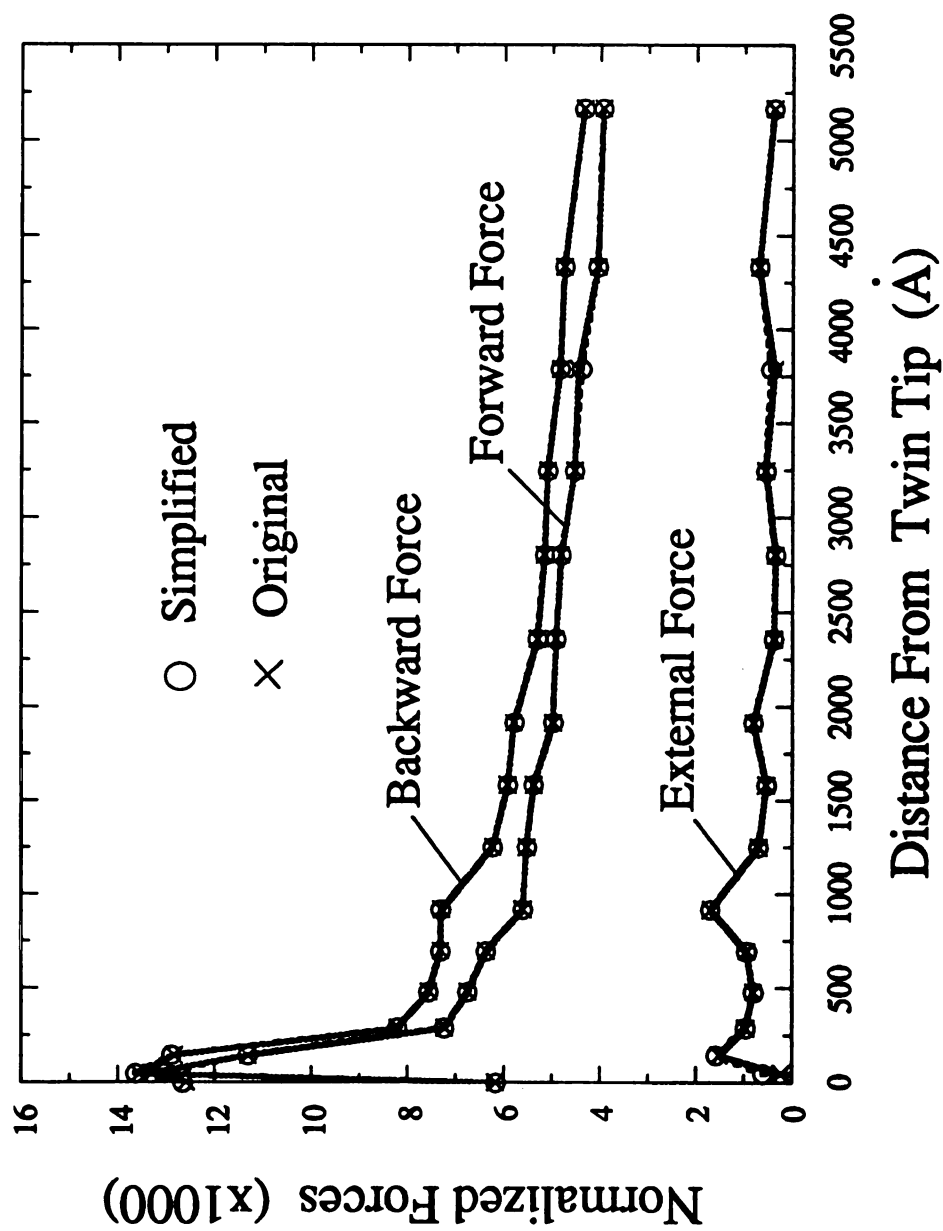


Figure 4.7 - Comparisons of results obtained from the original equations with results obtained from the simplified equations.

4.6. Discussion

4.6.1. Stress and Force Distributions Within The Twin Layer

From the previous results, we can see that the force distributions along the twin layer is similar to the stress distributions. So we will analyze only the stress distributions in this section, and this analysis is also applicable to the force distributions.

(a) External Stress τ_{ex}

External stress has been defined as the stress resulting from the externally applied load, the local stress concentration and the residual stress within the matrix. Since the specimen was free from external load during the TEM investigation, the externally applied stress term can be eliminated from the external stress. Investigating the external stress line in Fig. 4.6, we can see that the external stress is more or less evenly distributed along the thin twin layer, which indicates that no stress concentration exists within the region of the twin layer investigated. Also, no stress concentration would be expected in the middle of a grain. This means that the external stress calculated in this study may be purely a residual stress within the matrix where the twin layer was growing. It is possible that the twin layer investigated has propagated long enough so that the front portion of twin layer, which we are studying, has been out of the range of local stress concentration that is at the grain boundary, as shown in Chapter Three. The negative value of external stress at the twin tip may be due to the wrong values of back stress and forward stress, which will be analyzed in the following section. So taking an average of the calculated external stresses with neglect of the stress at the first twinning

dislocation, the residual stress (τ_m) in the matrix is

$$\tau_{rs} = [\tau_{ex}]_{av.} = 51 \text{ MPa} \quad (4.75)$$

where $[\tau_{ex}]_{av.}$ means the average value of external stresses except for the stress at the first twinning dislocation. We assume now that the external stress, equal to the residual stress in this case, is distributed evenly along the thin twin layer including the first twinning dislocation. Then the driving force resulting from the external stress is the same for all the twinning dislocations in the thin twin layer of Fig. 4.3 (a).

(b) Forward Stress τ_f

The forward stress, which is an internal stress resulting from the dislocation interaction and the twin interface tension, decreases as the distance from the twin tip increases, as shown in Fig. 4.6. This decrement of forward stress is remarkable near the twin tip up to about 1000 Å, which corresponds to the location of the seventh twinning dislocation, and the decrease becomes gentle beyond about 1000 Å. The forward stress tends toward a constant value far from the twin tip. This indicates that the driving force for the twinning dislocation glide resulting from the forward stress is different for the dislocations located at different places in the twin layer. The driving force necessary for the twinning dislocation glide is very large near the twin tip, and it drops quickly as the distance increases. Therefore, the twinning dislocations having large distance from the twin tip glide forward more easily than the twinning dislocations near the twin tip.

The forward stress at the first twinning dislocation is smaller than that at the second twinning dislocation, as seen in Fig 4.6 and in table 4.3. This is possibly due to the incorrect approximation of location of the second twinning dislocation. So if we extrapolate the plot of forward stress using the data from the third dislocation to the sixth dislocation, we have the forward stress at the first and the second twinning dislocations equal to 1245.6 MPa and 1059.4 MPa, respectively. Thus the modified forward stress distribution along the thin twin layer is as shown in Fig 4.8. The corresponding forward force distribution is shown in Fig. 4.9.

(c) Back Stress τ_b

The back stress is an internal stress, which results from the dislocation interaction, the twin interface tension and the internal friction on the twinning dislocations. The change of back stress with the distance is similar to that of forward stress, that is, back stress drops very quickly with the distance near the twin tip, and decreases gently with the distance when the distance is large. Since the back stress results in a force (backward force) opposite to the twin propagation direction, the back stress resists the twinning dislocation glide, so it must be overcome in order for twinning dislocations to move forward during the twin propagation. So the resistance to dislocation glide in the twin layer is very large near the twin tip and relatively small at a location far away from the twin tip. In other words, the trailing twinning dislocations have less resistance for glide than the leading twinning dislocations, so the trailing twinning dislocations more easily glide comparing to the leading twinning dislocations. This conclusion is the same as that drawn from the forward stress analysis.

Table 4.5 The modified stresses and forces for the first three twinning dislocations

Dislocation	$\tau_{f, \text{tip}}$ (MPa)	$\tau_{\text{fric}, \text{tip}}$ (MPa)	$\tau_{b, \text{tip}}$ (MPa)	$F_{f, \text{tip}}/\text{Gb}$	$F_{\text{fric}, \text{tip}}/\text{Gb}$	$F_{b, \text{tip}}/\text{Gb}$
1	1245.6 ^a	866.9	1296.6	1.789×10^{-2}	1.245×10^{-2}	1.862×10^{-2}
2	1059.4 ^a	166.4	1110.4	1.522×10^{-2}	2.389×10^{-3}	1.595×10^{-2}
3	772.8 ^a	-70.2	824.9	1.110×10^{-2}	1.472×10^{-3}	1.197×10^{-2}
	782.0 ^b	1.02 ^c	833.0 ^b	1.123×10^{-2} ^b		1.197×10^{-2} ^b

Notes: a. These data fit the equation

$$\tau_{f, \text{tip}} = 1245.55 - 4.215 x_i + 7.15 \times 10^{-3} x_i - 3.9 \times 10^{-6} x_i.$$

b. These data are obtained without modification.

c. It is a Peierls stress calculated using Peierls-Nabarro equation (5.4).

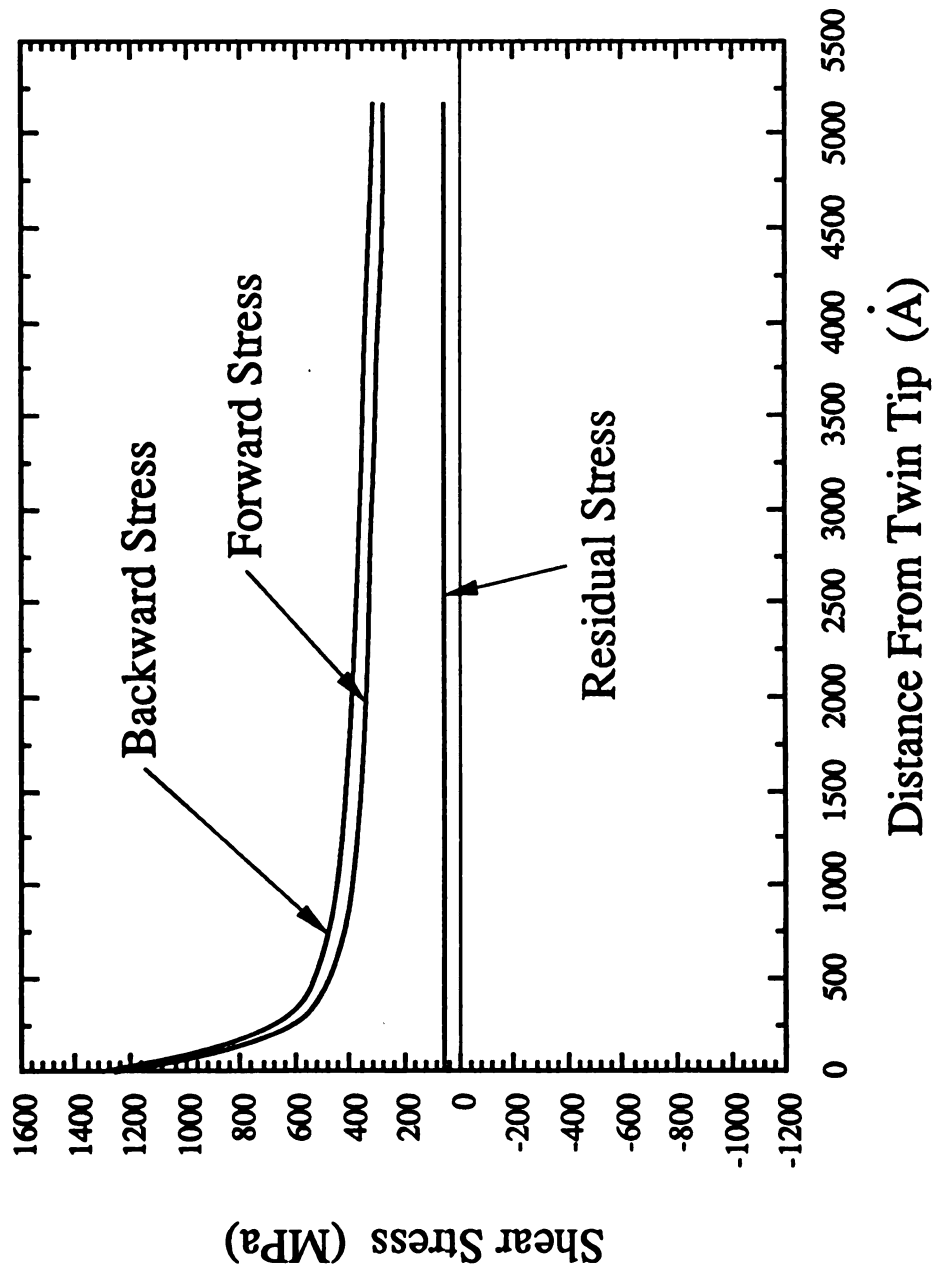


Figure 4.8 - The modified stress distribution along the thin twin layer.

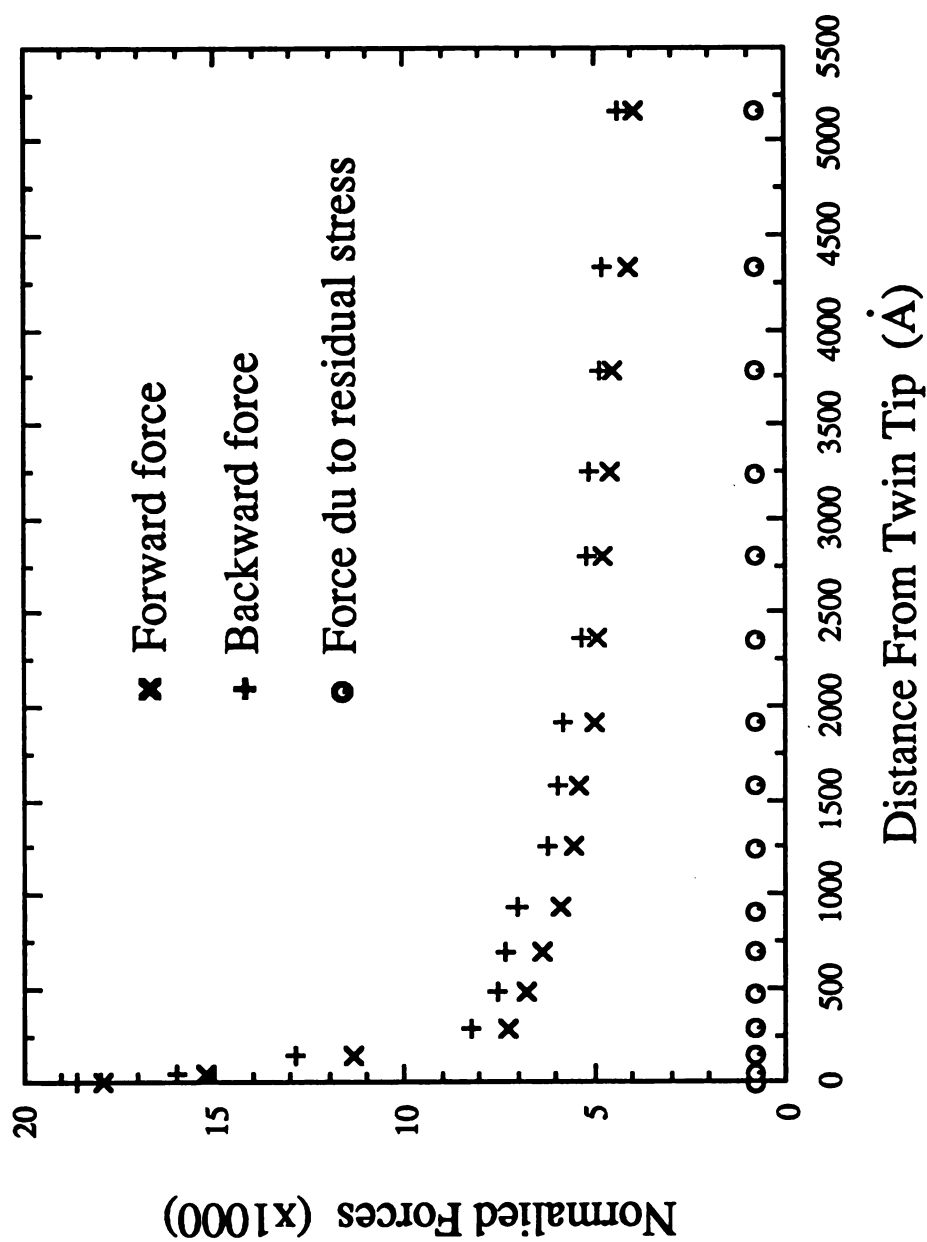


Figure 4.9 - The modified force distribution along the thin twin layer.

Comparing the back stress with the forward stress on the first twinning dislocation in the twin layer as shown in Fig. 4.6 and in table 4.3, we can see that the back stress is smaller than the forward stress. If this were true, the first twinning dislocation should glide further forward until the forward stress at the first twinning dislocation was equal to the back stress. But this is not what we observed since the twin tip was stationary. Therefore, there may exist a very large internal friction on the first twinning dislocation (or say for the twinning dislocations near the twin tip). This internal friction on the dislocations near the twin tip should be much larger than that on the dislocations located far away from the twin tip. The magnitude of internal friction stress at the dislocations near the twin tip are equal to the difference between the forward stress, the residual stress and the stress due to the stacking fault ($\tau_{S.F.}$), the back stress ($\tau_{b.d.}$) i.e.,

$$\tau_{fric,tip} = \tau_f + \tau_{rs} - \tau_{S.F.} - \tau_{b.d.}, \quad (4.76)$$

where $\tau_{fric,tip}$ is the internal friction stress on the twinning dislocations near the twin tip. The corresponding internal friction force on the dislocations near the twin tip is equal to the difference between the corresponding driving force (the forward force plus the force due to the residual stress) and the backward forces due to the stacking fault and the dislocation interaction,

$$F_{fric,tip} = F_f + F_{rs} - F_{S.F.} - F_{b.d.}, \quad (4.77)$$

where $F_{fric,tip}$ is the internal friction force on the twinning dislocations at the twin tip, F_n

is the force resulting from the residual stress τ_{rs} . So the modified back stress and the modified backward force should be

$$\tau_{b,tip} = \tau_{f,tip} + \tau_{cx} = \tau_{f,tip} + \tau_{rs}, \quad (4.78)$$

$$F_{b,tip} = F_{f,tip} + F_{rs}, \quad (4.79)$$

or

$$F_{b,tip} = b \tau_{b,tip}. \quad (4.80)$$

Here the subscripts "f.tip" indicates the modified forward stress and modified forward force at the twin tip. The modified forward stresses at the twin tip have been calculated for the first three twinning dislocations in the previous section, so the modified back stresses and the modified backward forces for the first three twinning dislocations can be easily calculated using equations (4.78) and (4.80). The results of the modified stresses and the modified forces for the first three twinning dislocations are listed in table 4.5. The plots for modified stresses are shown in Fig. 4.8 and for modified forces in Fig. 4.9.

4.6.2. Dislocation Distribution in The Case of Equal Backward Force or Equal Driving Force on Each Twinning Dislocation

At an equilibrium condition, the backward force on a twinning dislocation should be equal to the driving force on the same twinning dislocation. Thus the equal backward force condition is equivalent to the situation of equal driving force when we consider the

twinning dislocation distribution in a twin layer.

If we assume the backward force on any twinning dislocation is constant, then the twinning dislocation distribution within a twin layer will be uniform, i.e., the spacing between any two adjacent twinning dislocations will be constant, as shown in Fig. 4.10. Here we selected a normalized backward force equal to 1.18×10^{-2} . The result shows that if the backward force on every twinning dislocation is equal to 1.18×10^{-2} Gb, the spacing between any two adjacent twinning dislocations, except for the first two twinning dislocations, is equal to 164 Å. This result is inconsistent with the experimental observation shown in Fig. 3.1 and Fig. 3.5. So this result indirectly proves that the backward force (and the forward force) along a twin layer is not constant.

4.6.3. Effect of Dislocation Location on The Stress Distribution

Fig. 4.11 (a) shows how much the deviation of the second twinning dislocation location from the measured position affects the back stress on this dislocation. We selected ± 10 Å deviation from the measured value 48 Å. This deviation of the dislocation location results in either 131 MPa stress increment when the dislocation is at the left side of the measured position or 87 MPa stress decrement when the dislocation is located at the right side of the measured position. This indicates that a small deviation of the dislocation location results in a large variation in stress on the second dislocation. Location of the third twinning dislocation has a similar effect on the stress as the second one, as shown in Fig. 4.11 (b), however, the effect is less than the second one. In Fig. 4.11 (b), the deviation of ± 10 from the measured value, 145 Å, results in either 42 MPa

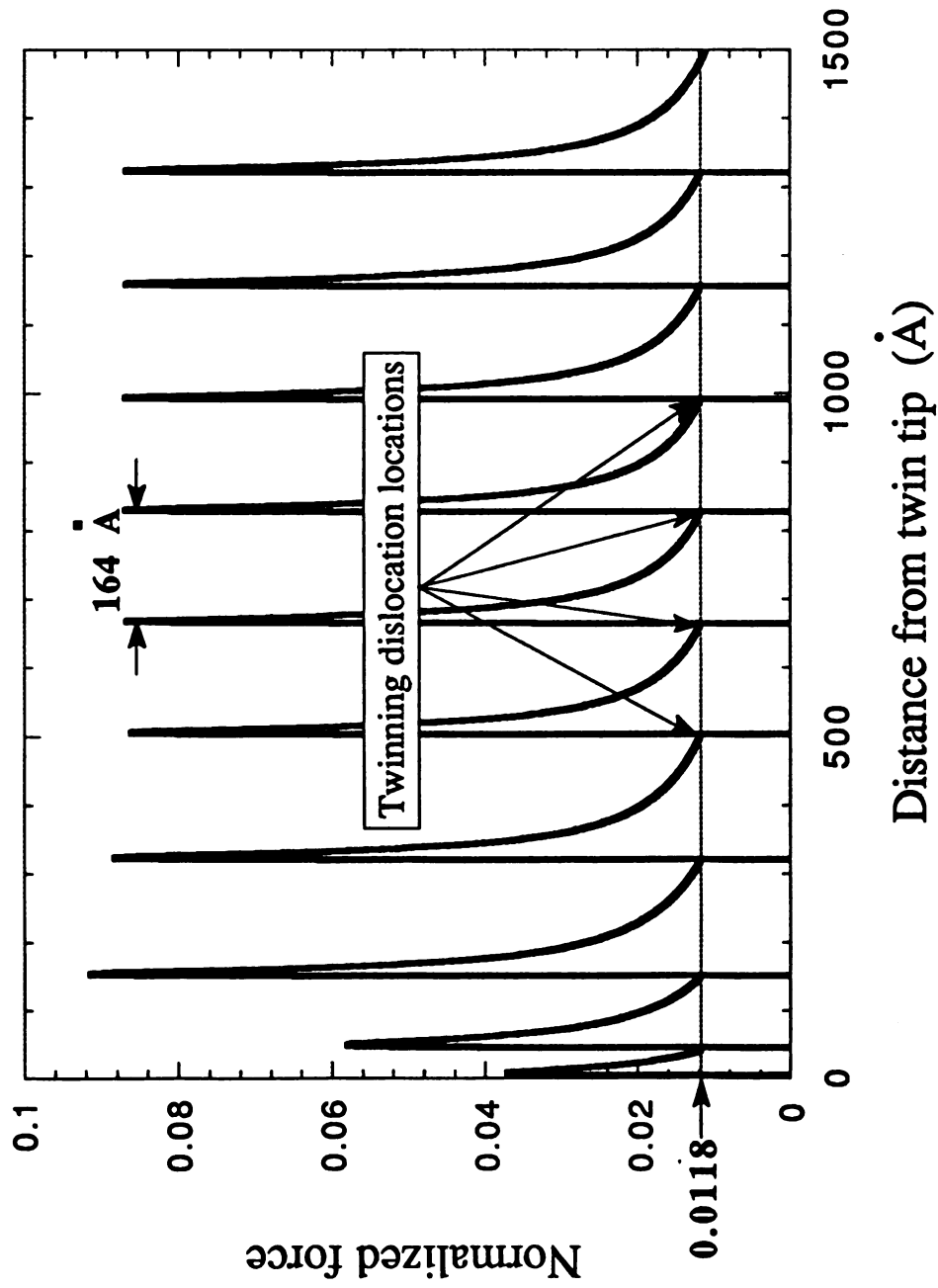


Figure 4.10 - Dislocation distribution at equal backward force on every twinning dislocation. ($F_t/Gb = 1.18 \times 10^{-2}$).

increase in stress on the right side of the measured position or 34 MPa decrease in stress on the right side of the measured position. If we look at the tenth dislocation, as shown in Fig. 11 (c), the effect of deviation of dislocation location from the measured position on the stress is very small. ± 10 deviation results in only +4 or -3 variation in stress. Even at the deviation of ± 50 for the tenth twinning dislocation location, the stress change is only +20 or -15 MPa that is still smaller than those for the second and the third twinning dislocations at the deviation of ± 10 . Therefore, the determination of twinning dislocation positions is very important for the dislocations near the twin tip. For the dislocations far away from the twin tip, a slight deviation from the correct position does not change the stress much. This is reason why the stress curves in Fig. 4.6 are rough near the origin of the distance axis (near the twin tip).

4.7. Summary

The distributions of forces and stresses along a thin twin layer was numerically calculated based on the dislocation theory and the morphology of twin nucleation and propagation analyzed in previous chapter. The forces acting on a twinning dislocation are classified into three categories: forward force, backward force and external force. The corresponding stresses are forward stress, back stress and external stress. The calculation was carried out based on the twinning dislocation locations in an experimentally observed thin twin layer. The results show that both forward stress and back stress are very large at the twin tip and drop quickly as the distance from the twin tip increases. The external stress is the residual stress in the matrix, which is uniformly

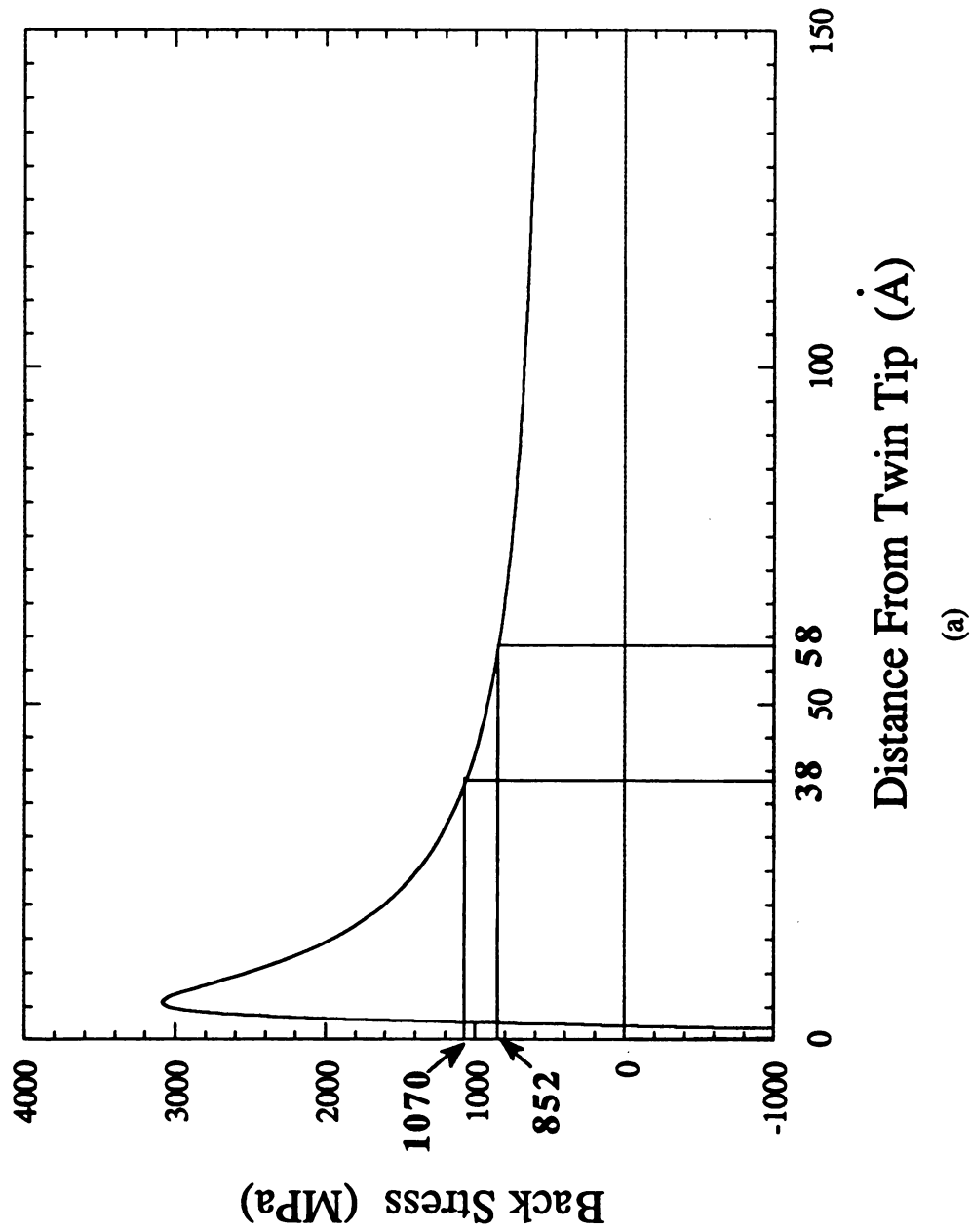
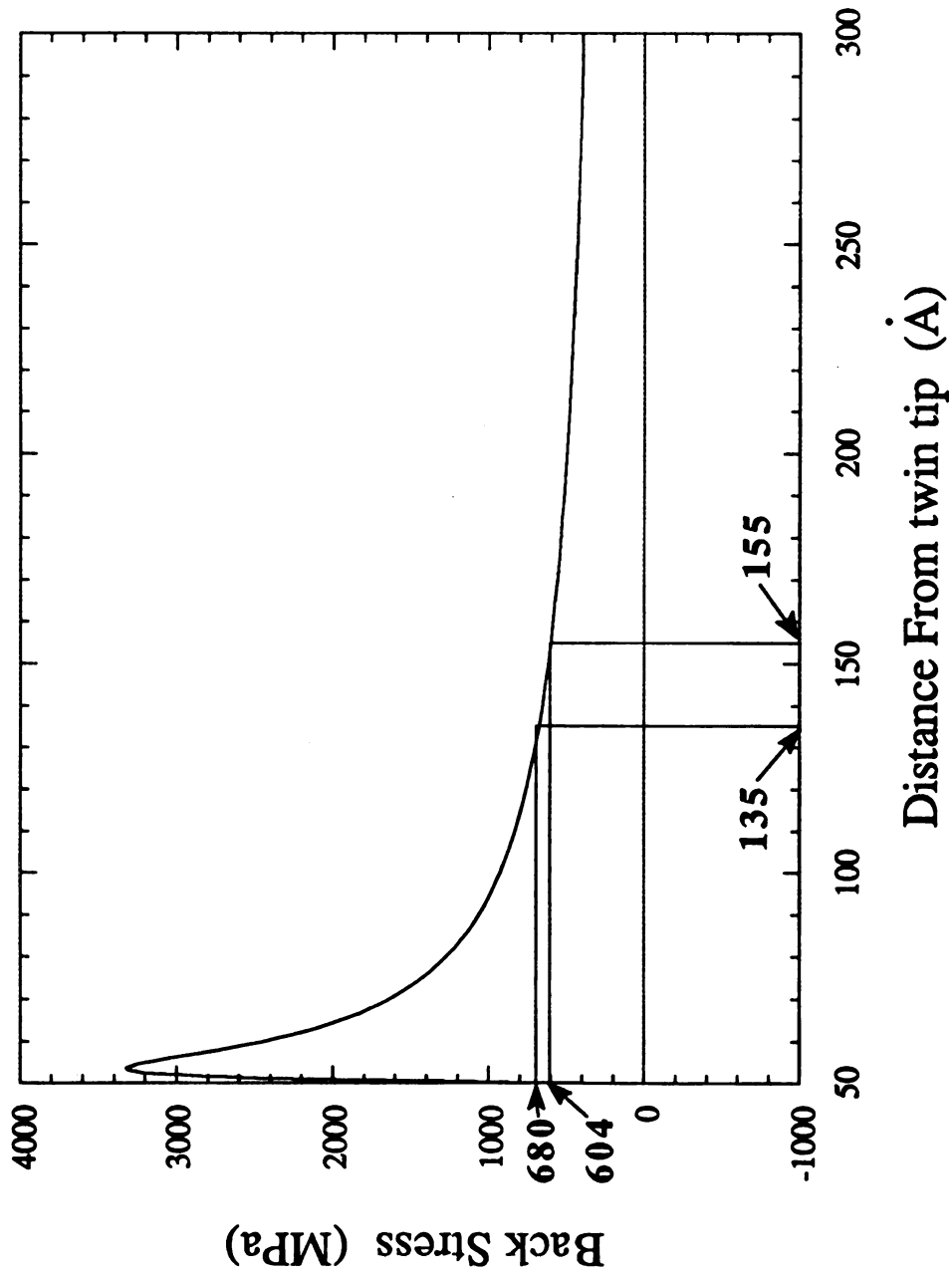
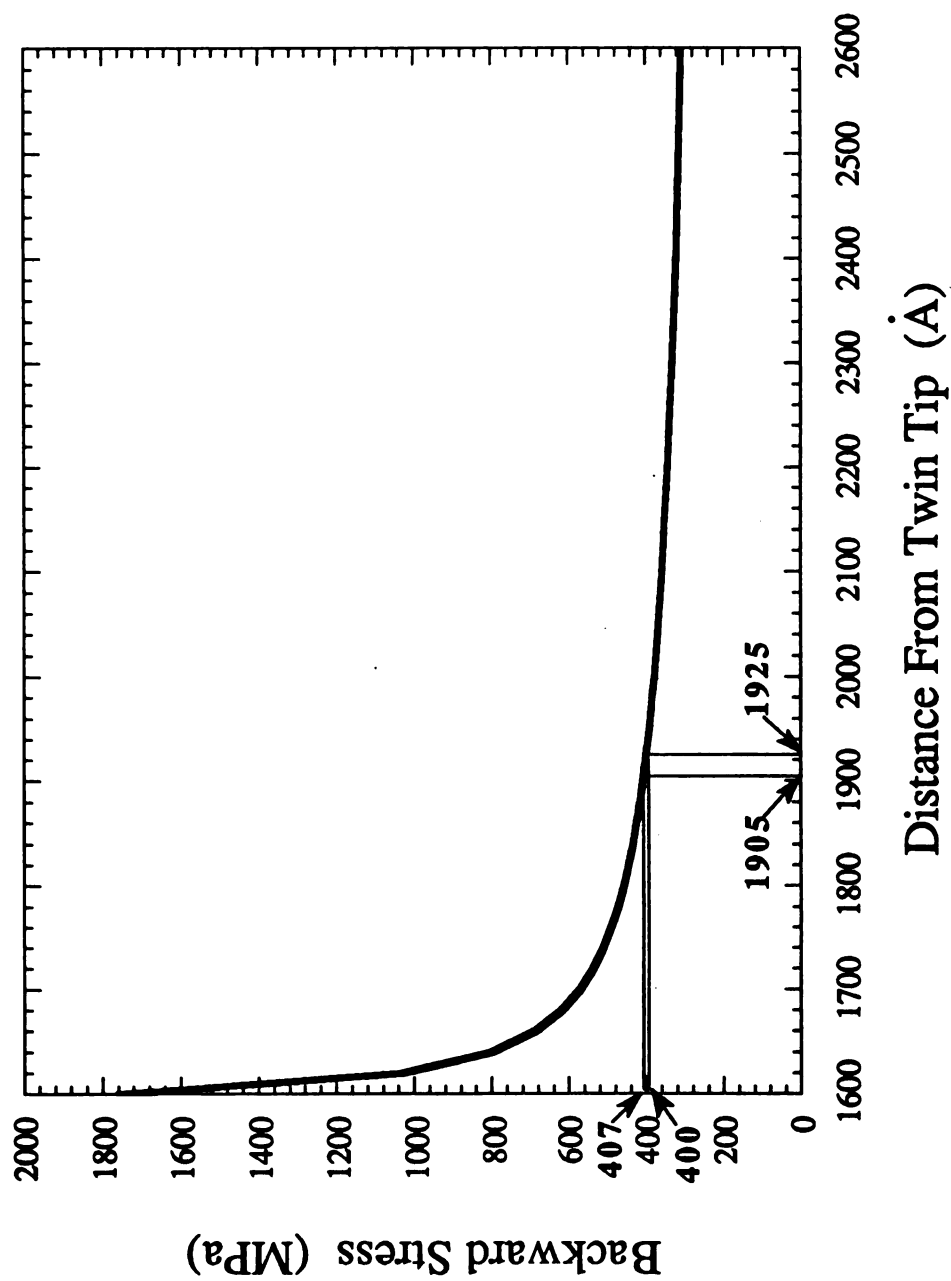


Figure 4.11 - Effect of the twinning dislocation location on the backward stress. (a) For the second dislocation, (b) for the third dislocation, and (c) for the tenth dislocation.



(b)

(Figure 4.11 continued)



(c)

(Figure 4.11 continued)

distributed along the twin layer. Comparison between the original equations and the simplified equations for the calculation of forces and stresses shows that there is a very small difference between them.

CHAPTER FIVE

MECHANICAL TWINNING DURING CREEP DEFORMATION IN TiAl

5.1. Introduction

In recent years, much work has been done to understand deformation mechanisms of TiAl in short term properties both at room temperature and at high temperature ^[1,4,155]. But for long term creep deformation, much less information is available in the literature. Also, there are two differing results concerning mechanical twinning in creep deformation of TiAl. Loiseau and Lasalmonie ^[22] investigated creep deformation of equiaxed single phase γ Ti₄₆Al₅₄ and found that mechanical twinning was an important creep deformation mechanism at deformation temperatures up to 800 °C. Huang and Kim ^[39] studied creep behavior of two phase $\gamma + \alpha_2$ alloy with composition of Ti-47.0Al-1.0Cr-1.0V-2.5Nb at 900 °C and observed no evidence of mechanical twinning in creep deformation. Since one goal of TiAl components will be to replace nickel and cobalt base superalloys in aircraft applications, understanding creep deformation at high temperatures is necessary. However, creep deformation mechanisms are not clearly identified: (1) The activation energies for creep are much larger than those for self-diffusion and interdiffusion in TiAl ^[37,41,42], which suggests that the creep rate may be controlled by processes other than the usual lattice diffusion mechanism; (2) The reported

value of the stress exponent varies widely from about 2 to 8 [43,44,156,157]. This indicates that several deformation mechanisms are involved in the creep of TiAl. The details of deformation mechanisms are not known and the limited results in the literature are not consistent with the creep theory. Mechanical twinning has been found to be an important component of creep deformation in TiAl [22,28,29]. It is possible that a parallel creep deformation mechanism exists in the case when the mechanical twinning and some other creep deformation mechanisms such as dislocation movement, diffusion, recovery, and so on, occur independently. Therefore, it is important to understand the mechanical twinning behavior during creep deformation and its contribution to the creep deformation in order to understand and therefore improve our ability to optimize this material.

In this chapter, observations of mechanical twinning behavior during creep and some contributions of mechanical twinning to creep deformation in near- γ TiAl are presented. The results are analyzed based on the twin nucleation and propagation theory proposed in the previous chapters and in terms of a maximum resolved shear stress criterion for mechanical twinning proposed in this chapter.

5.2. Material and Experimental Procedure

The creep specimens were produced and machined at Howmet Corp., Whitehall, Michigan. Investment cast test bars, 16 mm in diameter and 125 mm long, were HIP'ed before specimens with 25 mm gage length and 5 mm diameter were machined from the bars. After HIP'ing, the test bars were heat treated at 1300 °C for 20 hrs in Ar

atmosphere, and cooled at 65 °C/min in argon to produce the equiaxed + lamellar microstructure. The nominal composition was Ti-48Al-2Nb-2Cr atomic percent.

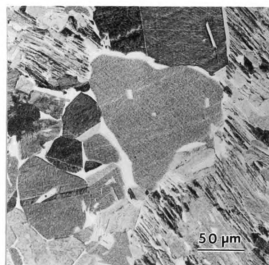
A constant stress test and a multi-stress drop test were conducted at 765 °C in air. A constant stress creep test at 176 MPa was interrupted at 4% strain, near the end of primary creep. The multi-stress drop test started at 276 MPa and the stress was dropped in increments to a final stress of 103 MPa at about 20% strain. The specimens were furnace cooled to room temperature while maintaining the final stresses. The temperature difference between the two ends of the specimens was less than 3 °C.

Microstructural investigation on the specimens before and after deformation was carried out using optical and transmission electron microscopy. Specimens for optical microstructure were prepared by making longitudinal sections from the deformed specimens and the original bars. The specimens were etched using Kroll's reagent to view grain structures after the specimens were ground and polished. For TEM investigation, however, 0.7 mm thick slices were cut in both longitudinal and transverse directions from deformed and undeformed samples. 3 mm diameter disks were cut from the slices using an ultrasonic cutting machine and ground to about 0.1 mm thick. The disks were finally thinned in a double jets electropolishing system using a 10% sulfuric acid + methanol solution at 20 °C. The TEM investigation was performed on a HITACHI H800 transmission electron microscope with an accelerating voltage of 200 kV.

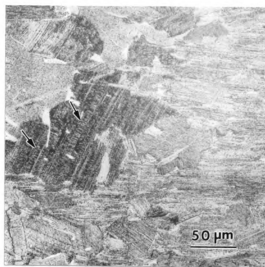
5.3. Results

5.3.1. Optical Microstructure

The initial microstructure after heat treatment was a duplex structure with $(\gamma + \alpha_2)$ lamellar colonies and equiaxed γ grains, as shown in Fig. 5.1 (a). After creep



(a)



(b)

Figure 5.1 - Optical microstructures (a) before creep deformation and (b) after creep deformation.

deformation, cross twinning configurations were observed within lamellar colonies as indicated by the arrows in Fig. 5.1 (b). One possible form of mechanical twinning occurs parallel to the existing lamellar interfaces, which is denoted as "parallel twinning"

hereafter. But it is difficult to distinguish parallel twins from original lamellae from their images since both have the same image characteristics.

5.3.2. Cross Twinning and Parallel Twinning in Lamellar Grains

The investigation in lamellar grains exhibited many cross twinning configurations. The cross twinning was found to occur when two differently oriented lamellae meet and either or both of the lamellae are oriented in such directions that twinning occurs parallel to the lamellar interfaces, as shown in Fig. 5.2 (a). Lamellar orientations with respect to the tensile axis were determined. For the inclined lamellae in Fig. 5.2 (a), the interfaces were tilted 42° from the tensile axis. For the vertical lamellae, lamellar interfaces are tilted 5° away from the tensile axis. Many similar configurations were found in the multi-stress-jump creep specimen.

At the intersection region of two lamellae in Fig. 5.2, many relatively fine twins were formed. Investigating the coarse lamellae that are located away from the intersection region, the orientation relationship between the two lamellae has true-twin relationship, as shown in Fig. 5.2 (b). For convenience, we denote "Lamellae 1" to the inclined lamellae and "Lamellae 2" to the vertical lamellae in the following. These two sets of lamellae are indexed in Fig. 5.2 (c) by taking the γ phase matrix as a reference orientation and the indices are referred to γ laths in lamellae. Therefore, the interfaces of Lamellae 1 are $(111)_1$ (subscription 1 indicating Lamellae 1); the interfaces of Lamellae 2 are $(1\bar{1}1)_2$; and the intersection axis of two lamellar sets is perpendicular to the page and in the $[1\bar{1}0]$ direction, as shown in Fig. 5.2 (c).



(a)

Figure 5.2 - (a) Cross twinning configuration in a lamellar grain, (b) diffraction pattern of the original lamellae, and (c) orientations of the original lamellae.

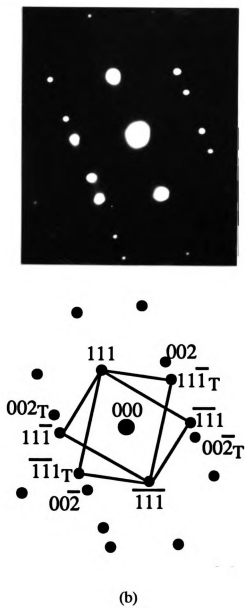


(Figure 5.2 continued)

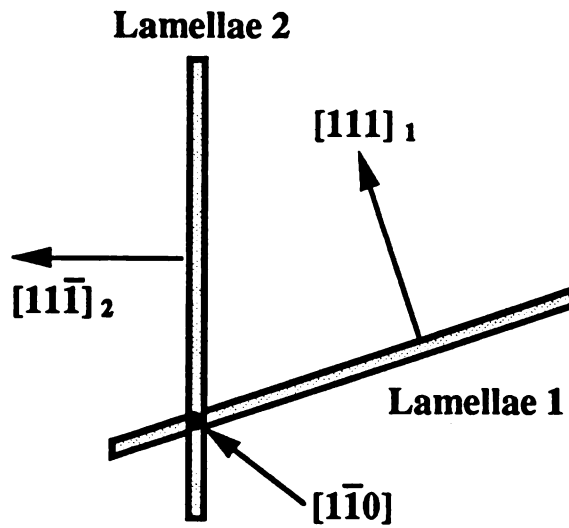


(Figure 5.2 continued)

The cross twinning configurations shown in Fig. 5.3 is a different situation from that described above. The cross twinning in Fig. 5.3 were formed in an equiaxed γ grain, and both approximately vertically oriented twins and slightly inclined twins were formed during creep deformation, which will be verified later.

5.3.3. Fine Mechanical Twins at Grain Triple Points

In the specimen deformed to a strain close to the end of primary creep, we found that very fine mechanical twins frequently formed at equiaxed γ grain triple points. Fig. 5.4 shows that these fine mechanical twins formed at the grain triple points within an equiaxed γ grain, as indicated by letters A, B and C. The thickness of the fine twins in Fig. 5.5 (a) is about 50 nm. These fine mechanical twins are much thinner than typical



Figure 5.3 - Cross twinning configuration within a large equiaxed γ grain.

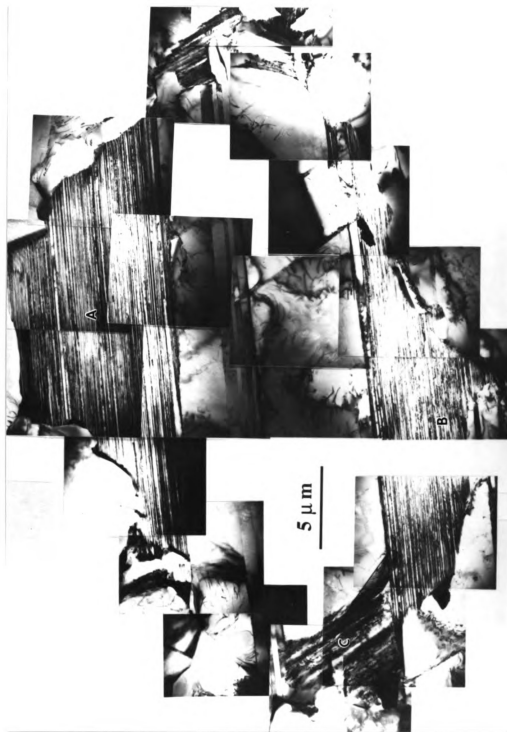


Figure 5.4 - Fine mechanical twin configurations at equiaxed γ grain triple points.

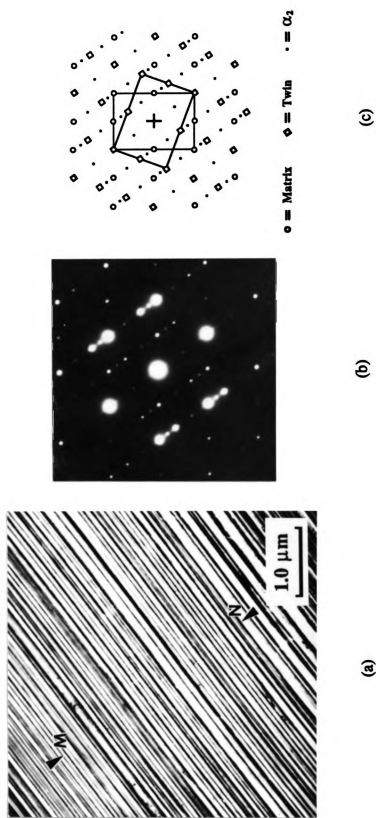


Figure 5.5 - Fine mechanical twins (a), diffraction pattern across several fine twin interfaces (b), and twin relation in the diffraction pattern (c).

lamellar laths that form in phase transformation ^[22]. The diffraction pattern across these fine mechanical twins is shown in Fig. 5.5 (b) and (c). Fig. 5.5 (c) is a schematic drawing of the diffraction pattern of Fig. 5.5 (b). The open circles in Fig. 5.5 (c) are the diffraction spots from the γ matrix, and the rhombuses are the twin spots. In addition to these two spot sets, there also exist very faint spots in Fig. 5.5 (b), which are designated by dots in Fig. 5.5 (c). This set of diffraction spots represents the DO_{19} crystal structure. This result indicates that two crystal structures exist in Fig. 5.5 (a): one is twin related γ phase layers (the fine mechanical twins and the untwinned matrix), and the other is fine DO_{19} structure layers. The locations of these DO_{19} structure layers are not known in this case. These fine lath configurations will be called fine mechanical twins in this study.

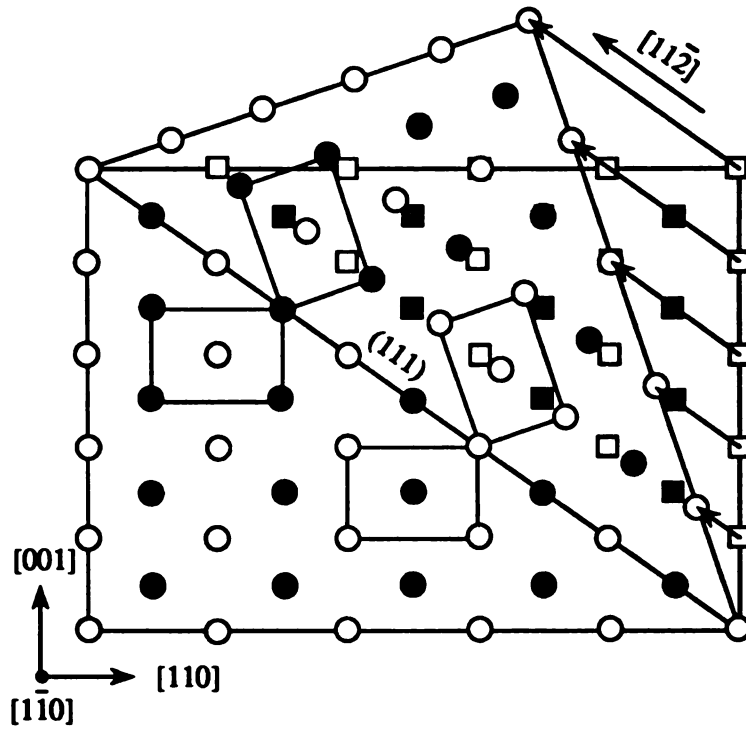
5.4. Analysis and Discussion

5.4.1. Cross Twinning in Lamellar Grains

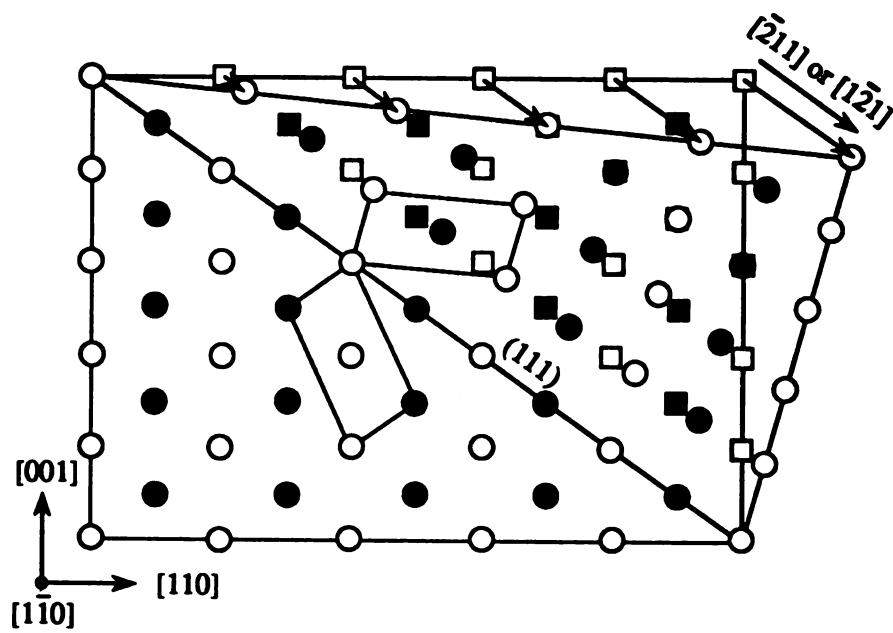
If we look at a γ/γ lamellar interface, there exist six possible orientation relationships between the two adjacent γ lamellae that can be described in terms of $\langle 110 \rangle$ directions ^[158,159]. Among these six relations there are two kinds of twin relationships: if $[\bar{1}10]$ directions in two γ laths are anti-parallel to one another in the lamellar interface, these two adjacent γ lamellae have a $\{111\}\langle 11\bar{2} \rangle$ true-twin relationship; if $[\bar{1}10]$ direction in one γ lath is anti-parallel to $[0\bar{1}1]$ or $[10\bar{1}]$ direction in an adjacent γ lath, a pseudo-twin will form ^[158,159].

In a cast and heat treated specimen, the γ/γ lamellar interfaces with a $\{111\} \langle \bar{1}1\bar{2} \rangle$ true-twin relationship are more favored than those with a pseudo-twin relationship, since true-twin relation has lower interface energy and is thermodynamically preferred during solidification and phase transformation. Fig. 5.6 shows interface structures of a true-twin in (a) and a pseudo-twin in (b). In Fig. 5.6 (a), the interface is a $\Sigma 3$ boundary with a (111) boundary plane, and two laths are fully symmetric in the boundary plane (111). The interface of pseudo-twin in Fig. 5.6 (b) is a $\Sigma 6$ boundary, that is, only atoms of every second (111) plane are in completely symmetrical locations with respect to the boundary plane (111), while atoms of other (111) planes are in anti-symmetric positions, in which perfect symmetric sites are occupied by atoms of different type. This even Σ boundary contains antiphase boundary elements ^[160]. Therefore, the energy of lamellar interfaces with pseudo-twin relation is higher than those with true-twin relation. This is consistent with our observations. We found that original lamellae had true-twin relationship in the specimens investigated, as shown in Fig. 5.2 (b).

For mechanical twinning, there are the same kinds of configurations as analyzed above. General twinning systems in γ phase are in the form of $\{111\} \langle \bar{1}1\bar{2} \rangle$, the same as for disordered fcc crystals. However, because of its anisotropic crystal structure, the different twinning systems result in either true-twins or pseudo-twins during deformation. If the twinning shear occurs in the direction of $[\bar{1}1\bar{2}]$ on a (111) plane, the deformed crystal will be exactly symmetric to the undeformed crystal with respect to the (111) twin plane, which is a true-twin, as in Fig. 5.6 (a). If a crystal is deformed by either of (111) $[\bar{2}11]$ or (111) $[\bar{1}2\bar{1}]$, the result will be a pseudo-twin, as shown in Fig. 5.6 (b). In



(a)



(b)

Figure 5.6 - Atomic arrangement of true twinning (a) and pseudo twinning (b).

order to understand the twinning behavior in the larger strain creep specimen, the possible twinning systems in Fig. 5.2 (a) are plotted in a stereographic projection along $[\bar{1}\bar{1}0]$ direction by considering the tensile axis orientation, as shown in Fig. 5.7, where the twinning system is assumed to be the $\{111\}\langle\bar{1}\bar{1}2\rangle$ type. A resolved shear stress on each twinning system in Fig. 5.7 is considered to determine the probable twinning systems in this particular orientation. Table 5.1 shows the computed Schmid factors for these possible twinning systems, where ϕ is the angle between the tensile axis and the normal to the twin plane, λ is the angle between the tensile axis and the twinning direction. In Lamellae 1, both $(111)[\bar{2}11]$ and $(111)[\bar{1}\bar{2}1]$ have relatively large Schmid factors, and are more likely to operate during creep deformation. In lamellae 2, all Schmid factors are small, so twinning is less likely. Therefore, the mechanical twins in Fig. 5.2 (a) are formed by operating either $(111)[\bar{2}11]$ or $(111)[\bar{1}\bar{2}1]$ or both twinning systems in lamellae 1. The mechanical twins in this case are pseudo-twins, and they were clearly formed during creep deformation, since this kind of twinning is not observed in undeformed specimens.

Since these pseudo-twins are not thermodynamically favored, an interfacial energy criterion of mechanical twinning is unsuitable in this case. A maximum resolved shear stress criterion for mechanical twinning is appropriate. This criterion is that mechanical twinning operates in the twinning system with the highest resolved shear stress. However, if the maximum resolved shear stress is less than a certain critical value, the interfacial energy criterion may play a role.

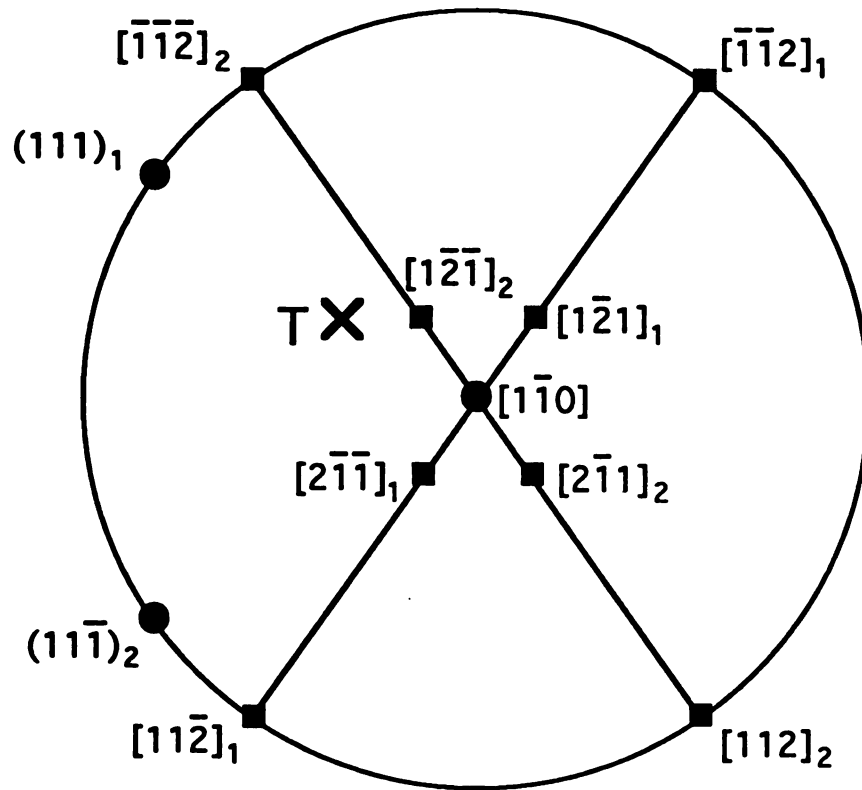


Figure 5.7 - Stereographic projection of possible twinning systems along $[1\bar{1}0]$ direction.

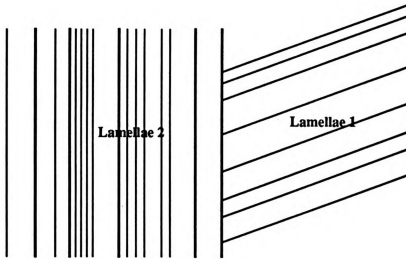
Table 5.1. Schmid Factors for Mechanical Twinning Systems in Lamellae 1 and Lamellae 2.

Lamellae 1			
$(111) \langle 112 \rangle$	ϕ	λ	$\cos\phi\cos\lambda$
$(111)[1\bar{1}2]$	48°	84°	0.070
$(111)[2\bar{1}\bar{1}]$	48°	45°	0.473*
$(111)[1\bar{2}1]$	48°	52°	0.412*
$(111)[\bar{1}\bar{1}2]$	48°	96°	-0.070

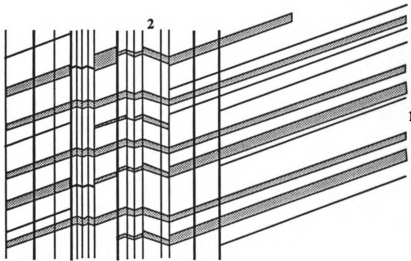
Lamellae 2			
$(111) \langle 112 \rangle$	ϕ	λ	$\cos\phi\cos\lambda$
$(1\bar{1}\bar{1})[\bar{1}\bar{1}2]$	85°	53°	0.052
$(1\bar{1}\bar{1})[1\bar{2}\bar{1}]$	85°	20°	0.082
$(1\bar{1}\bar{1})[2\bar{1}\bar{1}]$	85°	66°	0.035
$(1\bar{1}\bar{1})[112]$	85°	127°	-0.052

* Probable twinning system

Fig. 5.8 schematically shows the formation of cross twins in Fig. 5.2 (a) according to the maximum resolved shear stress criterion. Fig. 5.8 (a) is a starting situation before twinning. Fig. 5.8 (b) is a metastable situation showing growth of mechanical twins in lamellae 1 into lamellae 2. To accommodate this growth, mechanical twinning on the other twinning system with a high Schmid factor is needed as shown in Fig. 5.8 (c). Most thick twins can easily traverse through existing thin

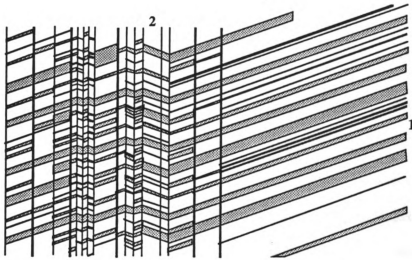


(a)



(b)

Figure 5.8 - Schematic mode of cross twinning: (a) initial condition of two lamellae; (b) metastable condition of twinning in lamellae 1; (c) final configuration of cross twins as seen in Fig. 5.2 (a).



(c)

(Figure 5.8 continued)

vertical twins. Therefore, mechanical twinning in Fig. 5.2 (a) occurred in the inclined lamellar colony parallel to the lamellar interfaces and across the vertical lamellar colony by twinning shear in $(111)[\bar{2}11]$ and $(111)[\bar{1}21]$ systems. Therefore, this is a parallel twinning with respect to the inclined lamellae, but it is also a cross twinning with respect to the vertical lamellar colony.

In Fig. 5.2 (a) the inclined lamellar laths become finer after twinning. This indicates that extensive mechanical twinning occurred during creep deformation in this lamellae. But vertical lamellar laths are unchanged. This is because the inclined

lamellar laths of Lamellae 1 contain two possible twinning systems having the highest Schmid factor and the vertical lamellar laths of Lamellae 2 do not have high Schmid factor twinning systems. This is consistent with the maximum resolved shear stress criterion.

5.4.2. Cross Twinning in Equiaxed γ Grains

The cross twinning configuration in Fig. 5.3 shows a different situation than that in Fig. 5.2 (a). In the case of Fig. 5.3, the cross twins were formed in an equiaxed γ grain, and both approximately vertically oriented twins and slightly inclined twins are formed during creep deformation, which is easily verified by carefully investigating the twinning sequence of these two sets of mechanical twins. The inclined twins are sheared by the formation of vertical twins at their intersections. This indicates that the inclined twins formed before the vertical twins. However, the inclined twins are tapered as they grow into the grain interior, which means that these twins are formed by the twinning mechanism described in chapter three. A possible scenario for this sequence is as follows: The inclined twins were first formed due to a local stress concentration, and the vertical twins were generated by the operation of twinning system with a maximum resolved shear stress resulting from the external tensile creep stress ^[28].

Comparing our result with others ^[22,39] indicates that mechanical twinning is playing an important role in creep deformation at the combination of stress and temperature. Mechanical twinning reduces a stress concentration so as to maintain strain continuity. There may be a twinning transition temperature, below which mechanical

twinning occurs. In Loiseau and Lasalmonie's study ^[22], the transition temperature is about 800 °C for a complete equiaxed single γ phase. But this transition temperature may change depending upon the composition and microstructure. Our observations of mechanical twinning in creep specimens are consistent with Loiseau and Lasalmonie's result where the equiaxed γ grain structure was investigated. In Huang and Kim's study ^[39], the material was in the two phase $\gamma + \alpha_2$ lamellar condition; the mechanical twinning did not operate, possibly due to the deformation temperature higher than the twinning transition temperature. At high temperature, since dislocations are much more mobile and some cube $\langle 100 \rangle$ dislocations become mobile, mechanical twinning is less favorable than that at temperatures below the twinning transition temperature.

5.4.3. Fine Mechanical Twins at Equiaxed γ Grain Triple Points

(a) Fine Mechanical Twins Formed by Accommodation of Stress Concentration at Equiaxed γ Grain Triple Points

Comparing a crystal orientation in the untwinned area with that in the fine twin region, we found that the matrix orientation in the fine mechanical twin region in Fig. 5.4 was exactly the orientation of the untwinned area. This suggests that the fine mechanical twins are formed by deforming the γ phase. This is also evident in the configuration of the fine mechanical twins growing toward the γ phase grain interior, which is located between the fine twin region and the untwinned region as indicated by arrows in Fig. 5.4.

The configurations of twinning accommodation of stress concentrations at equiaxed γ grain triple points were also occasionally found in the specimens before creep deformation. However, these accommodation twins are widely spaced compared to the fine mechanical twins in crept specimens. These accommodation twins at the grain triple points in the specimens before creep deformation are probably formed either by the previous HIP'ing process or by the heat treatment or both. The deformation mechanisms in HIP'ing process are similar to the creep deformation mechanisms, for example, the grain boundary sliding and the diffusion accommodated deformation^[161]. Therefore, the stress concentration at the grain triple points during HIP'ing process is probable. Since the cooling rate after heat treatment is relatively fast (65 °C/min), the thermal stress concentration at equiaxed γ grain triple points is also possible due to the anisotropic thermal contraction in γ phase. However, the stress concentration formed during the HIP'ing or the cooling could not result in so intensive twinning as observed in the crept specimens. The shear displacement along the twin interfaces between two points "M" and "N" in Fig. 5.5 (a) is calculated to be 1.18 μm . Such a large displacement could not be caused by the thermal stress arising from the thermal contraction mismatch. The observed fine mechanical twins at equiaxed γ grain triple points in this study are probably formed either by refining the largely spaced accommodation twins existing in the specimens before creep deformation, or by twinning in untwinned grains due to local stress concentrations at equiaxed γ grain triple points during creep deformation.

(b) Formation of Fine Mechanical Twins Prevents Grain Boundary Sliding

Fig. 5.9 is an another example of fine mechanical twins formed at an equiaxed

γ grain triple point. These fine mechanical twins formed to accommodate the stress concentration caused by grain boundary sliding and/or the deformation of adjacent equiaxed γ grains at the grain triple point (Fig. 5.9 (a)). However, this accommodation twinning caused the grain boundaries to become zigzagged instead of smooth (Fig. 5.9 (b)). The presence of curled dislocations in the untwinned neighbor equiaxed γ grain suggests that subsequent creep deformation occurred by dislocation slip in the untwinned equiaxed γ grain interior near the zigzagged boundaries (Fig. 5.9 (c)). All three of the grain boundaries that form the equiaxed γ grain triple point in Fig. 5.9 (a) are large angle grain boundaries. The grain orientation relationships and boundary structures of these three grains (designated as grain I, II, III in Fig. 5.9 (a)) were determined and are shown in table 5.2. The nearest coincidence boundary and the deviation from this boundary are indicated. The fact that these boundaries are high angle, and not low energy special boundaries, indicates that grain boundary sliding would have been relatively easy ^[162]. These grain boundaries were smooth before twinning since they were equiaxed γ grain boundaries, which can be seen if one looks at the same grain boundary in untwinned region.

Table 5.2. Misorientation and Grain Boundary Structure of Grains at the Grain Triple Point.

Grain boundary	I/II	II/III	III/I
Misorientation	$[\bar{1}20]/45^\circ$	$[164]/150^\circ$	$[\bar{3}11]/132^\circ$
Boundary structure	3° from $\Sigma 15$	7° from $\Sigma 33_b$	7° from $\Sigma 31_b$

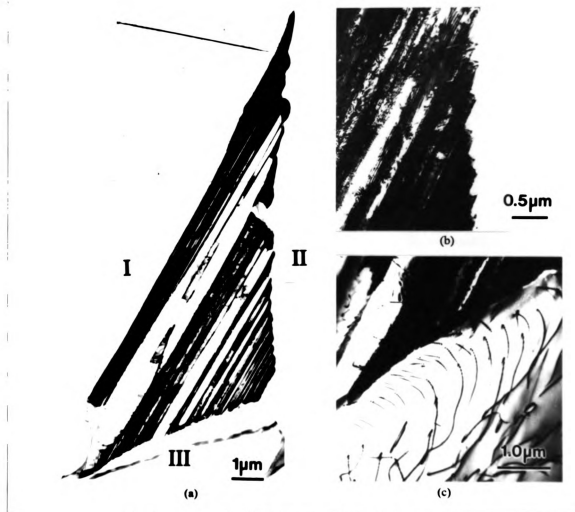


Figure 5.9 - Fine mechanical twins from accommodation of local stress concentration (a), twin end configuration at equiaxed γ grain boundary (b), and dislocation slip near the zigzagged boundary (c).

The zigzagged grain boundary resulting from mechanical twinning is much different from the serrated lamellar grain boundary in their morphology. The "serrations" of the zigzagged grain boundary formed by mechanical twinning are regularly distributed along the trace of the previous equiaxed γ grain boundary, and the "serrations" are small, as shown in Fig. 5.9 (b). However, the typical lamellar grain boundary, the boundary between an equiaxed γ grain and a lamellar grain or the boundary between two lamellar grains, formed from phase transformation, are roughly serrated, and the "serrations" are large and irregular, as shown in Fig. 5.10 and 5.11.

(c) On DO_{19} Crystal Structure in Fine Mechanical Twins

The twinning mechanism in TiAl observed in this study is a homogeneous shear of a crystal by the glide of $1/6 \langle 11\bar{2} \rangle$ twinning dislocations on every (111) close packed plane. However, if the stress concentration at the grain triple points and/or grain boundaries was such that it did not create $1/6 \langle 11\bar{2} \rangle$ twinning dislocations on every (111) plane, four atomic layers of DO_{19} structure, i.e., a nucleus of the Ti_3Al crystal structure, could be formed by glide of a $1/6 \langle 11\bar{2} \rangle$ twinning dislocation on a (111) plane ^[65]. In addition to this, the crystal structure across the true-twin plane in TiAl is also a three atomic layer DO_{19} structure. Therefore, the occurrence of DO_{19} diffraction spots with the twin related TiAl diffraction spots in the diffraction pattern in Fig. 5.5 (b) is reasonable. It is worth noting that such a uniformly distributed thin lath configuration in Fig. 5.5 (a) is very difficult to form through the phase transformation such as $\alpha_2 \rightarrow \alpha_2 + \gamma$ or $\alpha \rightarrow \alpha_2 + \gamma$. Such a thin new phase layer, γ phase in this case, could not be thermodynamically stable in the case of phase transformation, and therefore, the thin γ

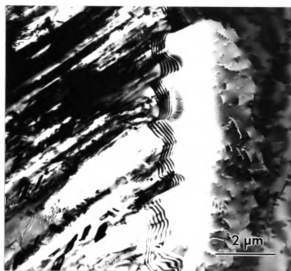


Figure 5.10 - Boundary between an equiaxed γ grain and a lamellar grain.

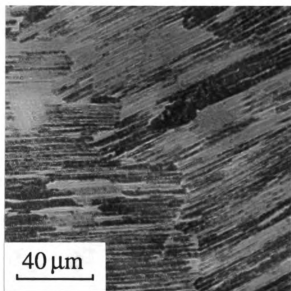


Figure 5.11 - Optical microstructure showing the roughness of lamellar grain boundary.

phase layer should either grow and become thicker or be eliminated by growth of the adjacent γ laths. The resultant configuration should be the lamellae containing coarse γ laths with different thickness. The observation of fine twin configurations only near the equiaxed γ grain triple points in this study also provides an evidence that the fine mechanical twins are formed due to the local stress concentration at the equiaxed γ grain triple points but not by the phase transformation.

5.5. Conclusions

1. Mechanical twinning is an important deformation mechanism in creep deformation of TiAl intermetallic compound.
2. An energetic criterion is not suitable for mechanical twinning in this study. Above a certain value of stress (at constant temperature), the twinning transition stress is apparently temperature dependent.
3. Mechanical twins are formed by either true-twinning or pseudo-twinning. The formation of mechanical twins during the creep deformation of TiAl follows the maximum resolved shear stress criterion.
4. The mechanical twins observed in this study are propagated by homogeneous glide of $1/6\langle 11\bar{2} \rangle$ twinning dislocations on every close packed (111) plane, that is, by a homogeneous shearing mechanism.

5. The stress concentration at the grain triple points can be accommodated by the formation of fine mechanical twins. The zigzagged grain boundaries formed by mechanical twinning can inhibit grain boundary sliding. The formation of fine mechanical twins is probably controlled more by the local stress concentration than by an externally applied stress.

CHAPTER SIX

CONCLUDING REMARKS AND RECOMMENDED FUTURE WORK

The *in situ* investigations of mechanical twin nucleation and propagation presented here have demonstrated that mechanical twin nucleates by bowing out of twinning dislocations at grain boundaries due to the local stress concentration and propagates by continuous emission of twinning dislocations from the grain boundaries and glide of twinning dislocations on every adjacent twinning plane. The nucleus of true-twinning is found to be either a superlattice intrinsic stacking fault (SISF) in the case that one $1/6[11\bar{2}]$ twinning dislocation is emitted from the grain boundaries in a (111) plane, or a superlattice extrinsic stacking fault (SESF) when two $1/6[11\bar{2}]$ twinning dislocations are emitted from the grain boundaries in two adjacent (111) planes. The mechanical twin propagation observed in this study occurs by trailing twinning dislocations pushing leading twinning dislocations in the twin layer.

The stress analysis on a thin twin layer has shown that the stress distribution along the thin twin layer is not even. The changes of forward stress and back stress are similar. The magnitudes of forward stress and back stress are very large near the twin tip and drop very quickly as the distance from the twin tip increases. At very large

distance from the twin tip, the stress changes are very small and both stresses tend to become constant. The calculation of external stress has shown that the magnitude of external stress is small and evenly distributed along the thin twin layer investigated. The external stress has been identified as a residual stress within the grain where the thin twin layer is located. The result of stress analysis indicates that the trailing twinning dislocations glide forward more easily in the twin layer than the leading twinning dislocations. This result is consistent with the experimental observation of the trailing dislocation pushing the leading dislocation phenomenon.

The formation of various mechanical twin configurations observed in creep deformed specimens has been well understood, and interpreted using the twinning mechanism identified and the maximum resolved shear stress criterion proposed in this study. The cross twinning occurs when two differently oriented lamellar colonies meet in such a way that one lamellar colony with a larger Schmid factor generates twins across the other one. However, the cross twinning configurations are also observed in the large equiaxed γ grains: one set of twins, which initiate at grain boundaries, are formed due to the local stress concentration and the other set of twins, which cross the first set of twins, are formed by the external loading. Analysis of the cross twinning in the lamellar colonies indicates that an energetic criterion for mechanical twinning is not suitable in this study, and the pseudo-twinning obeys the maximum resolved shear stress criterion. The fine mechanical twins at the equiaxed γ grain triple points are due to the accommodation of local stress concentration during the creep deformation.

to fully understand the mechanical twinning and creep deformation in TiAl:

1. Correlations between mechanical twinning and creep deformation in TiAl, or the role of mechanical twinning in the creep deformation of TiAl.
2. What type of grain boundary structure is preferred for mechanical twin nucleation at the grain boundary.
3. Investigation of creep deformed single crystal TiAl in which the Schmid law can be precisely applied.

LIST OF REFERENCES

LIST OF REFERENCES

- [1] H.A. Lipsitt, D. Schechtman, and R.E. Schafik, *Metall. Trans. A*, 6A (1975), 1991.
- [2] T. Kawabata, T. Kanai, and O. Izumi, *Acta metall.*, 33 (1985), 1355.
- [3] S.C. Huang, *Scripta Metall.*, 22 (1987), 1985.
- [4] D. Schechtman, M.J. Blackburn, and H.A. Lipsitt, *Metall. Trans.*, 5 (1974), 1373.
- [5] G. Hug, A. Loiseau, and A. Lasalmone, *Phil. Mag. A*, 54 (1986), 47.
- [6] G. Hug, A. Loiseau, and P. Veyssiere, *Phil. Mag.*, 57 (1988), 499.
- [7] S.A. Court, V.K. Vasudevan, and H.L. Fraser, *Phil. Mag. A*, 61 (1990), 141.
- [8] S.H. Whang and Y.D. Hahn, *Scripta Metall.*, 24 (1990), 485.
- [9] B.A. Greenberg, O.V. Antonova, V.N. Indenbaum, L.A. Karkina, A.B. Notkin, M.V. Ponomarev, and L.V. Smirnov, *Acta Metall.*, 39 (1991), 233.
- [10] B.A. Greenberg, O.V. Antonova, L.A. Karkina, A.B. Notkin, and M.V. Ponomarev, *Acta Metall.*, 40 (1992), 815.
- [11] S.C. Huang and E.L. Hall, *Metall. Trans. A*, 22 (1991), 427.
- [12] S.C. Huang and E.L. Hall, *Scripta Metall.*, 25 (1991), 1805.
- [13] V.K. Vasudevan, M.A. Stucke, S.A. Court, and H.L. Fraser, *Phil. Mag. Lett.*, 59 (1989), 299.

- [14] H. Inui, A. Nakamura, M.H. Oh, and M. Yamaguchi, *Phil. Mag. A*, 66 (1992), 557.
- [15] M.A. Morris, *Phil. Mag. A*, 68 (1993), 237.
- [16] M.A. Morris, *Phil. Mag. A*, 68 (1993), 259.
- [17] M. Hirabayashi and S. Weissmann, *Acta Metall.*, 10 (1962), 25.
- [18] B. Hanssom and R.S. Barnes, *Acta Metall.*, 12 (1965), 315.
- [19] V. Krasevec, P. Delavignette, and S. Amelinckx, *Mater. Res. Bull.*, 2 (1967), 1029.
- [20] V.I. Syutkin and E.S. Yakovleva, *Physica Status Solidi*, 21 (1967), 465.
- [21] D.W. Pashley, J.L. Robertson, and M.J. Stowell, *Phil. Mag.*, A19 (1969), 83.
- [22] A. Loiseau and A. Lasalmonie, *Mater. Sci. Eng.*, 67 (1984), 163.
- [23] C.R. Feng, D.J. Michel, and C.R. Crowe, *Scripta Metall.*, 22 (1988), 1481.
- [24] M.H. Yoo, C.L. Fu, and J.K. Lee, DE89-014779, 1989,
- [25] M.H. Yoo, C.L. Fu, and J.K. Lee, *J. Phys. III*, 1 (1991), 1065-1084.
- [26] G.T. Gray III, *Microstructure/Property Relationships in Titanium Aluminides and Alloys*, ed. by Young-Won (Y-W) Kim and Rodney R. Boyer (TMS Publications, 1991), p263.
- [27] H. Inui, A. Nakamura, M.H. Oh, and M. Yamaguchi, *Phil. Mag. A*, 66 (1992), 557.
- [28] Z. Jin and T.R. Bieler, *Scripta Metall.*, 27 (1992), 1301.
- [29] Z. Jin and T.R. Bieler, *High-Temperature Ordered Intermetallic Alloys V*, ed. by I. Baker, R. Darolia, J.D. Whittenberger, and M.H. Yoo (MRS, Pittsburgh, PA, 1993), Vol. 288, p. 775.

- [30] Z. Jin, R. Beals, and T.R. Bielar, *Structural Intermetallics*, ed. by R. Darolia et al. (A Publication of TMS, Warrendale, PA, 1993), p. 275.
- [31] Z. Jin and T.R. Bieler, *Twinning in Advanced Materials*, ed. by M.H. Yoo and M. Wuttig (A Publication of TMS, Warrendale, PA, 1994), in press.
- [32] S. Farenc, A. Coujou, and A. Couret, *Phil. Mag. A*, 67 (1993), 127-142.
- [33] S. Wardle, I. Phan, and G. Hug, *Phil. Mag. A*, 67 (1993), 497-514.
- [34] Y.Q. Sun, P.M. Hazzledine, and J.W. Christian, *Phil. Mag. A*, 68 (1993), 471-494.
- [35] Y.Q. Sun, P.M. Hazzledine, and J.W. Christian, *Phil. Mag. A*, 68 (1993), 495-516.
- [36] M. Yamaguchi and H. Inui, *Structural Intermetallics*, eds. by R. Darolia, J.J. Lewandowski, C.T. Liu, P.L. Martin, D.B. Miracle, and M.V. Nathal (A Publication of TMS, Warrendale, PA, 1993), p127.
- [37] D.A. Wheeler, B. London, and D.E. Larsen, Jr., *Scripta Metall.*, 26 (1992), 939.
- [38] P.L. Martin, M.G. Mendiratta, and H.A. Lipsitt, *Metall. Trans.*, 14A (1983), 2170.
- [39] J.S. Huang and Y-W. Kim, *Scripta Metall.*, 25 (1991), 1901.
- [40] M. Yamaguchi, S.R. Nishitani and Y. Shirai, in *Proc. on "High Temperature Aluminides & Intermetallics"*, eds by S.H. Whang, C.T. Liu, D.P. Pope and J.O. Stiegler, TMS, 1990, p63.
- [41] R.W. Hayes and B. London, *Acta Metall.*, 40 (1992), 2167.
- [42] K.I. Ouchi, Y. Iijima, and K.I. Hirano, in the *Proc. of Titanium '80 - Science and Technology*, ed. H. Kimura and O. Izumi (The Metallurgical Society of AIME, 1980),

559.

- [43] S.L. Kampe, J.D. Bryant, and L. Christodoulou, *Met. Trans.*, 22A (1991), 447.
- [44] P.L. Martin et al., in the *Proc. of Creep And Fracture of Engineering Materials And Structures*, ed. B. Wilshire and R.W. Evans (The Institute of Metals, London, 1990), 265.
- [45] S.C. Cheng, J. Wolfenstine, and O.D. Sherby, *Met. Trans.*, 23A (1992), 1509.
- [46] H. Oikawa, in the *Proc. of High Temperature Aluminides & Intermetallics*, ed. S.H. Whang, C.T. Liu, D.P. Pope and J.O. Stiegler, TMS, 1990, p353.
- [47] H.R. Ogden, D.J. Maykuth, W.L. Finlay and R.I. Jaffee, *Trans. AIME*, 191 (1951), 1150.
- [48] D. Clark et al., *J. Institute of Metals*, 91 (1962-1963), 197.
- [49] J.L. Murray, *Binary Alloy Phase Diagrams*, ed. T.B. Massalski, ASM, Metals Park, OH, 1986, p173.
- [50] E.S. Bumps, H.D. Kessler and M. Hansen, *Trans. AIME*, 194 (1952), 609.
- [51] P. Duwez and J.L. Taylor, *JOM*, January, 1952, p70.
- [52] S.C. Huang, E.L. Hall and M.F.X. Gigliotti, *High Temperature Ordered Intermetallic Alloys II*, ed. N.S. Stoloff, C.C. Koch, C.T. Liu and O. Izumi, Mrs, Pittsburgh, PA, 1987, p481.
- [53] R.P. Elliott and W. Rostoker, *Acta. Met.*, 2 (1954), 884.
- [54] B.A. Greenberg, *Phys. Status Sol.*, B55 (1973), 59.
- [55] T. Kawabata and O. Izumi, *Scripta Metall.*, 21 (1987), 433.
- [56] S.H. Whang and Y.D. Hahn, *Scripta Metall.*, 24 (1990), 1679.
- [57] B.A. Greenberg, *Phys. Stat. Sol.*, 42 (1970), 459.

- [58] B.A. Greenberg and L.I. Yakovenkova, *Phys. Stat. Sol.*, 18A (1973), K129.
- [59] V.N. Indenbaum, et al., *Physics Metals Metallogr.*, 59 (1985), 52.
- [60] B.A. Greenberg and Yu.N. Gornostirev, *Scripta Metall.*, 22 (1988), 853.
- [61] G. Hug. A. Loiseau and P. Veyssiere, *Revue Phys. Appl.*, 23 (1988), 673.
- [62] C. McCullough, et al., *Scripta Metall.*, 22 (1988), 1131.
- [63] J.J. Valencia, et al., *Scripta Metall.*, 21 (1987), 1341.
- [64] Y.S. Yang and S.K. Wu, *Scripta Metall.*, 24 (1990), 1801.
- [65] M.J. Blackburn, *The Science, Technology and Application of Titanium*, ed. R.T. Jaffee and N.E. Promisel, Pergamon Press, London, 1970, p633.
- [66] P. Mukhopadhyay, *Metallography*, 12 (1979), 119.
- [67] R.W. Cahn, *Advanc. Phys.*, 3 (1954), 363.
- [68] B.A. Bilby and A.G. Crocker, *Proc. Roy. Soc. A*, 288 (1965), 240-255.
- [69] M. Bevis and A.G. Crocker, *Proc. Roy. Soc. A*, 313 (1969), 509-529.
- [70] M. Bevis and A.G. Crocker, *Proc. Roy. Soc. A*, 304 (1968), 123-134.
- [71] E. Schmid and W. Boas, *Plasticity of Crystals*, (London: Hughes, 1950).
- [72] E.O. Hall, *Twinning and Diffusionless Transformations in Metals*, (London: Butterworths, 1954).
- [73] H. Kiho, *J. Phys. Soc. Japan*, 9 (1954), 739.
- [74] H. Kiho, *J. Phys. Soc. Japan*, 13 (1958), 269.
- [75] M.A. Jaswon and D.B. Dove, *Acta Crystallogr.*, 9 (1956), 621.
- [76] M.A. Jaswon and D.B. Dove, *Acta Crystallogr.*, 10 (1957), 14.
- [77] M.A. Jaswon and D.B. Dove, *Acta Crystallogr.*, 13 (1960), 232.
- [78] F. Laves, *Naturwissenschaften*, 39 (1952), 546.

- [79] D.E. Mikkola and J.B. Cohen, *Acta Metall.*, 14 (1966), 105.
- [80] A. Guimier and J.L. Strudel, in *Proc. 2nd Int. Conf. Strength of Metals and Alloys* (ASM, Metals Part, OH, 1970), Vol. 3, p1145.
- [81] B.H. Kear, J.M. Oblak, and A.F. Giamei, *ibid.*, p1155.
- [82] S.B. Chakraborty and E.A. Starke, Jr., *Acta Metall.*, 23 (1975), 63.
- [83] G.F. Bolling and R.H. Richman, *Acta Metall.*, 13 (1965), 709.
- [84] J.P. Kubin and J.V. Rieu, *Scripta Metall.*, 12 (1978), 927.
- [85] M.L. Green and M. Cohen, *Acta Metall.*, 27 (1979), 1523.
- [86] E. Goo, T. Duerig, K. Melton, and R. Sinclair, *Acta Metall.*, 33 (1985), 1725.
- [87] R.W. Cahn and J.A. Coll, *Acta Metall.*, 9 (1961), 138.
- [88] D. Shechtman and L.A. Jacobson, *Metall. Trans. A*, 6 (1975), 1325.
- [89] G. Vanderschaeve and T. Sarrazin, *Phys. Status Solidi*, 43a (1977), 459.
- [90] M. Yamaguchi, Y. Umakoshi, and T. Yamane, *Phil. Mag.*, 55 (1987), 301.
- [91] A. Faress and G. Vanderschaeve, *Acta Metall.*, 35 (1987), 691.
- [92] G. Vanderschaeve and B. Escaig, *Phys. Status Solidi*, 20a (1973), 309.
- [93] J.W. Christian and D.E. Laughlin, *Acta Metall.*, 36 (1988), 1617.
- [94] M.H. Yoo, *J. Mater. Res.*, 4 (1989), 50.
- [95] P.C. Rowlands, E.O. Fearon and M. Bevis, *Trans. Metall. Soc. A.I.M.E.*, 242 (1968), 1559.
- [96] M. Bevis, P.C. Rowlands, and F. Acton, *Trans. Metall. Soc. A.I.M.E.*, 242 (1968), 1555.
- [97] M.H. Yoo and B.T. Loh, *Fundamental Aspects of Dislocation Theory*, ed. by J.A. Simmons, R. de Wit, and R. Bullough (US-NI Spec. Publ. 317, 1970), Vol. I, p479.

- [98] A.H. Cottrell and B.A. Bilby, *Phil. Mag.*, 42 (1951), 573.
- [99] N. Thompson and D.J. Millard, *Phil. Mag.*, 43 (1952), 422.
- [100] J.A. Venables, *Phil. Mag.*, 6 (1961), 379.
- [101] J.T. Fourie, F. Weinberg, and F.W.C. Boswell, *Acta Metall.*, 8 (1960), 851.
- [102] P.B. Price, *Proc. Roy. Soc. (a) (London)*, 260 (1961), 251.
- [103] E. Orowan, *Dislocation in Metals*, A.I.M.E., New York, 1954, p116.
- [104] R.L. Bell and R.W. Cahn, *Proc. Roy. Soc. (a) (London)*, 239 (1957), 494.
- [105] R. Bullough, *Proc. Roy. Soc. (a)*, 241 (1957), 568.
- [106] T.H. Blewitt, R.R. Coltman and J.K. redman, *J. Appl. Phys.*, 28 (1957), 651.
- [107] D.G. Westlake, *Deformation Twinning*, ed. by R.E. Reed-Hill, J.P. Hirth, and H.C. Rogers (Gordon and Breach Science Publishers, 1964), p29.
- [108] H.S. Rosenbaum, *ibid.*, p43.
- [109] R.E. Reed-Hill, *ibid.*, p295.
- [110] M.H. Yoo, *Metall. Trans. A*, 12A (1981), 409.
- [111] D.G. Westlake, *Acta Metall.*, 9 (1961), 327.
- [112] K. Yasutake, S. Shimizu, and H. Kawabe, *J. Appl. Phys.*, 61 (1987), 947.
- [113] J.K. Lee and M.H. Yoo, *Metall. Trans. A*, 21A (1990), 2521.
- [114] R.A. Lebensohn and C.N. Tome, *Phil. Mag. A*, 67 (1993), 187.
- [115] R.E. Cooper, *Acta Metall.*, 13 (1965), 46.
- [116] R.E. Cooper, *Acta Metall.*, 14 (1966), 78.
- [117] M.J. Marcinkowski and K.S. Sree Harsha, *Trans. Metall. Sco. AIME*, 242 (1968), 1405.
- [118] S. Takeuchi and A.S. Argon, *J. Mater. Sci.*, 11 (1976), 1542.

- [119] A.H. Clauer, B.A. Wilcox and J.P. Hirth, *Acta Metall.*, 18 (1970), 381.
- [120] D. McLean, *J. Inst. Metals*, 80 (1951-52), 507.
- [121] J.D. Parker and B. Wilshire, *Phil. Mag.*, 41A (1980), 665.
- [122] M. Henderson and K.F. Hale, *Proc. 3rd Int. Conf. on High Voltage Electron Microscopy*, eds by P.R. Swann, C.J. Humphreys and M.J. Goringe, Academic Press, New York, 1974, p206.
- [123] T.G. Langdon and R.B. Vastava, *Mechanical Testing for Deformation Model Development*, eds. by R.W. Rohde and J.C. Swearingen, ASTM, 1982, p435.
- [124] D. Hanson and M.A. Wheeler, *J. Inst. Metals*, 45 (1931-32), 229.
- [125] W.A. Wood and G.R. Wilms, *J. Inst. Metals*, 75 (1948-49), 693.
- [126] C.R. Barrett, J.L. Lytton and O.D. Sherby, *Trans. AIME*, 239 (1967), 170.
- [127] J.E. Bird, A.K. Makherjee, and J.F. Dorn, *Proc. Int. Conf. on Quantitative Relation Between Properties and Microstructure*, eds. by D.G. Brandon and A. Rosen, Israel University Press, Jerusalem, 1969, p225.
- [128] F.R.N. Nabarro, *Conference Proceedings on "Strength of Solids"*, The Physical Society, London, 1948, p78.
- [129] C. Herring, *J. Appl. Phys.*, 21 (1950), 437.
- [130] R.L. Coble, *J. Appl. Phys.*, 34 (1963), 1679.
- [131] J. Harper and J.E. Dorn, *Acta Metall.*, 5 (1957), 654.
- [132] O.D. Sherby and P.M. Burke, *Prog. Mater. Sci.*, 13 (1967), 325.
- [133] J. Weertman, *Trans. AIME*, 218 (1960), 207.
- [134] J. Weertman, *Acta Metall.*, 25 (1977), 1393.
- [135] D. McLean, *Rep. Prog. Phys.*, 29 (1966), 1.

- [136] R. Lagneborg, *Met. Sci. J.*, 3 (1969), 161.
- [137] N.F. Mott, *Proc. Conf. on Creep and Fracture of Metals at High Temperatures*, H.M.S.O., London, 1956, p21.
- [138] P.B. Hirsch and D. Warrington, *Phil. Mag.*, 6 (1961), 735.
- [139] C.R. Barrett and W.D. Nix, *Acta Metall.*, 13 (1965), 1247.
- [140] M. Yamaguchi and H. Inui, *Structural Intermetallics*, ed. by R. Daralia et al. (A Publication of TMS, Warrendale, PA, 1993), p127-142.
- [141] M. Yamaguchi, and Y. Umakoshi, *Prog. in Mater. Sci.*, 34 (1990), 1.
- [142] J.P. Hirth, and J. Lothe, *Theory of Dislocations*, Second Edition, John Wiley & Sons, Inc., 1982.
- [143] M.J. Darkburn, *The Science, Technology and Application of Titanium*, edited by R.T. Jaffee and N.E. Promisel (Pergamon Press, London, 1970), p633.
- [144] H.E. Deve, A.G. Evans, and D.S. Shih, *Acta Metall.*, 40 (1992), 1259.
- [145] T.E. Mitchell and J.P. Hirth, *Acta Metall.*, 39 (1991), 1711-1717.
- [146] R.E. Peierls, *Proc. Phys. Soc.*, 52 (1940), 23.
- [147] F.R.N. Nabarro, *Proc. Phys. Soc.*, 59 (1947), 256.
- [148] G. Fantozzi, C. Esnouf, W. Benoit, and I.G. Ritchie, *Prog. Mater. Sci.*, 27 (1982), 311.
- [149] R. Bullough and V.K. Tewary, *Dislocations in Solids*, ed. by F.R.N. Nabarro (North-Holland Publishing Company, 1979), Vol. 2, p1.
- [150] I.L.F. Ray and D.J.H. Cockayne, *Proc. Roy. Soc. London A*, 325 (1971), 543.
- [151] C. Weigel, H. Alexander, and J.W. Corbett, *Phys. Status Solidi. B*, 71 (1975), 701.

- [152] C.L. Fu and M.H. Yoo, *Phil. Mag. Letter*, 62 (1990), 159-165.
- [153] C.L. Fu and M.H. Yoo, *Phil. Mag. Letter*, 58 (1988), 199.
- [154] M.H. Yoo, C.L. Fu, and J.K. Lee, *Twinning in Advanced Materials*, ed. by M.H. Yoo, M. Wuttig (TMS Publication, 1994), in press.
- [155] T. Fujiwara, A. Nakamura, M. Hosomi, S.R. Nishitani, Y. Shirai, and M. Yamaguchi, *Phil. Mag. A*, 61 (1990), 591.
- [156] S.C. Cheng, J. Wolfenstine, and O.D. Sherby, *Met. Trans.*, 23A (1992), 1509.
- [157] H. Oikawa, in the *Proc. of High Temperature Aluminides & Intermetallics*, ed. S.H. Whang, C.T. Liu, D.P. Pope and J.O. Stiegler, TMS, 1990, p353.
- [158] M. Yamaguchi, *Metals and Technology*, 60 (1990), 34.
- [159] Y. Yamabe, K. Sugawara and M. Kikuchi, *Proceedings - 1990 Tokyo Meeting*, Japan Inst. of Metals, Sendai, the Japan Inst. of Metals, 1988, p409.
- [160] V.Yu. Gertsman, et al, *Scripta Metall.* 24 (1990), 1027.
- [161] W.A. Kaysser, in the *Proc. of Second International Conference on Hot Isostatic Pressing: Theory and Applications* (Gaithersburg, MD, USA, June 7-9, 1989), p1.
- [162] K. Matsuki et al., *Z. Metallkde*, 79 (1988), 231.

MICHIGAN STATE UNIV. LIBRARIES



31293010517831